Transport and Anisotropy inside Ionic Polymer Membranes

Jianbo Hou

Dissertation submitted to the faculty of the Virginia Polytechnic Institute and State University in partial fulfillment of the requirements for the degree of

Doctor of Philosophy
In
Chemistry

Louis A. Madsen
Herve Marand
Harry C. Dorn
Edward Valeev

(October 2nd, 2012)
Blacksburg, VA

Keywords: ionomer
transport
pulsed-field-gradient NMR
structural characteristic
molecular interactions

Transport and Anisotropy inside Ionic Polymer Membranes

Jianbo Hou

ABSTRACT

Water and ion transport critically determine the performance of many functional materials and devices, from fuel cells to lithium ion batteries to soft mechanical actuators. This dissertation aims to address some fundamental issues regarding transport and anisotropy, structural heterogeneity and molecular interactions inside ionic polymers.

I first discuss a main deficiency of a standard protocol for calibrating high pulsed-field-gradient NMR. I show that high gradient calibration using low γ nuclei is not amenable to measurements on slow diffusing high γ nuclei. Then I employ NMR diffusometry to investigate transport and anisotropy for a series of ionic polymers, from poly(arylene ether sulfone) hydrophilic-hydrophobic multi-block copolymers to polymer blends to perfluorosulfonate random copolymers.

For the multi-block copolymers, NMR diffusion measurements yield diffusion anisotropy as a function of water uptake and block lengths. ^{2}H NMR spectroscopy on absorbed D_2O probes membrane alignment modes. These measurements also provide insights into average defect distributions.

For the blend membranes, we examine the impact of compatibilizer on their transport properties. An increase in compatibilizer significantly improves the membrane phase homogeneity confirmed by SEM and transport studies. Theories of diffusion in porous media yield changes in domain size and tortuosity that correspond to drastic changes in local restrictions to water diffusion among different blend membranes. NMR

relaxometry studies yield multi-component T_1 values, which further probe structural heterogeneities on smaller scales than diffusion experiments.

For the random copolymer, the exploration of ion transport reveals inter-ionic associations of ionic liquids (ILs) modulated by hydration level and ionic medium. When ILs diffuse inside ionic polymers, isolated anions diffuse faster ($\geq$ 4X) than cations at high hydration whereas ion associations result in substantially faster cation diffusion ($\leq$ 3X) at low hydration inside membranes, revealing prevalent anionic aggregates.

Finally, I present the strategy and analytical protocol for studying ionomer membranes using ILs. The normal cation diffusion contrasts to the anomalous anion diffusion caused by local confinement structures inside the membranes, which vary drastically with temperature and hydration level. These structures correspond to a density variation of SO_3^- groups, which define a distribution of local electrical potentials that fluctuate with temperature and nature of ionic media.

Acknowledgement

There are many people I would like to thank for their help and concerns over the span of my graduate study. First, I am greatly indebted to my advisor Professor Louis Madsen for all his guidance, patience, support, encouragement and precious time during the past 4 years. His constant enthusiasm for science and personal charisma have always motivated my research toward a new level. This dissertation would not be possible without his guidance and contribution.

I would also like to show my sincere appreciation to my committee members: Professor Harry Dorn, Edward Valeev, Herve Marand and Tim Long for their valuable comments on my research and precious time spent reading this dissertation.

I want to make a special acknowledgement to Dr. Jing Li, who guided me into the practical world of NMR and from whom I have greatly benefited in terms of research strategy and thinking pattern. I would not have made any progress without his early instructions and help.

In addition, I am grateful to all my Madsen group colleagues, Dr. Mark Lingwood, Kyle Wilmsmeyer, Zhiyang Zhang, Kacey McCreary, James Wahmhoff, Bryce Kidds, Cocoa Wang and Ying Wang for being supportive and creating a lovely and comfortable atmosphere in the lab.

I would like to thank our collaborators Dr. Harry Lee, Dr. Changhyun Lee and Prof. McGrath for providing polymer membrane samples, Dr. David Mountz and Dr.Marisa Hull at Arkema for providing and discussing proton conductivity and microscopy results, Dong Wang and Prof. Heflin at Virginia Tech for the actuator test, Yang Liu and Prof. Qiming Zhang at PennState University for providing ionic liquid samples and useful discussion.

My acknowledgement further extends to my friends Tian Gao, Zhe Liu, Zhen Liu, Renlong Gao and Tianyu Wu for their company and support.

Finally, I would like to show my deep appreciation to my parents for their love, support and encouragement over the years. I would not be able to set up my belief and life goal without their dedications to my education.

Table of Contents

List of Figures

List of Tables

Chapter 1

Transport Concepts in Advanced Functional Materials

1.1 Motivation, Strategy and Research Goal

Ionic polymers (ionomers) represent promising candidates for a series of functional materials and devices, from fuel cells to water reverse osmosis membranes to artificial muscle actuators.[1-3] Many of these useful ionomer membranes consist of hydrophilic and hydrophobic moieties that nanophase separate to form interconnected hydrophilic channels that allow water transport and ion conduction.[4-6] Structural motifs such as orientation, size and connectivity of ionic domains and channels within the polymer network will strongly impact water and ion transport.[7-10] Understanding the role of these key factors in the transport process will give insightful guidance on and direct targeted design of new materials.

Nuclear magnetic resonance (NMR) spectroscopy has become an indispensible tool for studying structures and molecular dynamics. Our group has deeply investigated water and ion transport as well as structural characteristics inside ionomers by combining NMR diffusometry and advanced NMR spectroscopy.[11-16] In general, our strategy relies on probing multi-scale (~100 nm – 10 μm) structural features (domain sizes, confinement, defects, tortuosity) in soft materials by tracking the position and reorientation of diffusing species, such as H_2O and ions.[11,12,17] Pulsed-field-gradient (PFG) NMR allows measuring molecular diffusion coefficient in a wide range (10^{-14}-10^{-9} m^2/s), therefore reflecting structural features on multiple length scales. Diffusion and anisotropy measurements yield quantitative information regarding structural and dynamic anisotropy inside ionomers. ^2H NMR spectroscopy further provides

useful information on the orientational ordering inherited by the probe molecules (D_2O, CD_3OD) through quadrupolar splitting. The combination of these measurements allow quantitative assessment of average alignment and alignment mode of hydrophilic channels inside the polymer. In addition, sample modulations, such as hydration level, molecular weight variation and mechanical deformation strongly impact these structural characteristics.[13,15,18-21] Through systematic NMR studies on different samples, as well as combining NMR with other techniques like X-ray scattering and TEM,[20,22,23] we aim to bridge the gap between microscopic and macroscopic worlds to obtain a better understanding of these complex materials.

The rest of this dissertation is organized as follows: Chapter 1 quickly reviews the objects of our research focus: polymer electrolyte membrane fuel cells (PEMFCs) and soft mechanical actuators. We briefly discuss some factors influencing device operation, with particular emphasis on the critical roles of water and ion transport. Following this perspective, chapter 2 discusses the fundamental significance of transport phenomena and specifically focuses on the molecular diffusion process, followed by describing its physical meaning and mathematical origin. We then introduce relevant theoretical and experimental aspects of NMR spectroscopy and diffusometry for anisotropy, diffusion and structural studies in later chapters. In chapter 3, we report a new discovery that discloses a main deficiency of the standard protocol for high gradient calibration using low gyromagnetic ratio nuclei. Detailed discussion on the role of relevant parameters leads to a more robust protocol for high gradient calibration, which can effectively avoid data misinterpretation. These results thus provide meaningful guidance toward investigating slow diffusion process in complex materials. In chapter 4 and 5, we analyze diffusion and anisotropy results in a series of poly(arylene ether sulfone) block copolymers and polyelectrolyte/PVDF blends. Further correlation with microscopy measurements (TEM, SEM) reveals useful structural

information, such as local defects, domain sizes and orientations. These new "insights" bring forward another useful strategy to characterize ionomers. In chapter 6 and 7, we deeply explore ion transport and intermolecular interactions of ionic liquids (ILs) inside ionomers. Our ion diffusion studies clearly elucidate ion associations inside ionomers that correlate with the macroscopic actuation test. Moreover, we utilize the idea of "double probes" to study the perfluorosulfonate ionomers by measuring the slow cation and anion diffusion of ILs inside these dry membranes. This study leads a revisit to the "ionic nature" of these polymers and strongly emphasizes the significance of local dynamics for ion transport. These discoveries provide new insightful guidance toward materials design and innovation. Finally, chapter 8 gives a summary and comments on future work.

1.2 Proton Exchange Membrane Fuel Cell (PEMFC)

1.2.1 Principle and Configuration of PEMFC

The past few decades have witnessed a rapid growth in development of renewable energy materials for global sustainability.[24-27] Polymer electrolyte membrane fuel cells (PEMFCs) have become a research focus due to their high efficiency in generating electricity via oxidizing renewable resources into environmentally benign products, thereby holding promise to meet the ever increasing global demand for fossil fuels (coal, petroleum, natural gas) and clean energy. High performance fuel cells may serve as power sources to automobiles and portable electronics, such as laptops and cameras.[28,29] Depending on the type of electrolyte used, fuel cells are also classified into other categories, such as alkaline fuel cells (AFC), direct methanol fuel cells (DMFC), phosphoric acid fuel cells (PAFC), molten carbonated fuel cells (MCFC) and solid oxide fuel cells (SOFC).[29]

Unlike batteries which store electrical energy only internally in chemical substances, fuel cells can utilize a constant supply of fuels (usually hydrogen and oxygen) to maintain the subsequent electrochemical reactions:

$$\text{Anode:} \quad 2H_2 \rightarrow 4H^+ \rightarrow 4e^-$$

$$\text{Cathode:} \quad O_2 + 4H^+ + 4e^- \rightarrow 2H_2O$$

$$\text{Overall:} \quad 2H_2 + O_2 \rightarrow 2\,H_2O$$

For illustration, figure 1.1 schematically shows the configuration of a PEMFC where the membrane electrolyte assembly (MEA) is sandwiched between two electrodes. The chemical reactions result in a concentration gradient that drives proton transport across the electrolyte, which is usually made of an ion conducting polymer. Meanwhile, electrons generated at the anode migrate fast along the external circuit to the cathode and produce electrical power.

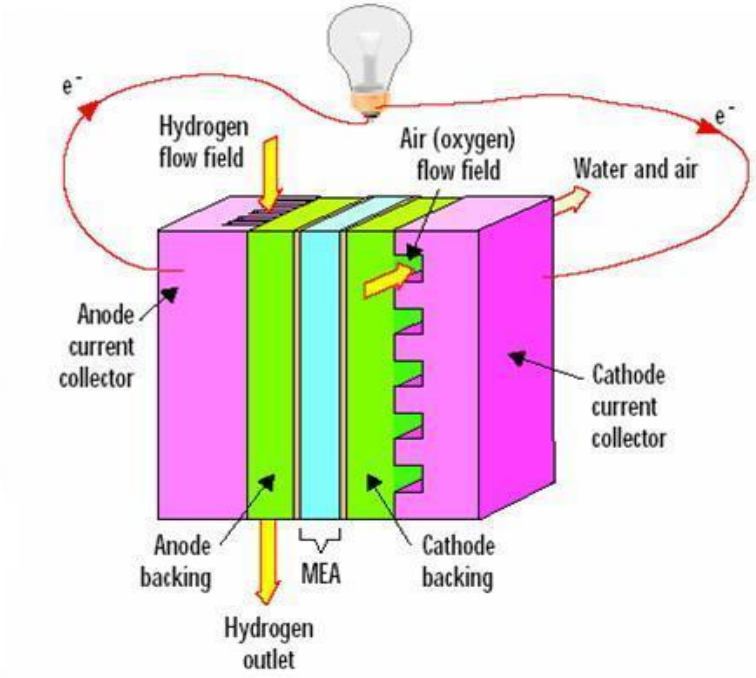

Figure 1.1. Configuration of a proton exchange membrane fuel cell

Flow of H_2 and O_2 gas respectively into the anode (left) and cathode (right) provides constant fuel and oxidant supplies. Electric current forms by electrons moving in the outer circuit. Meanwhile, protons migrate across the membrane electrolyte assembly (MEA), which is sandwiched between the two electrodes.

Early investigations of PEMFCs progressed slowly due to the lack of robust and efficient electrolyte materials.[29] The advent of ionomers greatly facilitates the research progress for fuel cell applications. Developed and commercialized by Dupont, Nafion® is a perfluorosulfonate ionomer (PFSI) that stands out as the bench mark material for fuel cell membranes. This material chemically assembles hydrophobic and hydrophilic moieties that phase separate on the ~ 1 nm scale. The hydrophilic phase forms interconnected channels that are distributed in the hydrophobic matrix to allow water transport and ion conduction but with an acceptable mechanical, thermal and chemical performance.[6] Many critical issues remain to be addressed with regard to fuel cell applications, including mechanical durability, chemical and thermal stability, proton conduction, electrolyte morphology, etc.. Herein, we mainly focus on water and ion transport inside ionomers to understand the impact of structural specificity and molecular interactions on the transport property of these polymeric materials.

1.2.2 Water Transport and Management

Water content inside ionomer membranes plays a significant role during fuel cell operation. High water content is usually desirable since both water transport and proton conduction increase monotonically with the hydration level prior to saturation.[18] Fast water transport effectively suppresses local drying across the electrolyte membrane, thereby maintaining a high efficiency of the whole device. On the other hand, water accumulated at the cathode should be removed upon its generation to minimize backward diffusion and avoid cathode flooding.[30] It is also necessary to

tightly control the hydration effect to evaluate and compare transport properties among different fuel cell membranes. Most fuel cell studies use relative humidity as the measured "control" parameter when determining fuel cell performance and membrane properties.[30-32] While this is a convenient control parameter, the water content is the key variable for determining morphological structure and transport inside the membrane. Thus, we choose to control water uptake as an independent variable rather than relative humidity. In general, water uptake is defined as the grams of water per gram of polymer dry weight,[33] known as wt%, or the number of water molecules per (sulfonic, carboxylic) acid group of the polymer, known as λ. For Nafion® with an equivalent weight of EW (grams of polymer per mole of sulfonate groups), wt% relates to λ by the following equation:

$$\text{wt\%} = \frac{M_{H_2O}}{EW} \times \lambda \qquad (1.2.1)$$

It is reported that water uptake from the liquid phase depends on the pretreatment of the polymer membrane[18,33] and the polymer's water uptake at equilibrium when exposed to the vapor phase is not the same as immersed in the liquid phase. Such a paradox (Schroeder's paradox) is partially due to the difference between interfacial interactions of polymer with the vapor phase and polymer with the liquid phase. In our study, we immerse polymer membranes in liquid phase to saturation and then controllably dry the sample in the open air to vary water content. We seal the membrane sample at room temperature in a homebuilt poly(tetrafluoroethylene) cell as shown in figure 1.2 for equilibration prior to any NMR measurement. The sample cell has a relatively low dead volume (< 20% vol.), which allows fast equilibration. All water transport studies are performed at 25 ^{o}C and water uptake is then determined via gravimetric measurements of the dry and hydrated membranes.

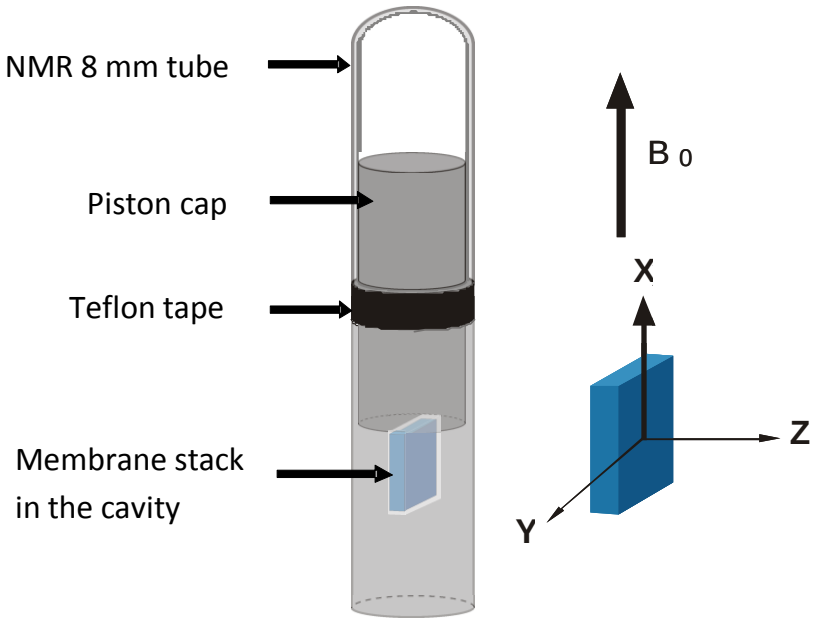

Figure 1.2. Sealed Teflon cell configuration

Membrane pieces are stacked in the same orientation to snugly fit the rectangular shaped cavity in the cell. A piston cap is used to seal the cell in which membranes are equilibrated. An NMR tube is connected to the piston cap for ease of handling and the sample cavity is centered in the NMR coil.

1.2.3 Proton Conduction

Proton conductivity is a key parameter in the evaluation of fuel cell membranes. Nafion is one of the benchmark materials with a typical conductivity value around 0.1 S/cm under high hydration levels ($\lambda > 10$), which is roughly one order of magnitude lower than the value in sulfuric acid (20wt%).[34] The proton conductivity also strongly depends on water uptake and decreases significantly at low hydration levels ($\lambda < 3$).[33] Grotthuss' hopping mechanism[35] and Kreuer's vehicle mechanism[36] are widely used to explain the proton conduction process at different hydration levels. These processes are illustrated in figure 1.3. At high hydration levels,

the hopping mechanism indicates that protons can hop in the network formed by adequate amount of water molecules, which leads to enhanced proton conductivity. In the absence of enough water molecules to form a continuous network, protons travel with the water molecules, resulting in drastically reduced proton conductivity limited by water diffusion.

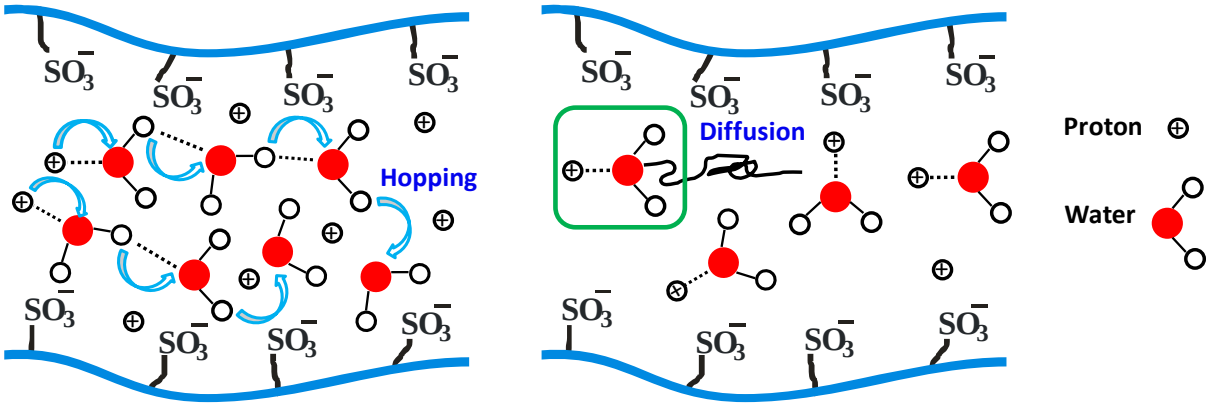

Figure 1.3. Proton transport: (a) hopping and (b) vehicular mechanism

In case (a), fast protons transport occurs via hopping through the hydrogen bonding network formed by adequate amount of water molecules. In case (b), due to the lack of water molecules to form a hydrogen bonding network, proton transport is associated with water diffusion. The proton migration causes a local charge density variation but maintain the charge neutrality macroscopically.

When comparing polymer membranes, other factors such as morphology, domain orientations and chemical compositions also dramatically impact the measured proton conductivity,[7,30,37] which may vary by orders of magnitude. Thus, improving the proton conduction inside ionomer membranes is viable through targeted synthesis and optimized post-processing protocols. Detailed understanding of how relevant parameters modulate the proton conduction will further inform the development of durable and high performance fuel cells.

1.2.4 Morphological Features of Ionomers

Ionomer membranes have complex morphologies that closely relate to the performance of fuel cells.[6,28,36] The morphological features of Nafion have been explored and discussed extensively in the literature.[5,9,38,39] Despite great efforts contributed to unraveling the structure of Nafion, its morphology still remains in debate.[5] Previous studies largely focused on using neutron and X-ray scattering techniques (SANS, SAXS, WAXS) to extract morphological information.[4,39,40] Early X-ray scattering studies provide solid evidence for the presence of ionic aggregation and crystal domain structures inside Nafion, which consistently agree with later investigations.[6] Gierke and coworkers[4] therefore proposed a model of ionic clusters to account for the morphology of hydrated Nafion (figure 1.4), in which ionic clusters (SO_3^-) are described as inverted micellar structures that form interconnected hydrophilic channels to facilitate water transport and ion conduction.

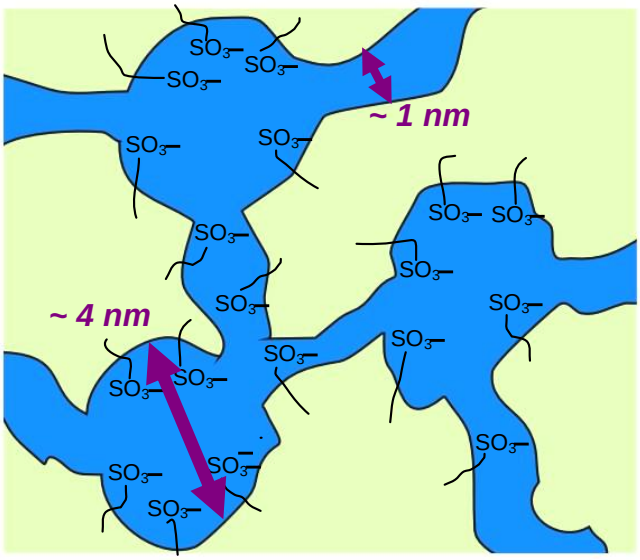

Figure 1.4. Cluster-network morphological model for hydrated Nafion[4]

Sulfonate groups aggregate into ionic clusters that from interconnected hydrophilic channels (blue part) in the presence of water. The yellow background represents the semicrystalline fluorocarbon matrix that provides mechanical and chemical stability.

Other morphological interpretations of Nafion also exist. For example, Roche and coworkers[41,42] used SAXS and small angle neutron scattering (SANS) to study the morphology of Nafion (equivalent weight = 1200) and found three contrast regions in the accessible measurement range, one of which is attributed to the crystalline phase. They concluded that either a non-random distribution of side chains exists in some portion of the material or that side groups are included in the crystalline structure. Morphological characteristics of ionic domains including a channel network,[38,43] layered structure[39,44,45] and fibril bundles[9,40] have also been suggested to exist. In a recent study, Schmidt-Rohr and coworkers proposed a parallel cylindrical nanochannel model for Nafion based on their simulation results.[5] This "new" model highlights the presence of cylindrical water nanochannels, which are randomly packed in the polymer matrix.

In recent years, significant efforts have been devoted to exploring the morphology of the ionomer using other microscopy and spectroscopy techniques. Xue and coworkers reported the existence of a three phase morphology in solution cast Nafion 117 using TEM,[46] where spherical clusters were observed to range from 25 to 50 Å in diameter. Recent NMR diffusion studies[8] suggest the presence of submicron domain structures reflected by restricted water diffusion at low temperatures. Our group has expanded on the hydrophilic channel alignment modes[5,47] for different ionomer membranes using ^{2}H NMR spectroscopy.[48] Figure 1.5 represents different channel alignment modes for Nafion, where A and B depict the biaxial ellipsoidal and cylindrical alignment modes respectively, C represents a collection of channel bundles that are uniaxially

aligned. These channel alignment modes well correlate with the transport anisotropy revealed by NMR diffusion measurements.

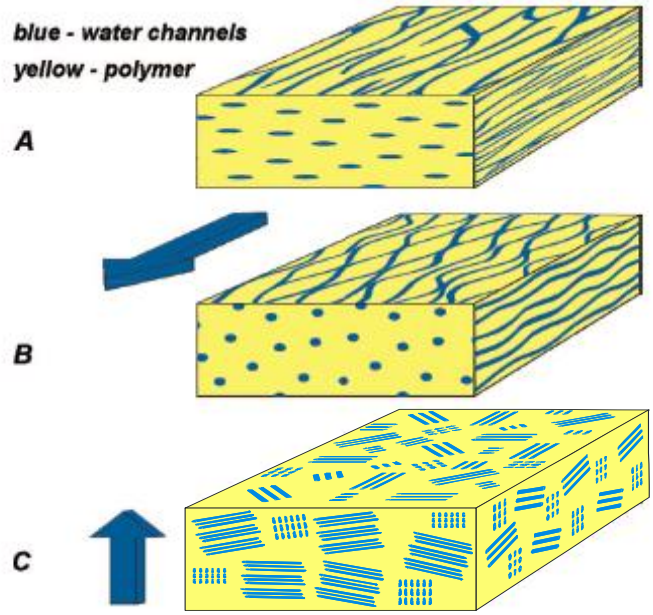

Figure 1.5. Hydrophilic channel alignment modes for Nafion[15,48]

A. Biaxial alignment in Nafion 112 formed by ellipsoidal channels; B. Biaxial alignment in Nafion 112 formed by cylindrical channels with directional anisotropy; C. Bundles of uniaxially aligned channels in Nafion 212.

We have further investigated the impact of mechanical stretching on channel dimension, domain orientation, and defect structures in ionomers. We measure water transport and anisotropy in a series of drawn Nafion 117 membranes, defining the draw ratios as L = final length (l) / initial length (l_0).[10] We notice conservation of the diffusion tensor trace (independent of water uptake) and linear coupling between order parameter (by ^{2}H splitting) and diffusion anisotropy. This evidence strongly demonstrates that these domains of channels behave like liquid crystals[49-52] simply reorienting along the uniaxial stretching direction without perturbing

their dimensions and the nature of defect structures (character, density). Based on the absolute value of the order parameter derived from the small angle X-ray scattering data, the linear coupling between order parameter and diffusion anisotropy results in a molecular aspect ratio of 1.8, which agrees well with that of the diffusing water molecules.[53]

1.3 Soft Mechanical Actuator

1.3.1 Ionic Electroactive Polymers (*i*-EAPs)

Soft mechanical actuators are energy conversion devices that can mimic the behavior of biological tissues and are often termed artificial muscles. These devices hold promising applications in the field of biomimetic and soft tissue engineering.[54] In particular, an emerging class of electroactive polymers (EAPs) has attracted great attention as they exhibit large mechanical deformation in response to electric field stimulus, thus finding wide applications in sensor and actuator fabrication.[2,55,56] Unlike piezoelectric materials such as poly (vinylidene fluoride) (PVDF), these polymers can generate large strain under relatively low voltages (1- 5V). For example, figure 1.6 shows the bending behavior of an EAP actuator in the presence of an electric field. The actuation process involves a series of steps, including the electrostatic interactions between ionic species and the external electric field, as well as ion transport and accumulation at the electrode interface, which enable electromechanical coupling.[2] Depending on the actuation mechanism, EAPs are generally divided into two categories: electronic EAPs and ionic EAPs, the latter of which can be further classified into ionic polymer metal composites (IPMC), ionic polymer gels (IPG), carbon nanotubes (CNT), conductive polymers (CP) and electrorheological fluids (ERF).[57]

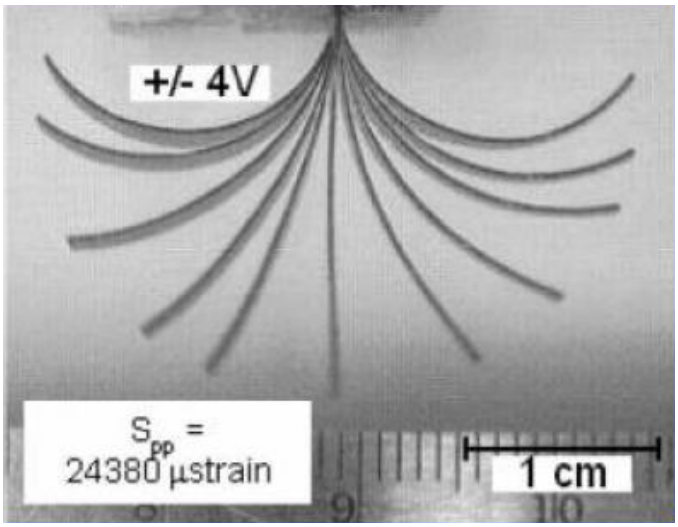

Figure 1.6. Electric-field-induced mechanical deformation of an actuator

This *i*-EAP actuator exhibits oscillating bending motions in response to an alternating electric field.[58] Copyright 2006 Elsevier.

In particular, actuator devices fabricated using ionomers are also termed ionic polymer transducers (IPTs).[2] A proposed mechanism regarding the mechanical actuation of IPTs originates from the local strain induced by ion accumulation at the electrode-electrolyte interfaces.[2,59] For illustration, figure 1.7 graphically explains the bending mechanism of an ionic polymer actuator by asymmetric swelling of the two electrodes.

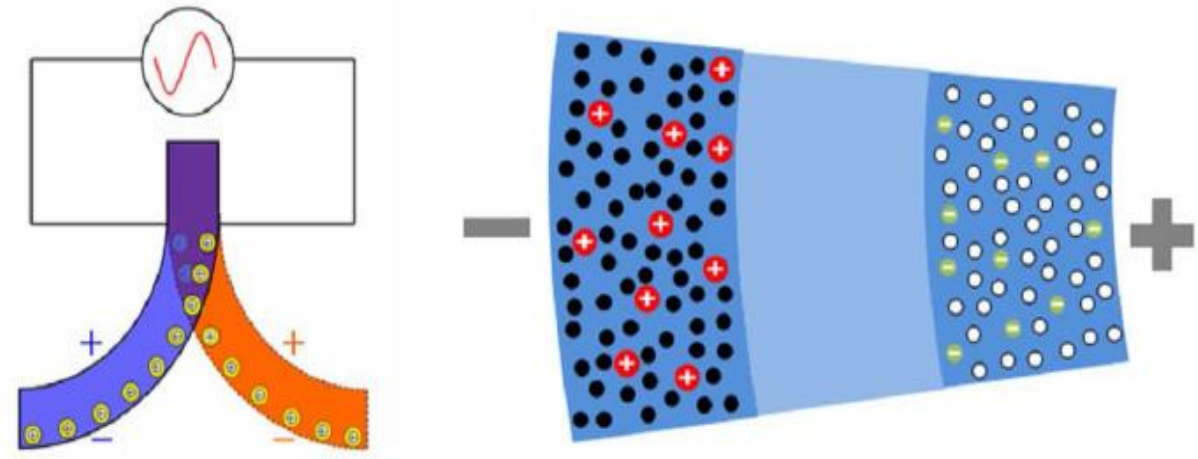

Figure 1.7. Bending mechanism of the ionic polymer actuator

An applied electric field induces cation and anion migration, which swells the cathode and anode. The cation/anion size difference (or difference in local molecular interactions) result in asymmetric electrode swelling and bending actuation.[60] Copyright Yang Liu 2012

Typically, these ionomer-based actuator devices are composed of three main components: a piece of ionomer membrane, metal electrodes and mobile ionic species that respond to an electric field. As mentioned in section 1.2, the perfluorosulfonate ionomer Nafion remains the benchmark material for designing and developing these functional devices. The polymer membrane plays a critical role in the process of mechanical actuation by offering a mechanically robust medium for ion transport. For the conducting electrodes, one usually desires a high surface area to enhance the whole device's capacitance. Using the layer-by-layer method[61] or by loading conducting nanoparticles[62] onto the interfaces between the electrolyte and electrodes represents a viable protocol to achieve high capacitance. Meanwhile, ion migration in the presence of an electric field is crucial to allow electromechanical coupling for subsequent mechanical actuation. Many relevant factors strongly impact ion migration, including the nature of the ions (electron density, size, shape anisotropy, specific molecular interactions), ion concentrations and the local dielectric medium. *i*-EAPs should therefore optimally combine different components to achieve high actuation performance.

1.3.2 Ion Dense Electrolytes: Ionic Liquids

The electrolyte has a significant contribution to the performance of mechanical actuators. Ideal liquid electrolytes should yield fast ion conduction with high carrier density and avoid leakage at the same time. Room temperature ionic liquids (RTILs) are molten salts that consist of

mobile cations and anions. Their bulky ion sizes and lack of structural symmetry reduce their molecular packing efficiency,[63] thus enabling their fluidity at relatively low temperatures (<100 ^{o}C). Figure 1.8 shows representative chemical structures of some ionic liquids used in this dissertation. The intricate inter-ionic interactions within ILs could be tailored by properly choosing the type of cation and anion. Due to their unique properties, ILs find useful applications in catalysis, batteries and polymer-based actuators.[64,65]

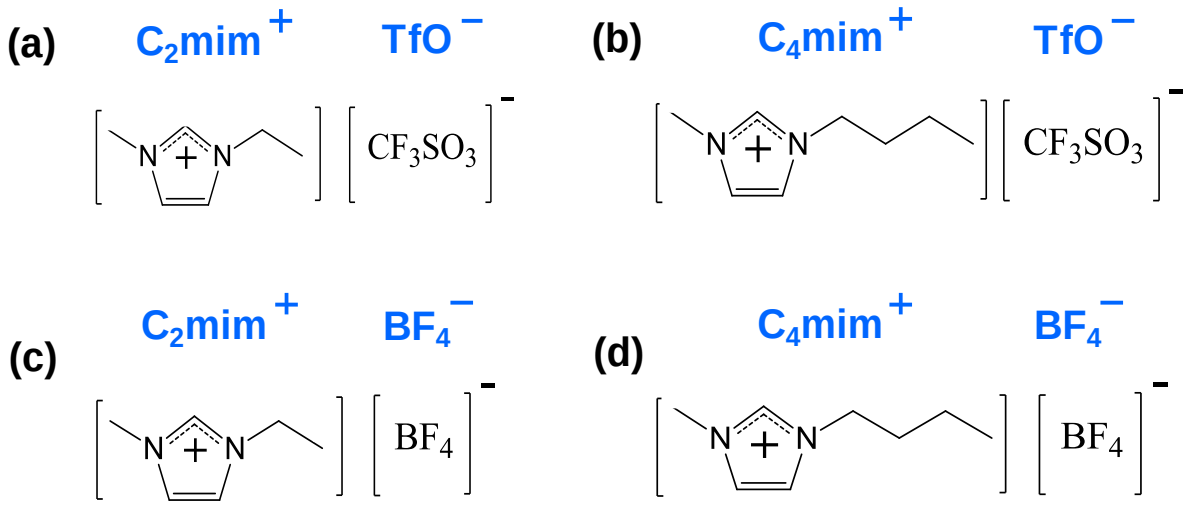

Figure 1.8. Chemical structures of some imidazolium based ILs

(a) 1-ethyl-3-methyl-imidazolium trifluoromethanesulfonate; (b) 1-butyl-3-methyl-imidazolium trifluoromethanesulfonate; (c) 1-ethyl-3-methyl-imidazolium tetrafluoroborate; (d) 1-butyl-3-methyl-imidazolium tetrafluoroborate.

Traditional *i*-EAPs[56] generate actuation by utilizing water or organic solvents to solvate the counterions associated with the polymer backbone to facilitate ion conduction. Here, the ionomer serves as the electrolyte itself. However, these actuators mainly suffer from the drawback of long time stability due to solvent evaporation.[56] The relatively narrow

electrochemical window of water (1.23 V) also limits the bending amplitude of these actuators, by limiting the maximum applied voltage. In comparison, ILs offer tremendous advantages over traditional solvents for actuators because of their non volatility. Impregnating ILs into the polymer membrane endows the system with largely improved performance due to their fairly wide electrochemical window (~ 4-6 V) and good ionic conductivity (~ 1-10 mS/cm). IL based actuators could operate stably without performance degradation after millions of cycles.[66]

1.3.3 Ion Transport and Associations inside *i*-EAPs

Ion transport inside ionomers governs the ion accumulation rate at the interfaces between the electrolyte and electrodes, which determines the response time and deformation amplitude of mechanical actuators. As mentioned earlier, traditional *i*-EAPs using solvent such as water or methanol are termed single-ion conductors since only counterions complementing the polymer-fixed ions are available for ion conduction. In this particular case, ionomers act both as the electrolyte and ionic media for ion transport. Low viscosity, good ion solvation and ion delocalization represent the crucial criteria to obtain fast ion conduction, thereby achieving high actuation performance. However, the volatile nature of these solvents suggests that the system can only operate efficiently at relatively high humidity or immersed in a corresponding liquid phase. In an open air condition, the performance of a water-based ionic polymer actuator degrades drastically only after 10^3 cycles due to water evaporation.[56]

In contrast, incorporating ILs into polymer membranes effectively eliminates solvent evaporation and improves ion conduction. However, this method introduces a new problem since both mobile cations and anions contribute to the ion conduction and the system evolves into a multiple-ion conductor (single ion, triple ion). Depending on the nature of the IL, inter-ionic interactions between cations and anions may drive the formation of more complicated ion

clusters, thus increasing the system complexity. If cations and anions completely dissociate, they will likely conduct equally in opposite directions. Consequently, ion-accumulation-induced local strain on the two electrodes will likely balance each other, leading to a drastically degraded actuation performance.

On the other hand, if cations and anions are strongly coupled to form symmetric pairs, then both ion conductivity and actuation performance will drop off significantly. To improve the actuation performance, asymmetric ion packing is highly preferable, which depends on factors, such as molecular charge distribution (charge density), molecular geometry, electronegtivity (basicity) and temperatures (dielectric constant) etc.. The trade off between fast ion conduction and associations requires further considerations in the design of actuators. Detailed understanding of how both ion associations and transport impact the actuation process will provide pivotal insight toward developing advanced mechanical actuators with better performance.

References

[1] H.S. Lee, A. Roy, O. Lane, S. Dunn, J.E. McGrath, Hydrophilic-hydrophobic multiblock copolymers based on poly(arylene ether sulfone) via low-temperature coupling reactions for proton exchange membrane fuel cells, Polymer, 49 (2008) 715-723.
[2] A.J. Duncan, D.J. Leo, T.E. Long, Beyond Nafion: Charged macromolecules tailored for performance as ionic polymer transducers, Macromolecules, 41 (2008) 7765-7775.
[3] R.J. Petersen, Composite reverse-osmosis and nanofiltration membranes, J. Membr. Sci., 83 (1993) 81-150.
[4] T.D. Gierke, G.E. Munn, F.C. Wilson, The morphology in Nafion perfluorinated membrane products, as determined by wide-angle and small-angle X-ray studies, J. Polym. Sci., Part B: Polym. Phys., 19 (1981) 1687-1704.
[5] K. Schmidt-Rohr, Q. Chen, Parallel cylindrical water nanochannels in Nafion fuel-cell membranes, Nature Mater., 7 (2008) 75-83.
[6] K.A. Mauritz, R.B. Moore, State of understanding of Nafion, Chem. Rev., 104 (2004) 4535-4585.
[7] M.J. Park, N.P. Balsara, Anisotropic proton conduction in aligned block copolymer electrolyte membranes at equilibrium with humid air, Macromolecules, 43 (2010) 292-298.

[8] T. Ohkubo, K. Kidena, A. Ohira, Determination of a micron-scale restricted structure in a perfluorinated membrane from time-dependent self-diffusion measurements, Macromolecules, 41 (2008) 8688-8693.
[9] L. Rubatat, A.L. Rollet, G. Gebel, O. Diat, Evidence of elongated polymeric aggregates in Nafion, Macromolecules, 35 (2002) 4050-4055.
[10] J. Li, J.K. Park, R.B. Moore, L.A. Madsen, Linear coupling of alignment with transport in a polymer electrolyte membrane, Nature Mater., 10 (2011) 507-511.
[11] B. Deloche, E.T. Samulski, Nematic order in strained elastomers via ^{2}H NMR, Bull. Am. Phys. Soc., 26 (1981) 327-328.
[12] E.O. Stejskal, J.E. Tanner, Spin diffusion measurements: spin echoes in the presence of a time-dependent field gradient, J.Chem. Phys., 42 (1965) 288-292.
[13] J.B. Hou, J. Li, L.A. Madsen, Anisotropy and transport in poly(arylene ether sulfone) hydrophilic-hydrophobic block copolymers, Macromolecules, 43 (2010) 347-353.
[14] J. Li, K.G. Wilmsmeyer, L.A. Madsen, Anisotropic diffusion and morphology in perfluorosulfonate ionomers investigated by NMR, Macromolecules, 42 (2009) 255-262.
[15] M. Rankothge, Haryadi, G. Moran, J. Hook, L. Vangorkom, Orientation effects in the deuterium NMR-spectroscopy of perfluorinated ionomer membranes, Solid State Ionics, 67 (1994) 241-248.
[16] W.S. Price, Pulsed-field gradient nuclear magnetic resonance as a tool for studying translational diffusion .1. Basic theory, Concepts Magn. Reson., 9 (1997) 299-336.
[17] T.A. Zawodzinski, T.E. Springer, J. Davey, R. Jestel, C. Lopez, J. Valerio, S. Gottesfeld, A comparative-study of water-uptake by and transport through ionomeric fuel-cell membranes, J. Electrochem. Soc., 140 (1993) 1981-1985.
[18] M. Lee, J.K. Park, H.S. Lee, O. Lane, R.B. Moore, J.E. McGrath, D.G. Baird, Effects of block length and solution-casting conditions on the final morphology and properties of disulfonated poly(arylene ether sulfone) multiblock copolymer films for proton exchange membranes, Polymer, 50 (2009) 6129-6138.
[19] J. Lin, P.H. Wu, R. Wycisk, P.N. Pintauro, Z.Q. Shi, Properties of water in prestretched recast Nafion, Macromolecules, 41 (2008) 4284-4289.
[20] P.C. van der Heijden, L. Rubatat, O. Diat, Orientation of drawn Nafion at molecular and mesoscopic scales, Macromolecules, 37 (2004) 5327-5336.
[21] K.M. Cable, K.A. Maurtiz, R.B. Moore, Anisotropic ionic-conductivity in uniaxially oriented perfluorosulfonate ionomers, Chem. Mater., 7 (1995) 1601-1603.
[22] A.Z. Weber, J. Newman, Transport in polymer-electrolyte membranes - II. mathematical model, J. Electrochem. Soc., 151 (2004) A311-A325.
[23] H.X. Zhou, L.Q. Yang, A.C. Stuart, S.C. Price, S.B. Liu, W. You, Development of fluorinated benzothiadiazole as a structural unit for a polymer solar cell of 7% efficiency, Angew. Chem. Int. Ed., 50 (2011) 2995-2998.
[24] S.H. Bergens, C.B. Gorman, G.T.R. Palmore, G.M. Whitesides, A redox fuel-cell That operates with methane as fuel at 120-degrees-C, Science, 265 (1994) 1418-1420.
[25] U. Bach, D. Lupo, P. Comte, J.E. Moser, F. Weissortel, J. Salbeck, H. Spreitzer, M. Gratzel, Solid-state dye-sensitized mesoporous TiO_2 solar cells with high photon-to-electron conversion efficiencies, Nature, 395 (1998) 583-585.
[26] J.H. Pang, H.B. Zhang, X.F. Li, Z.H. Jiang, Novel wholly aromatic sulfonated poly(arylene ether) copolymers containing sulfonic acid groups on the pendants for proton exchange membrane materials, Macromolecules, 40 (2007) 9435-9442.

[27] M.A. Hickner, H. Ghassemi, Y.S. Kim, B.R. Einsla, J.E. McGrath, Alternative polymer systems for proton exchange membranes (PEMs), Chem. Rev., 104 (2004) 4587-4611.
[28] S.M. Javaid Zaidi, T. Matsuura, Polymer membranes for fuel cells, (2009).
[29] T.A. Zawodzinski, M. Neeman, L.O. Sillerud, S. Gottesfeld, Determination of water diffusion-coefficients in perfluorosulfonate ionomeric membranes, J. Phys. Chem., 95 (1991) 6040-6044.
[30] M.L. Einsla, Y.S. Kim, M. Hawley, H.S. Lee, J.E. McGrath, B.J. Liu, M.D. Guiver, B.S. Pivovar, Toward improved conductivity of sulfonated aromatic proton exchange membranes at low relative humidity, Chem. Mater., 20 (2008) 5636-5642.
[31] Y. Sone, P. Ekdunge, D. Simonsson, Proton conductivity of Nafion 117 as measured by a four-electrode AC impedance method, J. Electrochem. Soc., 143 (1996) 1254-1259.
[32] F. Barbir, PEM fuel cells : theory and practice in, Boston : Elsevier Academic Press, 2005.
[33] T.A. Zawodzinski, C. Derouin, S. Radzinski, R.J. Sherman, V.T. Smith, T.E. Springer, S. Gottesfeld, Water-uptake by and transport through Nafion® 117 membranes, J. Electrochem. Soc., 140 (1993) 1041-1047.
[34] H.E. Darling, Conductivity of sulfuric acid solutions, J. of Chem. Eng. Data, 9 (1964) 421-426.
[35] V. Grotthuss, C.J.D., Ann. Chim, (1806) 58.
[36] K.D. Kreuer, A. Rabenau, W. Weppner, Vehicle mechanism, a new model for the interpretation of the conductivity of fast proton conductors, Angew. Chem. Int. Ed., 21 (1982) 208-209.
[37] S. Ma, Z. Siroma, H. Tanaka, Anisotropic conductivity over in-plane and thickness directions in Nafion-117, J. Electrochem. Soc., 153 (2006) A2274-A2281.
[38] K.D. Kreuer, S.J. Paddison, E. Spohr, M. Schuster, Transport in proton conductors for fuel-cell applications: Simulations, elementary reactions, and phenomenology, Chem. Rev., 104 (2004) 4637-4678.
[39] J.A. Dura, V.S. Murthi, M. Hartman, S.K. Satija, C.F. Majkrzak, Multilamellar interface structures in Nafion, Macromolecules, 42 (2009) 4769-4774.
[40] A.L. Rollet, O. Diat, G. Gebel, A new insight into Nafion structure, J. Phys. Chem. B, 106 (2002) 3033-3036.
[41] E.J. Roche, M. Pineri, R. Duplessix, Phase-separation in perfluorosulfonate ionomer membranes, J. Polym. Sci., Part B: Polym. Phys., 20 (1982) 107-116.
[42] E.J. Roche, M. Pineri, R. Duplessix, A.M. Levelut, Small-angle scattering studies of Nafion membranes, J. Polym. Sci., Part B: Polym. Phys., 19 (1981) 1-11.
[43] K.D. Kreuer, On the development of proton conducting polymer membranes for hydrogen and methanol fuel cells, J. Membr. Sci., 185 (2001) 29-39.
[44] H.G. Haubold, T. Vad, H. Jungbluth, P. Hiller, Nano structure of Nafion: a SAXS study, Electrochim. Acta, 46 (2001) 1559-1563.
[45] A.V. Krivandin, A.B. Solov'eva, N.N. Glagolev, O.V. Shatalova, S.L. Kotova, Structure alterations of perfluorinated sulfocationic membranes under the action of ethylene glycol (SAXS and WAXS studies), Polymer, 44 (2003) 5789-5796.
[46] T. Xue, J.S. Trent, K. Osseoasare, Characterization of Nafion membranes by transmission electron-microscopy, J. Membr. Sci., 45 (1989) 261-271.
[47] A.L. Rollet, J. Blachot, A. Delville, O. Diat, A. Guillermo, P. Porion, L. Rubatat, G. Gebel, Characterization of porous structure through the dynamical properties of ions confined in sulfonated polyimide ionomers films, Eur. Phys. J. E, 12 (2003) S131-S134.

[48] J. Li, K.G. Wilmsmeyer, L.A. Madsen, Hydrophilic channel alignment modes in perfluorosulfonate ionomers: Implications for proton transport, Macromolecules, 41 (2008) 4555-4557.
[49] P.J. Basser, J. Mattiello, D. Lebihan, Estimation of the effective self-diffusion tensor from the NMR Spin-Echo, J. Magn. Reson. B, 103 (1994) 247-254.
[50] Y.G. Yin, C.H. Zhao, S. Kuroki, I. Ando, Diffusion of rodlike polypeptides with different main-chain lengths in the thermotropic liquid crystalline state as studied by the field-gradient ^{1}H NMR method, Macromolecules, 35 (2002) 2335-2338.
[51] J.G. Kirkwood, J. Polym. Sci., 12 (1954) 1.
[52] M. Doi, S.F. Edwards, The theory of polymer dynamics, Oxford University Press, USA, (1988).
[53] S. Hess, D. Frenkel, M.P. Allen, On the anisotropy of diffusion in nematic liquid-crystals - test of a modified affine transformation model via molecular-dynamics, Mol. Phys., 74 (1991) 765-774.
[54] Y. Bar-Cohen, Biomimetics using electroactive polymers (EAP) as artificial muscles - A review, J. Adv. Mater. Covina, 38 (2006) 3-9.
[55] K. Sadeghipourt, R. Salomon, S. Neogi, Development of a novel electrochemically active membrane and 'smart' material-based vibration sensor/damper, Smart Mater. Struct., 1 (1992) 172-179.
[56] M.D. Bennett, D.J. Leo, Ionic liquids as stable solvents for ionic polymer transducers, Sensor Actuat. A-Phys., 115 (2004) 79-90.
[57] Y. Bar-Cohen, Electroactive polymers as artificial muscles: A review, J. Spacecraft Rockets, 39 (2002) 822-827.
[58] B.J. Akle, M.D. Bennett, D.J. Leo, High-strain ionomeric-ionic liquid electroactive actuators, Sensor Actuat. A-Phys., 126 (2006) 173-181.
[59] M.D. Bennett, D.J. Leo, G.L. Wilkes, F.L. Beyer, T.W. Pechar, A model of charge transport and electromechanical transduction in ionic liquid-swollen Nafion membranes, Polymer, 47 (2006) 6782-6796.
[60] Y. Liu, Ionic polymer composite actuators, Ph.D. dissertation, (2012).
[61] S. Liu, R. Montazami, Y. Liu, V. Jain, M.R. Lin, J.R. Heflin, Q.M. Zhang, Layer-by-layer self-assembled conductor network composites in ionic polymer metal composite actuators with high strain response, Appl. Phys. Lett., 95 (2009).
[62] S. Liu, W.J. Liu, Y. Liu, J.H. Lin, X. Zhou, M.J. Janik, R.H. Colby, Q.M. Zhang, Influence of imidazolium-based ionic liquids on the performance of ionic polymer conductor network composite actuators, Polym. Int., 59 (2010) 321-328.
[63] I. Krossing, J.M. Slattery, C. Daguenet, P.J. Dyson, A. Oleinikova, H. Weingartner, Why are ionic liquids liquid? A simple explanation based on lattice and solvation energies, J. Am. Chem. Soc., 128 (2006) 13427-13434.
[64] M. Armand, F. Endres, D.R. MacFarlane, H. Ohno, B. Scrosati, Ionic-liquid materials for the electrochemical challenges of the future, Nature Mater., 8 (2009) 621-629.
[65] T. Welton, Room-temperature ionic liquids. Solvents for synthesis and catalysis, Chem. Rev., 99 (1999) 2071-2083.
[66] F. Vidal, C. Plesse, D. Teyssie, C. Chevrot, Long-life air working conducting semi-IPN/ionic liquid based actuator, Synth. Met., 142 (2004) 287-291.

Chapter 2

Molecular Diffusion and NMR Spectroscopy

2.1 Diffusion Fundamentals

Molecular self-diffusion is a stochastic process driven by thermal fluctuation that exists universally. Its fundamental significance lies in the fact that many key process such as chemical reactions and mass transfer strongly depend on molecular diffusion.[1,2] The study of molecular self-diffusion reveals important information regarding molecular dynamics and particle sizes since diffusion coefficient *D* directly couples to dynamic and structural parameters such as temperature and hydrodynamic radius through the famous Stokes-Einstein relationship[3]:

$$D = \frac{kT}{c\eta r_H} \qquad (2.1.1)$$

where *k* is the Boltzmann constant, *T* is absolute temperature, *c* is a constant factor depending on the shape, stick or slip boundary conditions and relative size of the diffusing particle to its surrounding fluid,[4] η is fluid viscosity, and r_H is the diffusing particle's hydrodynamic radius.

Fick's first law describes the diffusion process in the presence of a concentration gradient:

$$\boldsymbol{J}(\boldsymbol{r}, t) = -D\nabla c(\boldsymbol{r}, t) \qquad (2.1.2)$$

D is a scalar for isotropic diffusion, $\boldsymbol{J}(\boldsymbol{r}, t)$ and $c(\boldsymbol{r}, t)$ denote particle flux and concentration, respectively. For anisotropic diffusion, *D* becomes a 3×3 tensor matrix. The negative sign indicates that particles diffuse in the opposite direction of the concentration gradient, *i.e.* from high concentration to low concentration. The following equation defines the law of mass conservation:

$$\frac{\partial c(\boldsymbol{r},t)}{\partial t} = -\nabla \cdot \boldsymbol{J}(\boldsymbol{r},t) \qquad (2.1.3)$$

Combining equation (2.1.2) and (2.1.3), one obtains Fick's second law:

$$\frac{\partial c(\boldsymbol{r},t)}{\partial t} = D\nabla^2 c(\boldsymbol{r},t) \qquad (2.1.4)$$

Under equilibrium conditions, the conditional probability $\mathrm{P}(\vec{\mathrm{r}}_\mathrm{i}, \vec{\mathrm{r}}_\mathrm{e}, \Delta)$ usually applies to describe molecular self-diffusion. Here $\mathrm{P}(\vec{\mathrm{r}}_\mathrm{i}, \vec{\mathrm{r}}_\mathrm{e}, \Delta)$ denotes the probability for a diffusing particle to move from $\vec{\mathrm{r}}_\mathrm{i}$ to $\vec{\mathrm{r}}_\mathrm{e}$ within a diffusion time Δ. Onsager's dissipation theory[5] indicates that $\mathrm{P}(\vec{\mathrm{r}}_\mathrm{i}, \vec{\mathrm{r}}_\mathrm{e}, \Delta)$ is governed by the same rule described by Fick's law, therefore the following equation applies:

$$\frac{\partial \mathrm{P}(\vec{\mathrm{r}}_\mathrm{i}, \vec{\mathrm{r}}_\mathrm{e}, \Delta)}{\partial t} = D\nabla^2 \mathrm{P}(\vec{\mathrm{r}}_\mathrm{i}, \vec{\mathrm{r}}_\mathrm{e}, \Delta) \qquad (2.1.5)$$

For free boundary conditions (free diffusion), one can easily derive the solution to equation (2.1.5):

$$\mathrm{P}(\vec{\mathrm{r}}_\mathrm{i}, \vec{\mathrm{r}}_\mathrm{e}, \Delta) = \frac{1}{(4\pi \mathrm{D}\Delta)^{3/2}} \exp\left(-\frac{(\vec{\mathrm{r}}_\mathrm{e} - \vec{\mathrm{r}}_\mathrm{i})^2}{4\mathrm{D}\Delta}\right) \qquad (2.1.6)$$

Let $\mathbf{R} = \vec{\mathrm{r}}_\mathrm{e} - \vec{\mathrm{r}}_\mathrm{i}$, equation (2.1.6) reduces to equation (2.1.7):

$$\mathrm{P}(\mathbf{R}, \Delta) = \frac{1}{(4\pi \mathrm{D}\Delta)^{3/2}} \exp\left(-\frac{\mathbf{R}^2}{4\mathrm{D}\Delta}\right) \qquad (2.1.7)$$

Equation (2.1.7) is an even function which has the form of the Gaussian distribution. Information on average molecular displacement can be calculated via the first and second moment of **R**:

$$< R > = \int_{\mathbf{0}}^{\boldsymbol{2\pi}} d\varphi \int_0^{\pi} \sin\theta \, d\theta \int_0^{\infty} \mathrm{R}^3 \, \mathrm{P}(\mathrm{R}, \Delta) \mathrm{dR} \qquad (2.1.8)$$

$$= 0$$

$$< \mathbf{R^2} > = \int_{\mathbf{0}}^{\boldsymbol{2\pi}} d\varphi \int_0^{\pi} \sin\theta \, d\theta \int_0^{\infty} \mathrm{R}^4 \, \mathrm{P}(\mathrm{R}, \Delta) \mathrm{dR}$$

$$= \int_0^{\infty} \frac{1}{(4\pi D\Delta)^{\frac{3}{2}}} \exp\left(-\frac{\mathbf{R}^2}{4D\Delta}\right) 4\pi R^4 \, dR$$

$$= 6D\Delta \qquad (2.1.9)$$

Equation (2.1.9) suggests that the average molecular diffusion length varies with the square root of diffusion time, which is associated with the stochastic nature of diffusion. In recognition that the above result is derived under the condition of free diffusion, deviations from equation (2.1.9) usually signify the presence of local barriers at relevant diffusion lengths, typically 0.1-10 μm, such as structural heterogeneity or domain boundary etc. inside polymeric materials. Therefore, diffusion measurements act as a ruler with a tunable scale, allowing us to map out the profile of local structure.

2.2 Lattice Model for Diffusion

One convenient way to depict molecular diffusion is to visualize the process as a series of consecutive jumps on a three dimensional lattice. For simplification, we assume that the root-mean-square value of each step is l and τ is the mean time between each successive jump. To further simplify the problem, we only consider molecular jumps in one dimension and molecules can either jump forward or backward as shown in figure 2.1:

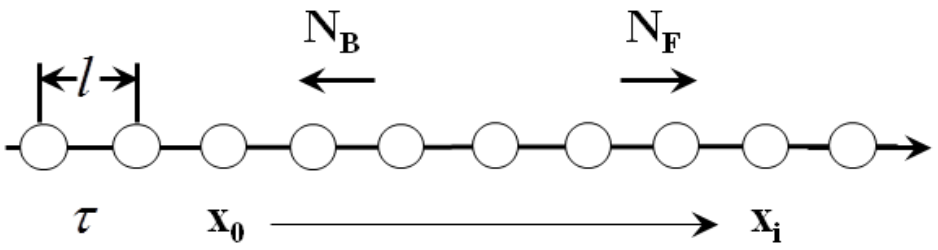

Figure 2.1. Illustration of one dimensional molecular jumps

l and τ are the root mean square value of step size and mean time interval between each step. For a given molecule, it takes N_F steps forward and N_B steps backward to move from x_0 to x_i.

N_B and N_F correspond to the number of steps backward and forward, respectively. For any given molecule, x_i-x_0 represents the net molecular displacement. Under the framework of free diffusion, molecules have no particular tendency to jump forward or backward but move in either direction with an equal probability, *i.e.* $P_F = P_B = \frac{1}{2}$. After $N = N_F + N_B$ jumps, the probability for a molecule to move from x_0 to x_i follows the binominal distribution:

$$P(x_0, x_i, N\tau) = \frac{N!}{N_F!\, N_B!}(\frac{1}{2})^{N_F}(\frac{1}{2})^{N_B} \quad (2.2.1)$$

Under the constraint $N = N_F + N_B$, we substitute x_i-$x_0 = (N_F - N_B)l$ into (2.2.1), P becomes solely a function of N and x_i-x_0. In the limit of large N, Stirling's approximation simplifies equation (2.2.1) into:

$$P(x_0, x_i, N\tau) = \sqrt{\frac{1}{2\pi N l^2}} \exp(-\frac{(x_i - x_0)^2}{2Nl^2}) \quad (2.2.2)$$

The total jumping time (diffusion time) is $\Delta = N\tau$ and the diffusion coefficient is $D = \frac{l^2}{2\tau}$. As a result, equation (2.2.2) becomes:

$$P(x_0, x_i, \Delta) = \sqrt{\frac{1}{4\pi D\Delta}} \exp(-\frac{(x_i - x_0)^2}{4D\Delta}) \quad (2.2.3)$$

Equation (2.2.3) represents the conditional probability for free molecular diffusion on one dimensional lattice. This result can be further extended to three dimensions. For isotropic diffusion, the conditional probability in three dimensions becomes the product of its correspondence in three orthogonal directions:

$$P(\vec{r}_0, \vec{r}_i, \Delta) = P(x_0, x_i, \Delta) \times P(y_0, y_i, \Delta) \times P(z_0, z_i, \Delta)$$

$$= \left(\frac{1}{4\pi D\Delta}\right)^{\frac{3}{2}} \exp\left(-\frac{(x_i - x_0)^2 + (x_i - x_0)^2 + (x_i - x_0)^2}{4D\Delta}\right)$$

$$= \left(\frac{1}{4\pi D\Delta}\right)^{\frac{3}{2}} \exp\left(-\frac{(\vec{r}_i - \vec{r}_0)^2}{4D\Delta}\right) \qquad (2.2.4)$$

Clearly, equation (2.2.4) is identical to equation (2.1.6) though they start from different viewpoints. Equation (2.2.4) is a direct consequence of the central limit theorem (CLT), which states that the mean value in the presence of a sufficient number of independent random steps will approach to normal distribution (Gaussian). This conclusion further implies that the physical meaning of *D* is associated with long time dynamics. Therefore, molecular translational motions under extremely short time scales (< ps) are beyond the scope of our current discussion.

2.3 Diffusion in Porous Media

Diffusion in porous media is a ubiquitous phenomenon observed in many biological, physical, chemical, material and geological systems. This phenomenon plays a significant role in many aspects of life and industry, encompassing biological tissues,[6] nanofiltration,[7] gas permeation[8] and chemical reactions.[2] Molecular motions are hindered when traveling in the structural labyrinth of materials matrix. Structural characteristics and geometrical factors, including orientation and molecular shape anisotropy,[9,10] pore size distribution,[11] inter-pore connectivity and tortuosity,[6,12] all dramatically impact the measured diffusion coefficient. The establishment of a general protocol to explicitly interpret the diffusion results represents a key step toward understanding how structures affect transport in complex materials.

Ionomer membranes, for example, can be modeled as porous media. One useful strategy of studying diffusion in porous structures is to measure *D* as a function of the diffusion time Δ. Domain characteristics (boundary, orientation, size, etc.) constantly modulate molecular motions

and thereby leave a fingerprint of local structures on the measured molecular diffusion coefficient: time-dependent diffusion coefficient that D varies with Δ. In general, there are two types of pore geometries to be considered: closed pores (isolated) and open pores (interconnected) as shown in figure 2.2.

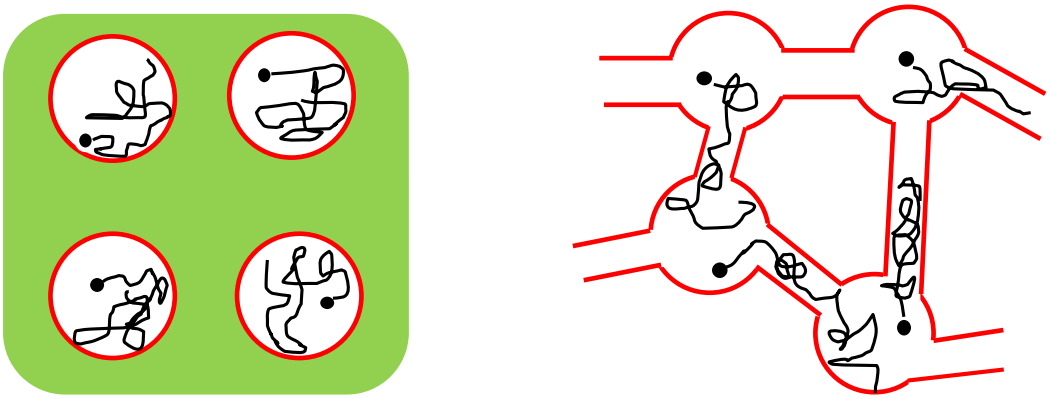

(a). Isolated porous structure **(b). Interconnected porous structure**

Figure 2.2. (a) Isolated pores and (b) interconnected pores in porous media

(a) Molecular diffusion is confined in isolated pores and D reduces to zero when Δ is adequately long. (b) For interconnected pores, D decreases to a nonzero plateau value that relies on the tortuosity of the pore matrix.

In their seminal paper, Mitra and coworkers pointed out that diffusion measurement in the short time regime (diffusion length << pore size) yielded information on the surface to volume ratio of the confining pore structure,[13] regardless of the local pore geometry:

$$D_{app} = D_0\left(1 - \frac{4}{9\sqrt{\pi}}\frac{S}{V}\sqrt{D_0\Delta}\right) \qquad (2.3.1)$$

D_{app} is the measured apparent diffusion coefficient and D_0 is the so called "unbounded" diffusion coefficient. D_0 is normally the diffusion coefficient one would measure for a pure

liquid without any restriction. $\frac{S}{V}$ corresponds to the surface to volume ratio of the pore matrix. The above equation can be understood in this way: When diffusion time Δ is short, only molecules in the vicinity of structural boundaries feel the obstruction and bounce back upon collision to yield an apparent slower diffusion coefficient. The number of these "restricted" molecules is proportional to the volume they occupy, as determined by the product of accessible surface area and diffusion length, *i.e.* $S\sqrt{D_0\Delta}$. When divided by the total volume, $\frac{S}{V}\sqrt{D_0\Delta}$ denotes the relative ratio of restricted molecules.

On the other hand, D_{app} in the long Δ regime diminishes to zero for isolated pores but plateaus to a specific value D_∞ for open pore structures. Such a signature allows one to distinguish isolated pores from interconnected pores. In the intermediate regime, a universal model relating diffusion coefficient to local structural environment does not exist due to structural complexity in different systems. However, the Padé approximation usually interpolates well between short and long time regimes as shown in the following:[12,14]

$$D_{app} = D_0\left(1 - \eta\frac{\sqrt{\alpha t} + \beta t}{\sqrt{\alpha t} + \beta t + \eta}\right) \qquad (2.3.2)$$

Here $\eta = 1 - \frac{1}{\Im}$ and $\Im = \frac{D_0}{D_\infty}$, which quantifies the tortuosity. $\alpha = D_0\left(\frac{4}{9\sqrt{\pi}}\frac{S}{V}\right)^2$ and β is the fitting parameter that relates macroscopic homogeneity length scale L_{macro} to D_0 as $\beta = \frac{D_0}{L_{macro}^2}$.

2.4 Nuclear Magnetic Resonance Spectroscopy

2.4.1 Principles of Spin ½ NMR

NMR spectroscopy finds expanding applications in analyzing intricate molecular interactions, probing dynamics and unraveling structural heterogeneities in many important

materials systems. Its basic principle lies in the fact that the spin of nuclei will redistribute and orient in the presence of an external magnetic field. For illustration, figure 2.3 depicts the distribution of different states for an ensemble of spin ½ nuclei in the absence (a) or presence (b) of a magnetic field.

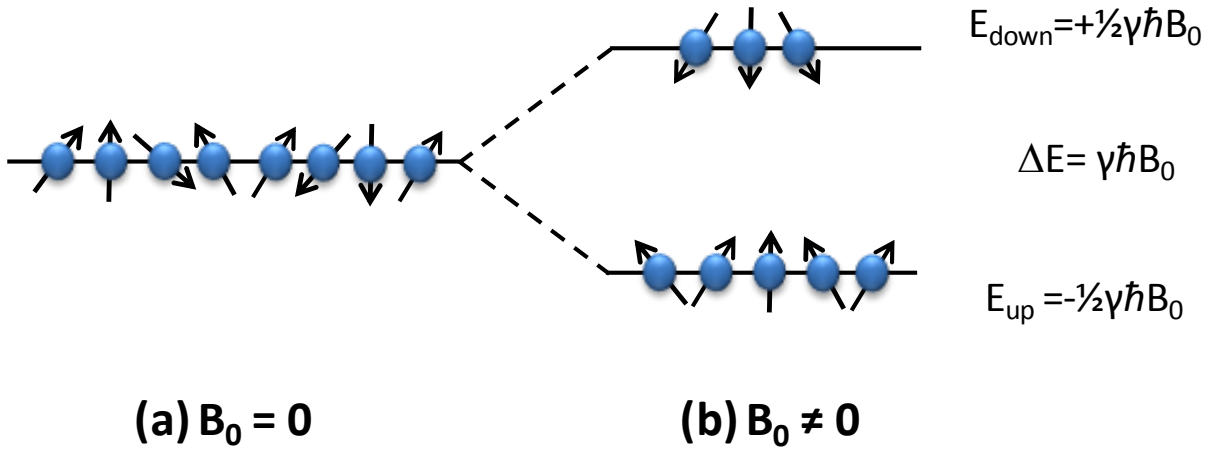

Figure 2.3. Population distribution of spin states for spin ½ nuclei

(a) The magnetic field $B_0=0$ (b) The magnetic field $B_0\neq0$. In zero field, all spins are degenerate and thus there is no population difference. In case (b), a splitting in energy levels results in a population difference between the two spin states.

Quantum mechanics predicts $2\times1/2+1=2$ possible states for spin ½ nuclei with regard to the azimuthal (z) component of the magnetization, m_z: $m_z = ½$ and $m_z = –½$, which correspond to the spin-up and spin-down states. No energy difference exists among these two spin states when $B_0=0$ and the spin magnetization is zero. When nuclear ensembles are exposed to the $B_0\neq0$, the energy level associated with each spin state will shift up or down by $½\gamma\hbar B_0$. γ is the gyromagnetic ratio of the nucleus. This shift in energy levels will bias the spin population in different states and their population difference yield the net spin polarization that fundamentally determines NMR signal intensity. We normally use the Larmor frequency $\boldsymbol{\omega_0} = \gamma B_0$ to represent

the energy difference $\Delta E = \frac{1}{2}\gamma\hbar B_0 - (-\frac{1}{2})\gamma\hbar B_0 = \gamma\hbar B_0$. A radio frequency magnetic field can be used to excite magnetic resonance and generate coherence transverse to B_0, which is detected as the free induction decay (FID) by the receiver coil. This oscillating signal has the form of $I = I_0 \sum_i \exp(i\omega_i t) \times \exp(-t/T_{2,i})$ in the time domain, which is Fourier transformed (FT) to yield a frequency domain spectrum, as shown in figure 2.4. The index i denotes nuclei with different Larmor frequencies.

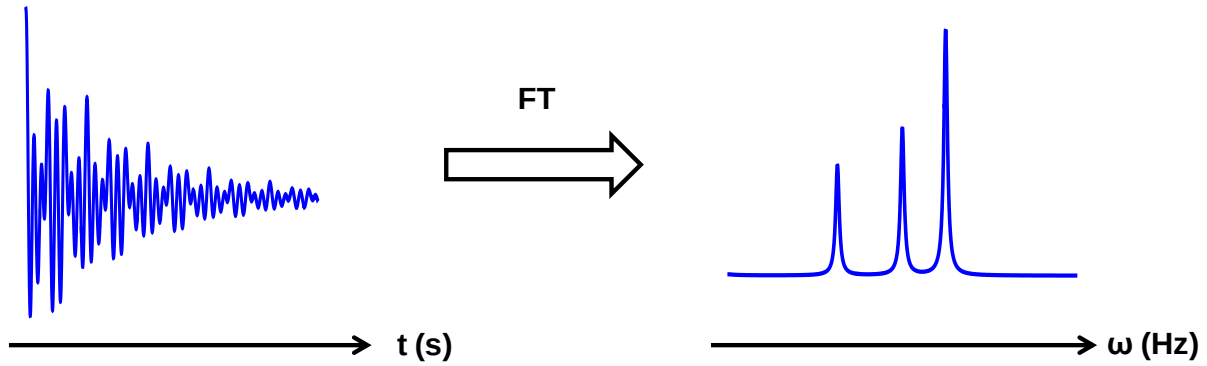

Figure 2.4. Fourier transform of a time domain signal into a frequency domain spectrum

The FT does not yield any extra information but significantly eases data interpretation. The NMR frequency spectrum contains a wealth of information with respect to chemical composition, molecular structure, symmetry, couplings and dynamics.

2.4.2 Orientational Order Measurement using ^{2}H NMR

^{2}H is a quadrupolar nucleus with important NMR applications regardless of its low natural abundance.[15-17] The interaction between the nuclear electric quadrupole moment and the local electric field gradient *e.g.* in a molecular bond provides critical information regarding material phase symmetry,[17] orientational order[18] and defects in local structures.[9] Unlike other quadrupolar nuclei, the relatively small quadrupole moment of ^{2}H makes deuterated molecules good candidates for characterizing local structures of soft materials, such as liquid crystals and

polymers. The quadrupole interaction arises from the electric field gradient along the C-D bond axis associated with the molecular orbital of labeled molecules as shown in figure 2.5.

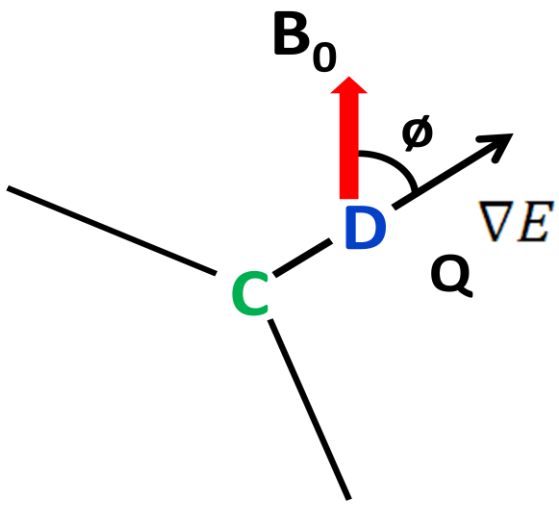

Figure 2.5. Orientation of a C-D bond with respect to the spectrometer field B_0

ϕ is the angle between C-D bond and the spectrometer magnetic field direction B_0. Q is the quadrupole moment of deuterium. ∇E denotes the electric field gradient, which typically lies along the direction of the C-D bond.

Here C may be any possible nucleus in general. For a probe molecule whose C-D bond is oriented at an angle ϕ with respect to B_0, the quadrupole interaction Hamiltonian has the following form:

$$H_{(Q)} = \frac{3eV_zQ}{4I(2I-1)}(3I_z^2 - I^2)P_2(\cos\phi) \qquad (2.4.1)$$

V_z is the electric field gradient, Q is the nuclear electric quadrupole moment, I is the spin quantum number, $P_2(\cos\phi) = \frac{1}{2}(3\cos^2\phi - 1)$ is the second Legendre polynomial term and ϕ is the angle of the C-D bond relative to B_0.

In the context of structural analysis, probe molecules diffuse in the tortuous matrix and sense the structural profile. C-D bond orientations can "probe" local rotational barriers to mimic structure anisotropy. The statistical value of $P_2(\cos\phi)$ diminishes to zero for an isotropic environment and gives only one peak in the spectrum. Otherwise, quadrupolar interactions do not vanish in the presence of average orientational anisotropy. Shifts in the spin energy levels cause non-equivalent transition energies as shown in figure 2.6.

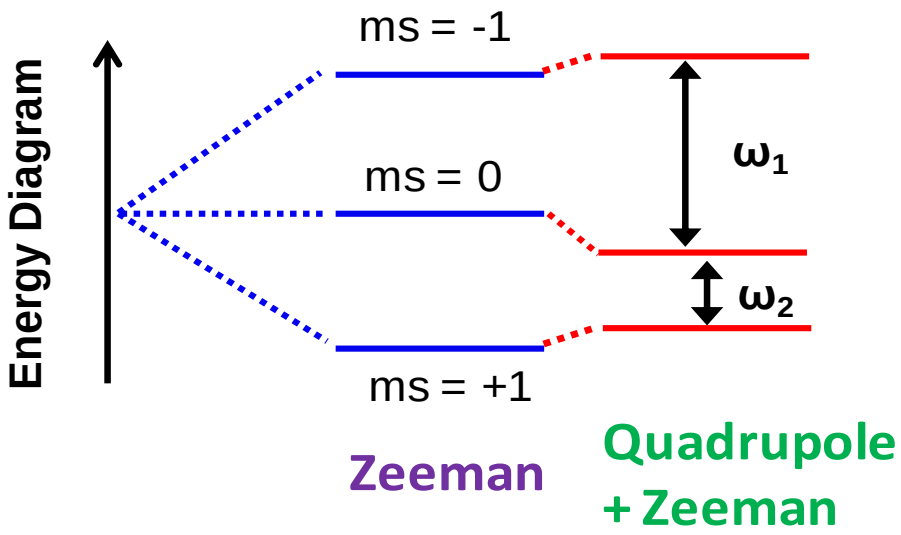

Figure 2.6. Shift of energy levels for a quadrupolar nucleus (I=1) in a magnetic field

The quadrupole interaction shifts energy levels resulting in nonequivalent energy differences among spin states and thus lead to peak splittings.

As a result, one observes peak splittings in the spectrum (figure 2.7), as described by the following equation:[18]

$$\Delta\nu = Q \times S \times P_2(\cos\theta) \qquad (2.4.2)$$

Q is the quadrupole coupling constant (~ 260 kHz for O-D bond), S is the orientational order parameter and θ is the angle between B_0 and average alignment of the studied material.

Informatively, equation 2.4.2 allows determination of the symmetry axis for uniaxially aligned systems. Quantification of the orientational order parameter *S* is also viable in combination with other supplementary information, such as X-ray scattering. In concert with diffusion anisotropy measurements, insights into local structural defects can also be obtained.

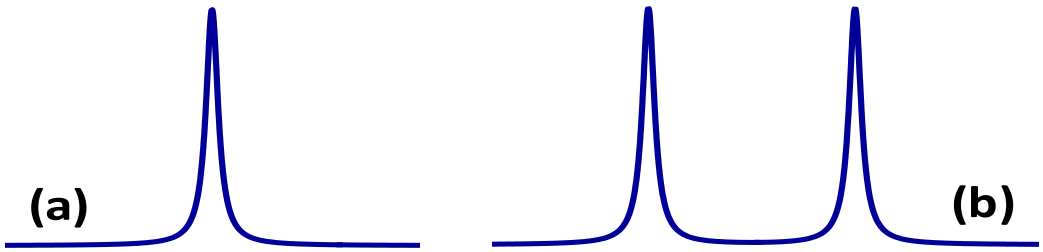

Figure 2.7. Representative ^{2}H spectra for (a) isotropic and (b) anisotropic materials

A single peak appears in the spectrum for the isotropic sample and a doublet in the aligned sample. Peak splittings are proportional to the orientational order *S* of the anisotropic material and also depend on the $P_2(\cos\theta)$ term.

2.5 Pulsed-Field-Gradient NMR: Experiment and Theory

Pulsed-field-gradient (PFG) NMR represents a powerful tool for measuring molecular displacement, thereby providing an accurate, tunable and sensitive probe of molecular self-diffusion.[1,19] The method allows a wide range assessment of molecular motions by means of its chemical selectivity and long coherence times. This technique utilizes magnetic field gradients (spatially varying magnetic fields) to label the initial and final positions of molecular ensembles, which are further coupled with the detected NMR signal to determine the self-diffusion coefficient *D* for one or more species in a material.[19-21] Figure 2.8 schematically shows how molecular self-diffusion is measured using a typical pulsed gradient spin echo (PGSE) sequence.

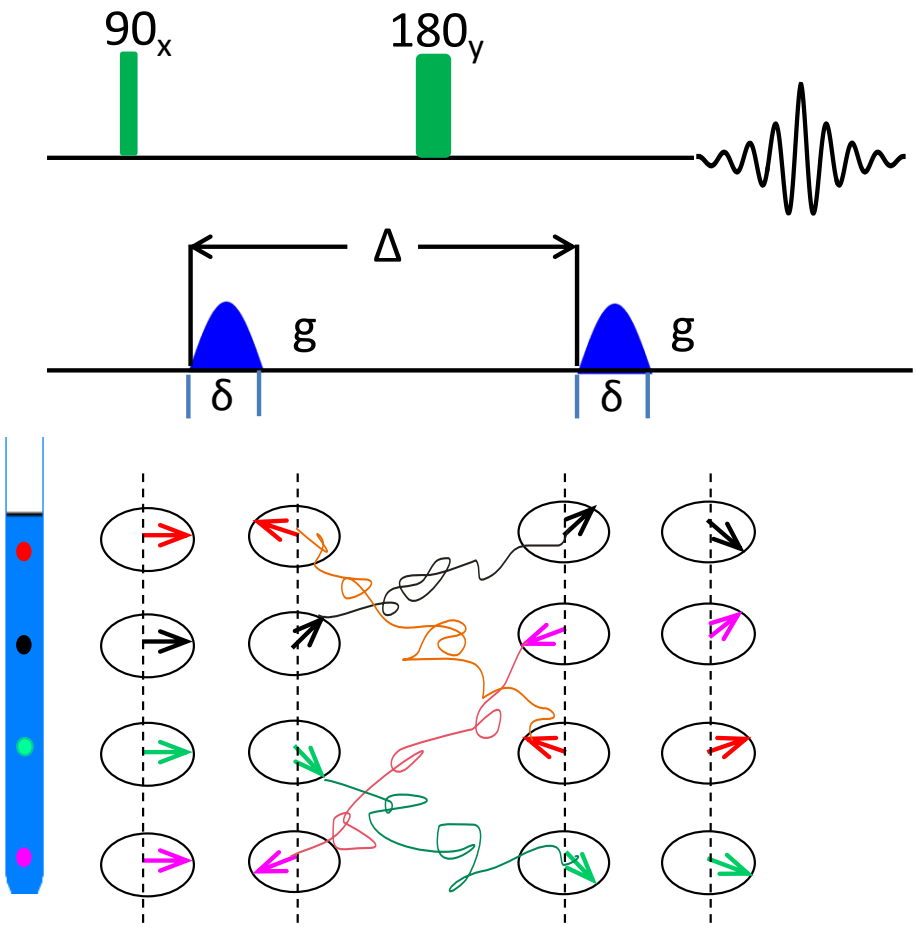

Figure 2.8. Illustration of molecular diffusion during the PGSE pulse sequence

Different color spots represent molecules at different positions along the vertical NMR tube. The corresponding colored arrows denote spin magnetization in the transverse plane. The gradient pair encodes and decodes the phase memory of the spin magnetization ensemble. Random molecular motions allow only partial preservation of the phase coherence over the whole sample, which leads to NMR signal attenuation.

The 90 degree pulse excites spin energy level transitions and introduces magnetization phase coherence into the transverse plane. Local spin magnetization precesses at the same rate in the absence of magnetic field inhomogeneity and all spin magnetization elements point along the

same direction. The first gradient pulse completely distorts the phase coherence by introducing a spatially distributed phase angle. The phase angle Φ_i varies continuously in space and forms a helix profile along the gradient direction. The pitch of the helix relates to parameters, such as gyromagnetic ratio (γ), gradient strength (g) and duration (δ). Such a process is called encoding since it establishes a relationship between spin phase angle and molecular position. A subsequent 180_y degree pulse inverts the spin magnetization with respect to the y axis, followed by a second decoding gradient, with the purpose of counteracting the effect of the first gradient. However, random molecular motions during the diffusion time Δ cause the final phase angle Φ_e to deviate from Φ_i, which leads to partial phase cancellation, *i.e.* NMR signal attenuation. Thus, explicit correlation between molecular displacement $|\vec{r}_e - \vec{r}_i|$ and signal attenuation allows quantification of molecular self-diffusion, $D = \frac{|\vec{r}_e - \vec{r}_i|^2}{2\Delta}$.

Alternatively, the pulse gradient stimulated echo (PGSTE) sequence is also commonly used for diffusion measurements. This method has the advantage that signal relaxes with a T_1 longitudinal (spin-lattice) relaxation rather than the T_2 transverse relaxation time during diffusion time Δ. As shown in figure 2.7, PGSTE consists of three 90 rf. pulses where the second one stores the magnetization along the z direction to relax primarily via T_1 processes. $T_1 >> T_2$ for most of our soft material systems and PGSTE usually exhibits much better signal sensitivity than PGSE method.

In general, there are two types of approximations involved in NMR signal analysis: the small (narrow) gradient pulse (SGP) approximation and the Gaussian phase distribution (GPD). As mentioned earlier, a pair of transient magnetic field gradients impart phase memory to individual spin bearing molecule. This memory instantaneously couples to molecular intial ($\mathbf{r_i}$) and final positions ($\mathbf{r_e}$) as shown in equations (2.5.1) and (2.5.2):

$$\Phi_i = \gamma \int_0^{\delta} \vec{g}(t)\vec{r}_i(t)dt \qquad (2.5.1)$$

$$\Phi_e = \gamma \int_{\Delta}^{\Delta+\delta} \vec{g}(t)\vec{r}_e(t)dt \qquad (2.5.2)$$

where γ is the gyromagnetic ratio, $\vec{g}(t)$ is the time dependent gradient pulse, $\vec{r}(t)$ denotes the instantaneous spatial location of an individual molecule at time t. As shown in equation (2.5.3) and (2.5.4), net phase accumulated by individual spins, which contains information regarding molecular diffusion (time-dependent position) is superimposed and folded into NMR signal amplitude:

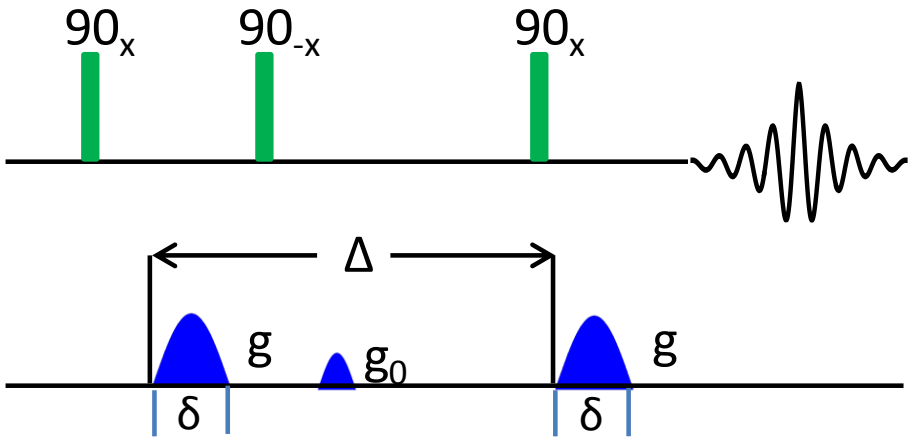

Figure 2.9. Schematic of the PGSTE pulse sequence

The second rf pulse stores half of the total spin magnetization along the longitudinal direction. The stimulated echo forms after the third rf. pulse. A spoil gradient (g_s) follows the second rf pulse to dephase the transverse spin magnetization to avoid the formation of a spin echo which would interfere with the stimulated echo.

$$I = I_0 \int_{-\infty}^{+\infty} \exp(i\Phi)\, d\Phi \qquad (2.5.3)$$

$$\Phi = \Phi_e - \Phi_i \qquad (2.5.4)$$

where Φ_i and Φ_e represent phase acquired by an individual spin during the first and second gradient pulses. The SGP approximation assumes an infinitely short gradient pulse so that $\vec{r}(t)$ remains constant with no diffusion (substantial) process taking place during δ. In case of rectangular shape gradient pulses, $\vec{g}=\vec{g}_0$ and equation (2.5.1) and (2.5.2) further simplify into equation (2.5.5) and (2.5.6):

$$\Phi_i = \gamma\delta\vec{g}_0\vec{r}_i \qquad (2.5.5)$$

$$\Phi_e = \gamma\delta\vec{g}_0\vec{r}_e \qquad (2.5.6)$$

For non-rectangular gradient pulses, one can use the effective gradient strength $\vec{g}_{eff}$ to substitute $\vec{g}_0$. Combining (2.5.1), (2.5.5) and (2.5.6), one obtains the following relationship:

$$I = \iint \boldsymbol{\rho}(\vec{r}_i)P(\vec{r}_i, \vec{r}_e, \Delta)\exp\left[\gamma\vec{g}_0\delta\left(\vec{r}_e - \vec{r}_i\right)\right]d\vec{r}_e d\vec{r}_i \quad (2.5.7)$$

$\boldsymbol{\rho}$ ($\vec{r}_i$) is the spin density, a constant in space for homogeneous materials that satisfies $\int \boldsymbol{\rho}(\vec{r}_i)d\vec{r}_i = 1$. $P(\vec{r}_i, \vec{r}_e, \Delta)$ is the conditional displacement distribution function of section 2.1, denoting the probability for an individual molecule to move from $\vec{r}_i$ to $\vec{r}_e$ within a diffusion time interval Δ. Onsager's dissipation theory indicates that $P(\vec{r}_i, \vec{r}_e, \Delta)$ follows the rule of Fick's law and the central limit theorem demonstrates its form as that of a Gaussian distribution:

$$P(\vec{r}_i, \vec{r}_e, \Delta) = \frac{1}{(4\pi D\Delta)^{3/2}}\exp\left(-\frac{(\vec{r}_e - \vec{r}_i)^2}{4D\Delta}\right) \quad (2.5.8)$$

where Δ is diffusion time, consistent with Figure 1 and D is the self-diffusion coefficient. The combination of equations (2.5.7) and (2.5.8) give the following equation:

$$I = I_0\ \exp(-\gamma^2\delta^2 g_0^2\, D\Delta) \qquad (2.5.9)$$

I_0 is the NMR signal intensity at zero gradient and I is the attenuated signal which allows derivation of the diffusion coefficient via NMR signal decay.

On the other hand, molecular diffusion of varying rates in a material in many cases violates the assumption of the SGP approximation since molecules do not remain static during the gradient pulses. As an alternative, one employs the GPD approximation for signal analysis to account for the finite gradient pulse duration, assuming the net phase Φ acquired by individual spin follows the Gaussian distribution.

$$\mathrm{P}(\Phi) = \frac{1}{(2 < \Phi^2 >)^{1/2}} \exp\left(-\frac{\Phi^2}{2 < \Phi^2 >}\right) \quad (2.5.10)$$

Here $< \Phi^2 >$ represents the mean square value of Φ. Combining equations (2.5.1), (2.5.2), (2.5.3) and (2.5.10), one obtains equations (2.5.11) and (2.5.12):

$$I = I_0 \exp\left(-\frac{< \Phi^2 >}{2}\right) \qquad (2.5.11)$$

$$< \Phi^2 > = \gamma^2 g^2 < \left(\int_0^{\delta} \vec{r}_i(t)dt - \int_{\Delta}^{\Delta+\delta} \vec{r}_e(t)dt\right)^2 >$$

$$= 2\gamma^2 g^2 \delta^2 \left(\Delta - \frac{\delta}{3}\right) \qquad (2.5.12)$$

Inserting (2.5.12) into (2.5.11), equation (2.5.10) becomes the famous Stejskal-Tanner equation:[20]

$$I = I_0 \exp\left(-\gamma^2 \delta^2 g^2 D\left(\Delta - \frac{\delta}{3}\right)\right) \qquad (2.5.13)$$

In contrast to use of the SGP approximation, equation (2.5.13) defines $\left(\Delta - \frac{\delta}{3}\right)$ as the effective diffusion time, which takes the duration of finite gradient pulse into account. In the long diffusion time limit ($\Delta \gg \delta$), these two approximations converge.

References

[1] W.S. Price, Pulsed-field gradient nuclear magnetic resonance as a tool for studying translational diffusion .1. Basic theory, Concepts Magn. Reson., 9 (1997) 299-336.
[2] A.O. Prytula, V.M. Fedirko, Y.M. Pohreliuk, Y.S. Matychak, Surface chemical reactions in processes of diffusion mass transfer, Defect Diffusion Forum, 237-240 (2005) 1312-1318.
[3] A. Einstein, On the Movement of Small Particles Suspended in Stationary Liquids Required by the Molecular-Kinetic Theory of Heat, Annalen der Physik 17 (1905) 549-560.
[4] J.T. Edward, Molecular Volumes and Stokes-Einstein Equation, J. Chem. Edu., 47 (1970) 261.
[5] D. Chandler, Introduction to Modern Statistical Mechanics, Oxford U. Press, New York (1987).
[6] L.L. Latour, K. Svoboda, P.P. Mitra, C.H. Sotak, Time-dependent diffusion of water in a biological model system, P. Natl. Acad. Sci. USA, 91 (1994) 1229-1233.
[7] A. Szymczyk, C. Labbez, P. Fievet, A. Vidonne, A. Foissy, J. Pagetti, Contribution of convection, diffusion and migration to electrolyte transport through nanofiltration membranes, Adv. Colloid Interface Sci., 103 (2003) 77-94.
[8] D. Lee, L. Zhang, S.T. Oyama, S. Niu, R.F. Saraf, Synthesis, characterization, and gas permeation properties of a hydrogen permeable silica membrane supported on porous alumina, J. Memb. Sci., 231 (2004) 117-126.
[9] J.B. Hou, J. Li, L.A. Madsen, Anisotropy and Transport in Poly(arylene ether sulfone) Hydrophilic-Hydrophobic Block Copolymers, Macromolecules, 43 (2010) 347-353.
[10] P. Wasterby, G. Oradd, G. Lindblom, Anisotropic water diffusion in macroscopically oriented lipid bilayers studied by pulsed magnetic field gradient NMR, J. Magn. Reson., 157 (2002) 156-159.
[11] P.T. Callaghan, K.W. Jolley, R.S. Humphrey, Diffusion of Fat and Water in Cheese as Studied by Pulsed Field Gradient Nuclear Magnetic-Resonance, J. Colloid Interface Sci., 93 (1983) 521-529.
[12] R.W. Mair, M.N. Sen, M.D. Hurlimann, S. Patz, D.G. Cory, R.L. Walsworth, The narrow pulse approximation and long length scale determination in xenon gas diffusion NMR studies of model porous media, J. Magn. Reson., 156 (2002) 202-212.
[13] P.P. Mitra, P.N. Sen, L.M. Schwartz, P. Ledoussal, Diffusion Propagator as a Probe of the Structure of Porous-Media, Phys. Rev. Lett., 68 (1992) 3555-3558.
[14] L.L. Latour, P.P. Mitra, R.L. Kleinberg, C.H. Sotak, Time-Dependent Diffusion-Coefficient of Fluids in Porous-Media as a Probe of Surface-to-Volume Ratio, J. Magn. Reson. A, 101 (1993) 342-346.
[15] D. Catalano, V. Domenici, A. Marini, C.A. Veracini, A. Bubnov, M. Glogarova, Structural and orientational properties of the ferro, antiferroelectric, and re-entrant smectic C* phases of ZLL7/* by deuterium NMR and other experimental techniques, J. Phys. Chem. B, 110 (2006) 16459-16470.
[16] V. Domenici, K. Fodor-Csorba, D. Frezzato, G. Moro, C.A. Veracini, Deuterium NMR evidences of slow dynamics in the nematic phase of a banana-shaped liquid crystal, Ferroelectrics, 344 (2006) 263-272.
[17] L.A. Madsen, T.J. Dingemans, M. Nakata, E.T. Samulski, Thermotropic biaxial nematic liquid crystals, Phys. Rev. Lett., 92 (2004).

[18] J. Li, K.G. Wilmsmeyer, L.A. Madsen, Hydrophilic channel alignment modes in perfluorosulfonate ionomers: Implications for proton transport, Macromolecules, 41 (2008) 4555-4557.
[19] C.S. Johnson, Diffusion ordered nuclear magnetic resonance spectroscopy: principles and applications, Prog. Nucl. Magn. Reson. Spectrosc., 34 (1999) 203-256.
[20] E.O. Stejskal, J.E. Tanner, Spin diffusion measurements: Spin echos in the presence of a time-dependent field gradient, J. Chem. Phys., 42 (1965) 288-292.
[21] P.S. Pregosin, Ion pairing using PGSE diffusion methods, Prog. Nucl. Magn. Reson. Spectrosc., 49 (2006) 261-288.

Chapter 3

Studying Slow Diffusion by Pulsed-field-Gradient NMR: New Insight into Alleviating Artifacts

3.1 Introduction

Pulsed-field-gradient (PFG) NMR[1,2] offers unprecedented opportunities for studying molecular motion, dynamics and imaging in many important fields, encompassing biological cells and tissues[3,4], neuro science[5] and polymer electrolytes.[6-8] Using the chemical specificity of NMR given by the spectrum, one may measure distinct diffusion coefficients for multiple species in a sample, and the sample may be either in or out of equilibrium. This method employs magnetic field-gradient pairs to encode molecular positions over an adjustable time period, thereby representing a powerful tool for probing molecular displacement on multiple length scales.[9,10] In particular, high magnetic field gradients become necessary for studying slow motions of macromolecules and diffusion in viscous media, such as concentrated polymer solutions,[11] viscous ionic liquid,[12] liquid crystals[13] and polymer electrolytes.[14] Meanwhile, one can fruitfully employ high gradients to study time-dependent diffusion behaviors of materials with restricted diffusion,[15] thus providing information about the average landscape for transport inside a material. High gradient strength also becomes a prerequisite in probing microstructural heterogeneities via q-space imaging which provides a wealth of information on structural features, such as pore size and geometry.[16-18]

Regardless of these promising aspects, application of high gradients can suffer from gradient transient effects such as eddy currents associated with the fast rise and fall times of the strong gradient pulse and gradient pair mismatch. Overlapping eddy currents duration and signal

acquisition can severely disturb the detected signal, resulting in intensity reduction, phase distortion, and inaccurate diffusion measurements.[19] Several approaches have been developed to minimize phase instability caused by eddy currents.[19,20] Commercial gradient probes utilize shielded gradient coils which introduce compensation currents to suppress eddy currents.[19] Nevertheless, limitations in hardware usually necessitate the use of a finite gradient delay time (~ 1 ms) to allow for complete eddy current decay prior to signal collection. Similarly, gradient pair mismatch[21] is another main source that influences NMR signal and leads to distorted spectra. Varying the amplitude and duration of compensation currents to control gradient transient effects are referred to as gradient preemphasis adjustments. A pair of well matched gradients and a good gradient preemphasis adjustment to minimize gradient delay time are desirable for measuring slow molecular motions on spins with short T_2.

However, a good gradient preemphasis adjustment is necessary but not sufficient to assure the removal of all the transient effects. One critical step in evaluating high gradient pulse reproducibility and stability after preemphasis adjustments is to perform gradient calibration. This process involves determining the gradient strength and examing artifacts that may disturb spectral appearance and diffusion measurements. Gradient strength can be calibrated using line width,[22] echo shape,[23] frequency shift[24] or by using a standard sample with known diffusion coefficient.[25] Another useful strategy for high gradient calibration[20] is to observe the echo maximum by applying a read gradient during the data acquisition time. Such a method has allowed calibrating gradient strength to 50 T/m.[26] However, depending on the gradient strength, the read gradient duration needs to be adjusted correspondingly, thereby making the method not convenient in general for diffusion studies. Currently, standard liquids with low gyromagnetic ratio (γ) nuclei, such as ^2H_2O, remain widely used for high gradient calibration.[15,17,25,27,28] This

method is desirable since anomalies such as eddy currents and gradient pulse instability are easily visualized as a phase disturbance in the diffusion spectrum or a variance of the measured diffusion coefficient with diffusion times Δ.[25,28] Yadav and coworkers[28] recently discussed the advantages of using molecules containing both low and high γ nuclei for a wide range of gradient calibration. Their measured ^2H_2O diffusion result using a wide range of gradient strengths well agreed with the gradient calibration at low intensity using ^1H_2O. They also argued that artifacts arising from eddy currents could be reduced if initial gradient calibration is performed at high gradient strength using ^2H_2O.

From the practical aspect, general users routinely adopt standard liquid samples that typically have a diffusion coefficient on the order of 10^{-9}-10^{-10} m^2/s. These liquid samples limit gradient calibration up to 1.5-4 T/m due to the high gamma of ^1H nuclei. For high gradients, the lack of standard viscous liquids (^1H) limits the range of gradient calibration. Therefore, liquid samples with low gamma nuclei are normally used for high gradient calibration. Here, we have demonstrated that such a method is not sensitive to gradient transient effects and not robust for high gradient calibration, which is not explicitly documented in the literature. We further reveal that sample dimension along the gradient direction plays the same role as the gradient transient effect. This feature can be utilized to suppress the gradient artifacts that appear in diffusion measurements.

In this study, we "optimize" gradient preemphasis values and follow a standard calibration protocol by measuring ^2H_2O diffusion in a ^2H_2O-^1H_2O mixture. We obtain ^2H_2O diffusion spectra with no phase distortion up to a gradient value of 9.4 T/m. Varying gradient strength and diffusion time consistently yield the same diffusion coefficient and normal signal decays. These experimental results appear to convince us of a well performing gradient system.

Unexpectedly, we encounter significant phase distortion when measuring glycerol diffusion with the same set of experimental parameters. In the worst case, the signal attenuation exhibits an artificial diffractive-like behavior. Such a counterintuitive phenomenon conveys that a well calibrated gradient system using low γ nuclei may not be amenable to measurements on slow diffusing high γ nuclei. Further quantitative analysis sheds light on the observed experimental paradox. We conclude that low γ nuclei calibration may mask the presence of seemingly negligible gradient transient effects, and these effects are exposed when observing high γ nuclei resulting in anomalous NMR signal decay. Thus, low γ nuclei can yield ill-calibrated gradient parameters, followed by misinterpretation of artificial signal decay as restricted diffusion. Our analysis also indicates that even viscous liquids bearing high gamma nuclei is employed for high gradient calibration, artificial signal decay may still occur when measuring slower diffusion coefficients. We further reveal that sample dimension along the gradient direction plays the same role as the gradient transient effect. This feature can be utilized to suppress the gradient artifacts that appear in diffusion measurements. After reoptimizing the gradient preemphasis using $^{1}H_2O$, we obtain greatly improved diffusion results on glycerol. These discoveries are of great significance to high gradient calibrations for q-space imaging as well as for studying slow motions in structurally complex systems.

3.2 Experimental

$^{2}H_2O$ (99.9% purity) and dry glycerol (> 99% purity) were purchased from Cambridge Isotope Labs and Acros Organics, respectively. We compared gradient calibration results using three different samples in 5 mm NMR tubes: (1) 3.2 cm height $^{2}H_2O$-$^{1}H_2O$ mixture (9:1 mol ratio) doped with 1 wt% $CuSO_4$ that decreased both $^{2}H_2O$ and $^{1}H_2O$ T_1 values below 500 ms and dry glycerol samples with a height of (2) 4.3 cm and (3) 0.5 cm. We performed diffusion

measurements on ^2H_2O-^1H_2O mixture and glycerol at 20 ^oC and pure ^2H_2O at 25^oC, respectively. The glycerol we studied was dry and sealed prior to use. Though it is hygroscopic and its diffusion coefficient varies with water content, in our case water content variation is negligible since our measured diffusion coefficient remained unchanged over the span of the whole experiment. In this paper, we just use glycerol to check the precision rather than the accuracy of our gradient calibration. Diffusion measurements and gradient preemphasis adjustments were conducted on a Bruker Avance III WB 400 MHz (9.4 T) NMR spectrometer, equipped with either a 10 mm ^1H or a 10 mm single resonance ^2H coil in a Diff60 single axis gradient probe with a maximum gradient strength of 30 T/m. The rf coil length is 1.5 cm. The pulsed-gradient stimulated-echo (PGSTE) sequence employed a sinusoidal-shaped gradient pulse and a 90^o radiofrequency (rf) pulse of 10.5μs and 27 μs for the ^1H and ^2H coils, respectively. We used long experiment repetition time (≥ 2 s) to keep the gradient duty cycle low enough (< 0.5 %) so that any residual heat in the gradient coil should have dissipated prior to the next pair of gradient pulses. Also, the temperature monitored in the gradient coil did not change during the entire set of experiments. For diffusion measurements, gradient stabilization time varied between 1.5 and 10 ms, depending on gradient strength and duration. Gradient pulses g varied from 0 to 18 T/m in 16 steps with relaxation delay times > $5T_1$ and an effective pulse duration δ between 1.5 and 3 ms (for sinusoidal-shaped gradient pulses, the real pulse duration = 1.57×effective pulse duration). Diffusion time Δ varied from 10 to 100 ms for ^2H_2O and 10 to 300 ms for glycerol with diffusion coefficients *D* determined based on the Stejskal-Tanner equation:

$$I = I_0 \exp\left(-D\gamma^2 g^2 \delta^2 (\Delta - \frac{\delta}{3})\right) = I_0 \exp(-Db) \qquad (3.1)$$

where *I* is signal intensity, I_0 is signal intensity with g = 0 and $b = \gamma^2 g^2 \delta^2 (\Delta - \frac{\delta}{3})$ is the Stejskal-Tanner factor. Gradient preemphasis adjustments employed δ = 3 ms effective gradient pulses,

followed by observing 10 fids after a variable delay time ranging from 0.4 ms to 50 ms. An adequate relaxation delay (> $5T_1$) is also allowed between each neighboring fid. Here, we used a 30^o rf pulse for preemphasis adjustments to further avoid possible radiation damping effects.[29]

3.3 Result and Discussion

After gradient preemphasis adjustments, we examine the impact of gradient transients on NMR signal by measuring ^2H_2O diffusion in the 3.2 cm height ^2H_2O-^1H_2O mixture. Both effective gradient pulse duration and gradient stabilization time are fixed to 1.5 ms. Figure 3.1a representatively shows a stack of ^2H_2O diffusion spectra with gradient strengths increasing from 6.6 T/m to 9.4 T/m.

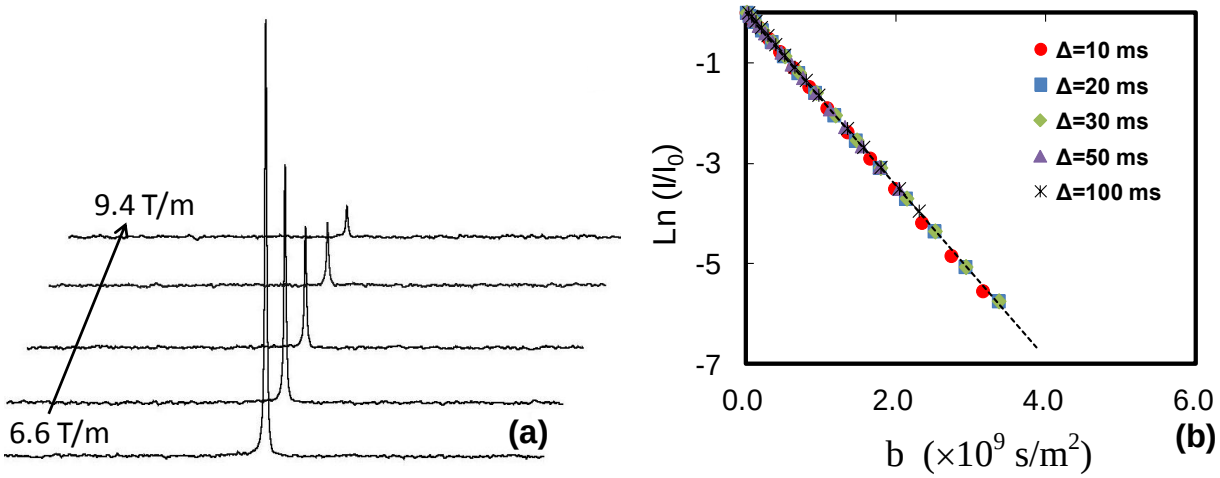

Figure 3.1. ^2H_2O diffusion spectra and signal decay vs. the Stejskal-Tanner parameter

(a) Phase sensitive ^2H_2O diffusion spectra as a function of gradient strength (g) at 20 ^oC, with a diffusion time Δ = 10 ms and an effective gradient pulse δ = 1.5 ms. Sample dimension along the gradient direction is 3.2 cm. No observable phase shift or distortion exists even when gradient strength reaches a maximum of 9.4 T/m. (b) Plot of signal intensity (logarithmic scale) as a function of the Stejskal-Tanner parameter for diffusion experiments with varying diffusion times

Δ. All data points consistently overlap and show linear regression, signifying a well-calibrated gradient with effective suppression of gradient transient effects.

Though the signal intensity at the maximum gradient has decreased by >99% compared with no gradient, the signal-to-noise ratio still remains above 20. There is no observable phase distortion in any of these spectra, which signifies effective suppression of gradient transients. We further measure the diffusion coefficient *D* vs. diffusion time Δ and plot the results using the Stejskal-Tanner equation as shown in figure 3.1b. Linear regression and consistent overlap among different data sets seemingly demonstrate the stability and reproducibility of gradient pulses.

Unexpectedly, we observe significant spectral phase distortion and deviation from linear regression when using the same set of gradient parameters to study the ^{1}H diffusion of dry glycerol. Here, the glycerol sample height is 4.3 cm. Figure 3.2a shows a set of phase-sensitive glycerol spectra with varying gradient strengths.

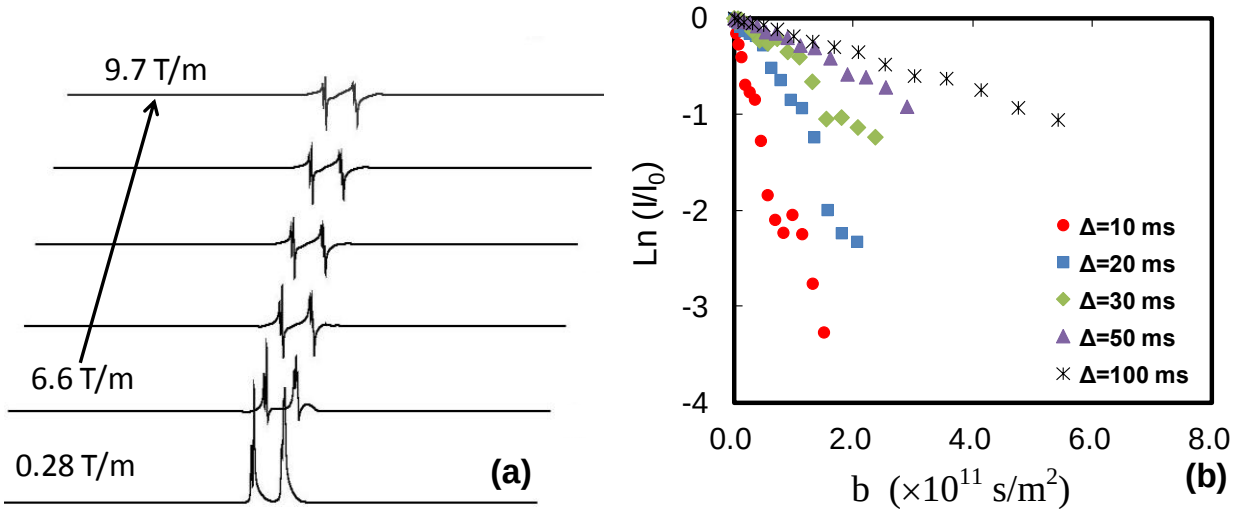

Figure 3.2. (^{1}H) glycerol spectra and signal decay vs. the Stejskal-Tanner parameter

(a) Representative stack of glycerol (^{1}H) diffusion spectra as a function of gradient strength (g) at 20 ^{o}C. The diffusion time is Δ = 20 ms and δ = 1.5 ms. Sample dimension along the gradient

direction is 4.3 cm. The spectra exhibit increasing levels of phase distortion with gradient strength. (b) Plot of signal intensity (logarithmic scale) as a function of the Stejskal-Tanner parameter for diffusion experiments with varying Δ. Diffractive signal decay emerges at short diffusion time even if the diffusion spectra are processed using magnitude mode. However, signal attenuation becomes normal when the diffusion time is above 100 ms.

For comparison, the gradient varies within a similar range as compared to ^2H_2O. In contrast to the ^2H_2O results, phase distortion starts to emerge in glycerol spectra even when the gradient strength is below 5 T/m. In addition, phase distortion increases with gradient strength. To understand the origin of this irregular phase pattern, we process the diffusion spectra in magnitude mode and show the Stejskal-Tanner plot in figure 3.2b, and compare experimental results with varying Δ. The signal decay profile greatly deviates from the expected linear regression and exhibits a diffractive-like phenomenon[21] at short diffusion times. We also notice that the signal decay approaches a linear regression as diffusion time increases to 100 ms and gives a reasonable *D* value of $(1.85 \pm 0.05)\times10^{-12}$ m^2/s at 20°C for dry glycerol. This number continues to decrease down to a plateau value of $(1.20 \pm 0.05)\times10^{-12}$ m^2/s at longer diffusion times (data not shown). In PFG NMR studies, anomalous signal attenuation is usually associated with restricted diffusion in complex structures, which cannot be the case for a pure liquid (if no chemical exchange occurs on the NMR diffusion time scale) such as glycerol. Moreover, sample movement cannot explain the twisted phase patterns that would otherwise be corrected in magnitude mode to yield a normal signal decay curve.[20] Thus, there is a remarkable inconsistency regarding gradient calibration when comparing results obtained from ^2H_2O and (^1H) glycerol. This apparent contradiction challenges the reliability of the standard protocol for high gradient calibration based on low γ nuclei.

To investigate this apparent contradiction, we refer to the pulse sequence for gradient preemphasis adjustments as shown in figure 3.3a. The sequence allows observation of gradient transient effects on NMR signals as it employs a gradient pulse before applying a rf pulse for signal detection. A variable time interval t_d between the gradient and rf pulse allows for examination of gradient transient effects that modulates spectral appearance. This delay time t_d is a surrogate for the gradient delay time (stabilization time) used in the PGSTE sequence as shown in figure 3.3b, which is inserted after each gradient pulse. Since the PGSTE sequence takes the advantage of long T_1 relaxation times to measure diffusion of species with short T_2, it is desired to use a short t_d value to avoid significant transverse relaxation while maintaining effective gradient transient suppression. On the other hand, gradient transient effects are likely to increase with gradient strength and duration, and thus require a longer t_d to avoid interference with the signal. To examine the time dependence of gradient transients, we use a sinusoidal-shaped gradient pulse and vary t_d values from 0.4 ms to 50 ms. We display 10 successive observed FIDs and compare the gradient transient signal interference between ^2H_2O (3.3c) and ^1H_2O (3.3d). In both figure 3.3c and 3.3d, FIDs are displayed for gradient strengths g = 0, 3, 6, 10.5, 15 and 18 T/m from (i) to (vi).

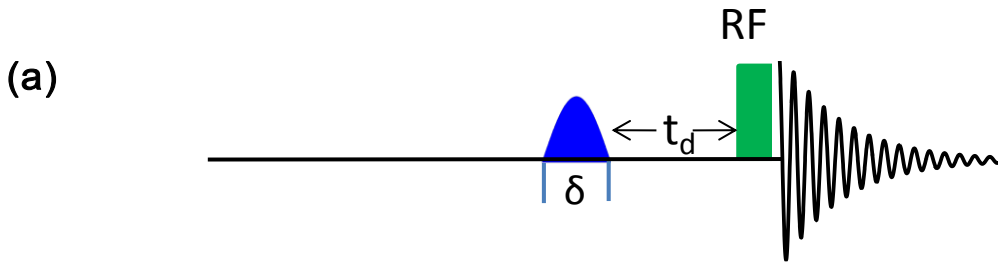

(b)

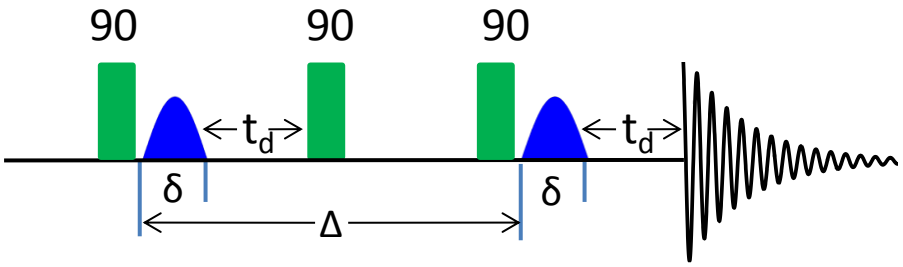

(c) ^2H_2O

(i) g= 0 T/m

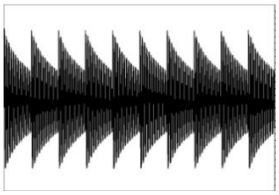

(ii) g= 3 T/m

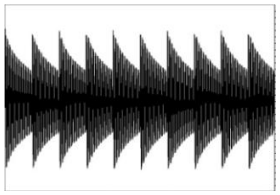

(iii) g= 6 T/m

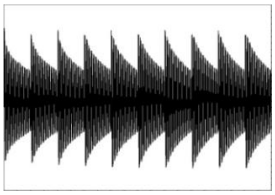

(iv) g= 10.5 T/m

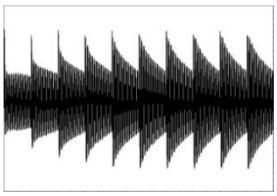

(v) g= 15 T/m

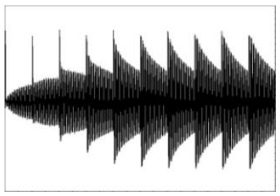

(vi) g= 18 T/m

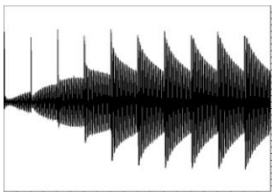

(d) ^1H_2O

(i) g= 0 T/m

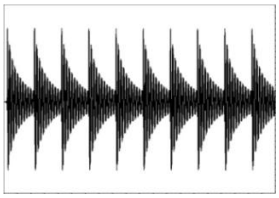

(ii) g= 3 T/m

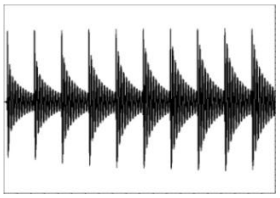

(iii) g= 6 T/m

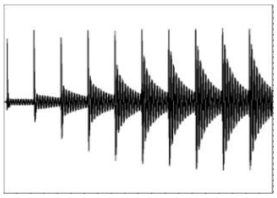

(iv) g= 10.5 T/m

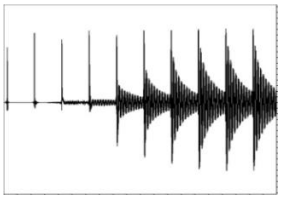

(v) g= 15 T/m

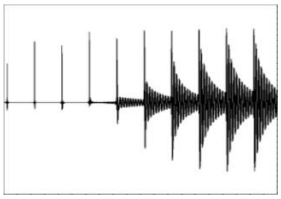

(vi) g= 18 T/m

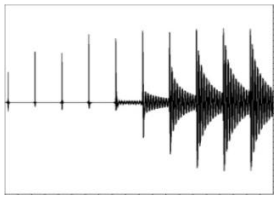

Figure 3.3. Pulse sequences for gradient preemphasis adjustment and results

(a) Pulse sequence for detecting the influence of gradient transients on the FID. (b) A typical PGSTE pulse sequence with a gradient stabilization time t_d inserted after each gradient pulse. In (a), the effective gradient pulse is fixed to 3 ms, and experiments were taken with variable delay times t_d prior to signal acquisition. The same gradient strengths and t_d list are used when comparing results between the (c) ^2H_2O and (d) ^1H_2O samples. The applied gradient strength is 0, 3, 6, 10.5, 15 and 18 T/m, respectively. 10 FIDs are acquired with the set of t_d values: 0.4, 0.6, 0.8, 1, 1.5, 2, 3, 8, 30 and 50 ms. Interference between the FID and gradient transients is much stronger for the ^1H_2O sample, resulting in a marked dependence of FID quality on t_d.

Clearly, the ^2H_2O signal (figure 3.3c) shows different responses to gradient transients as compared to ^1H_2O (figure 3.3d). In the low γ case, a stabilization time of one millisecond seems sufficient to remove the gradient transient effect up to gradient strengths of 10.5 T/m. In the high γ case, the gradient transient effect only becomes negligible when t_d exceeds 8 ms. Moreover, the gradient transient effect for ^1H_2O lasts up to 3 ms even at 6 T/m gradient strength. These results suggest that the gradient preemphasis is adequately adjusted for ^2H_2O but not for ^1H_2O. These results show consistency with the observed contradictions in figure 3.1 and figure 3.2. We also observe that a long gradient delay time (up to 10 ms) partially eliminates anomalies in the diffusion spectra and signal attenuation, but improvement is limited (data not shown). Thus, gradient pulse irreproducibility is also likely present. In addition, the gradient pulse tends to be more reproducible at long diffusion times Δ, as shown in figure 3.2 where signal attenuation becomes normal at large Δ values. It is likely that a long time interval allows complete dissipation of heat generated in the gradient coil by the first gradient pulse that may change the coil resistance and thus influence the generation of the second gradient pulse.[21] All of these

phenomena imply that the negligible dephasing effect induced by gradient transients/gradient pair mismatch when observing with ^2H_2O have been magnified by a factor of $\frac{\gamma_{1_H}}{\gamma_{2_H}} = 6.5$ and become evident when measuring the diffusion of glycerol (^1H). Such a factor also enters as a square into the Stejskal-Tanner term $-D\gamma^2g^2\delta^2\left(\Delta - \frac{\delta}{3}\right)$. However, since $D_{\text{glycerol}} \approx 1000\ D_{2H2O}$, the impact on diffusion curves is less for glycerol than ^2H_2O. Thus, our observed anomalous decay curves mainly relies on the dephasing factor by the gradient transient effect, which is proportional to γ.

Consequently, we arrive at a phenomenological hypothesis: calibrating high gradients using low γ nuclei has a critical drawback due to their low sensitivity to artifacts (gradient transients). In other words, high gradients calibrated using low γ nuclei such as ^2H or ^{15}N are not adequate for studying slow motions of molecules via detection of high γ nuclei such as ^{19}F or ^1H.

Here, we further perform a detailed analysis based on this hypothesis. The gradient transient effect can be alternatively considered as a consequence of gradient pair mismatch. Due to the short stabilization time in the PGSTE sequence, the second rf pulse (after the first gradient pulse) "terminates" gradient transient effects by pulling spin magnetization partially into the longitudinal direction while gradient transients only interfere with the residual transverse magnetization, which is dephased by a small spoil gradient. However, gradient transients created by the second encoding gradient pulse will overlap with signal detection, thus distorting the detected NMR signal. As a result, the signal-gradient transient interferences after the first and second gradient pulses are not symmetric. This asymmetric interference can become severe for high γ nuclei even if the gradient strength is moderate. Additionally, gradient transients after the first gradient pulse may persist long enough to partially interact with the second gradient pulse, which complicates the situation. In summary, any asymmetric interference will lead to phase

distortion and possibly substantial signal reduction. How do we alleviate such distortions? Callaghan analyzed the influence of strong gradient pulse on phase stability and suggested using a read gradient to improve the phase instability induced by high gradient pulses.[20] Price and coworkers further discussed a strategy for diagnosing and alleviating mismatch in gradient pairs.[21] Similar to their analytical protocol, we perform a mathematical analysis of the NMR signal in the presence of asymmetric interference generated by the PGSTE sequence. Under the framework of the small gradient pulse (SGP) approximation, a molecule migrating from z_0 to z_i along the gradient direction is encoded with a phase memory of $\Phi_0 = 2\pi q z_0$ and $\Phi_i = 2\pi q z_i$, respectively, and $q = \frac{\gamma g \delta}{2\pi}$. The asymmetric interference results in extra dephasing ($2\pi q z_{asym}$) after the second gradient pulse, changing Φ_i into $\Phi_e = 2\pi(q + q_{asym})z_i$, with q_{asym} expected to increase with q. Thus, an individual spin moving from z_0 to z_i contributes a spatially dependent phase angle $\Delta\Phi$ to the detected signal:

$$\Delta\Phi = 2\pi(q + q_{asym})z_i - 2\pi q z_0 \qquad (3.2)$$

Defining diffusion displacement as $Z = z_i - z_0$ and integrating equation 3.2 across the entire sample l, the following expression for NMR signal arrives:

$$I = \int_{-\infty}^{+\infty} P(Z)\exp(i2\pi qZ)\,dZ \int_{-\frac{l}{2}}^{\frac{l}{2}} \rho(z_i)\exp\left(i2\pi q_{asym} z_i\right) dz_i \qquad (3.3)$$

Equation 3.3 contains two assumptions: 1) the gradient coil center matches that of the sample; 2) both the gradient and rf coils cover the entire sample. $\rho(z_i) = \frac{1}{l}$ is the spin density along the gradient direction. $P(Z) = \frac{1}{(4\pi D\Delta)^{\frac{1}{2}}}\exp\left(-\frac{(z_i - z_0)^2}{4D\Delta}\right)$ is a Gaussian function that governs the displacement probability. Thus, equation 3.3 simplifies to:

$$I = I_0 \exp(-4\pi^2 q^2 \Delta D)\,\mathrm{Sinc}(\pi q_{asym} l) \qquad (3.4)$$

Signal oscillation with respect to q_{asym} by a sinc function is clearly manifested in equation 3.4. Figure 3.4 illustrates the signal attenuation calculated using the Stejskal-Tanner equation (straight line) and equation 3.4 (blue dots) for both ^2H_2O and glycerol. For simplification, we just made a simple assumption to facilitate the data analysis. We assume q_{asym} is proportional to q and set $q_{asym} = 1 \times 10^{-4}$ q. This is equivalent to 0.01% gradient pair mismatch. The assumption is just a rough approximation, which may not hold exactly for some cases. However, the predicted trend should hold in general and our analysis is also consistent with the assumption, at least for the observed diffractive peaks. Even with this small gradient mismatch, equation 3.4 yields evident diffractive-like signal attenuation for glycerol, in agreement with our observations in figure 3.2. In comparison, the calculated result for ^2H_2O using equation 3.4 shows excellent agreement with the theoretical prediction. Equation 3.4 holds if the isocenters of the sample and the gradient coil match. Otherwise, gradient transient effects, such as eddy current will further lead to phase distortion in the spectra, which may vary with gradient strength. Since our diffusion measurements yield a single component for ^2H_2O, it is not evident that our gradient system suffers from nonlinearity spatially, which will yield multi-component fits. To better illustrate the effect described in equation 3.4, figure 3.5 presents a schematic representation of the effect of a mismatched gradient pair on diffusion measurements. q_{asym} spatially dephases spin magnetization to form a helix with a pitch inversely proportional to γ, and so the spatial periodicity for a ^2H helix is 6.5 longer than that of ^1H ($\frac{\gamma_{1H}}{\gamma_{2H}} = 6.5$). This difference is insignificant when q_{asym} is small because the helix periodicity in both cases is much larger than the sample dimensions. As q_{asym} increases, the ^1H helix approaches the sample dimension, but the corresponding ^2H_2O helix still remains much larger than the sample size. Consequently, the phases of spin magnetization ensembles within the glycerol sample (^1H) cancel each other out for

some specific q_{asym} values and the diffraction phenomenon appears. With respect to ^2H_2O, the phase angle of spin magnetization remains close to unity ($\pi q_{asym} l$ << 1) and no extra attenuation is induced in the signal decay.

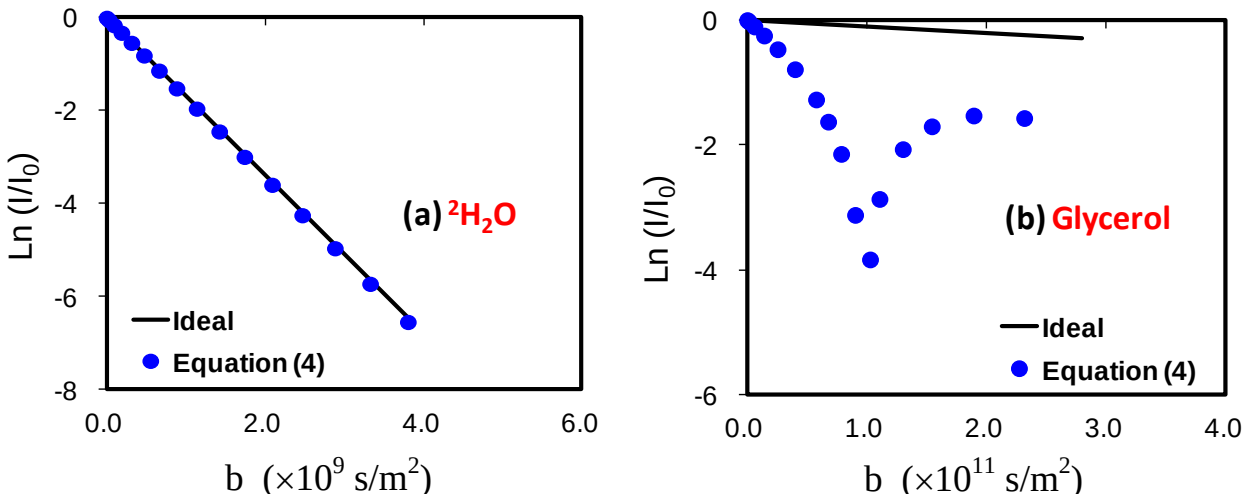

Figure 3.4. Ideal and non-ideal NMR signal decay due to gradient transient effects

Comparison of calculated signal decay curves of (a) ^2H_2O and (b) ^1H glycerol using the Stejskal-Tanner equation (black line) and equation 3.4. Relevant parameters are $q_{asym} = q \times 1 \times 10^{-4}$, l = 2 cm, δ = 1.5ms, Δ =10 ms, $D_{2_{H_2O}} = 1.7 \times 10^{-9}$ m^2/s and $D_{glycerol} = 1.1 \times 10^{-12}$ m^2/s. For ^2H_2O, the calculated signal behavior exhibits good agreement with the theoretical prediction (black line). For glycerol, the calculation drastically deviates from the expected linear regression and even exhibits a diffraction peak at low q values.

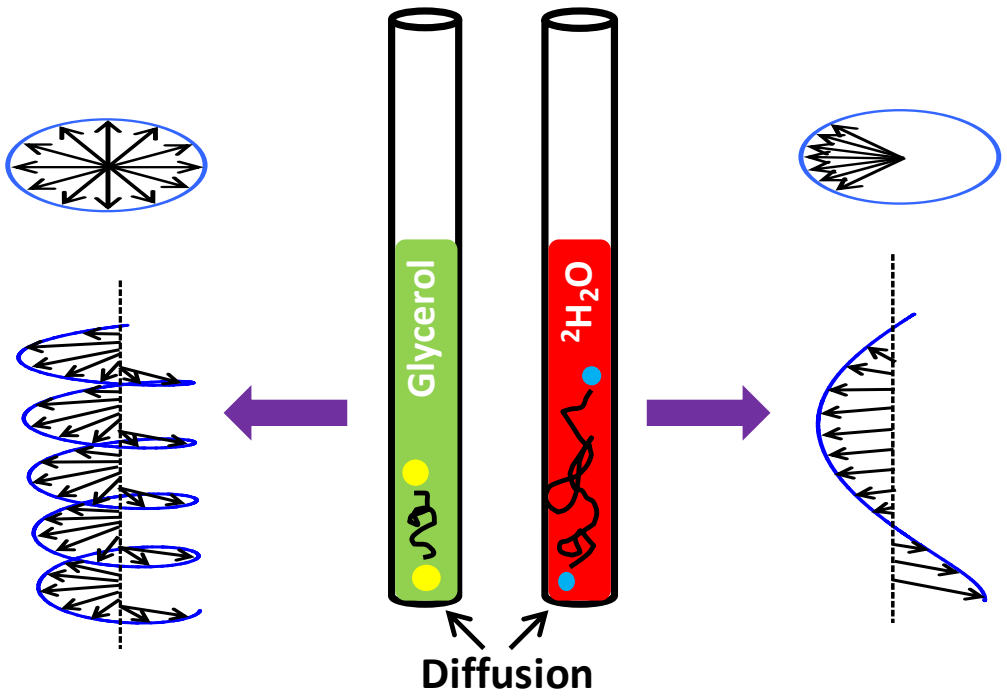

Figure 3.5. A helix by spin magnetization ensembles due to gradient transient effects

Exaggerated representation of spin magnetization sub-ensembles forming a helix due to their interaction with q_{asym}. Due to the difference in γ, the helix periodicity is much shorter for ^1H glycerol than ^2H_2O. For ^1H, the projection of spin magnetization in the transverse plane is averaged to zero as the helix periodicity approaches the sample dimension. Meanwhile, the spin magnetization average for ^2H remains close to unity.

Equation 3.4 also suggests that the competition of signal decay rate between diffusion vs. gradient transients will determine the level of observed artifact. For fast diffusion, NMR signal will attenuate significantly prior to the observation of any artifact. Thus, this implies that artifact may not be ignored for measuring even slower diffusion (D ~10^{-13}-10^{-14} m^2/s) though high gradient is well calibrated using a viscous liquid bearing high γ nuclei, such as glycerol. In other words, gradient transients ($\frac{q_{asym}}{q}$) must be meticulously controlled to allow robust measurements of very slow diffusion coefficient. Based on this viewpoint, we simplify equation 4 into equation

5 (assuming $\pi q_{asym} l$ is not too larger than 1) to estimate the error bar associated with diffusion measurements in the presence of gradient transients:

$$I = I_0 \exp(-4\pi^2 q^2 \Delta D)\, \mathrm{Sinc}\left(\pi q_{asym} l\right)$$

$$= I_0 \exp(-4\pi^2 q^2 \Delta D)\left(1 - \frac{(\pi q_{asym} l)^2}{3!}\right)$$

$$= I_0 \exp(-4\pi^2 q^2 \Delta D) \exp\left(-\frac{(\pi q_{asym} l)^2}{3!}\right)$$

$$= I_0 \exp\left[-4\pi^2 q^2 \Delta \left(D + \frac{(\alpha l)^2}{24\,\Delta}\right)\right] \qquad (3.5)$$

Here we define $\alpha = \frac{q_{asym}}{q}$, which characterizes the level of gradient transients. The measured apparent diffusion coefficient is $D + \frac{(\alpha l)^2}{24\Delta}$, thereby yielding an experimental error bar $\varepsilon = \frac{(\alpha l)^2}{24 D \Delta}$. This result indicates that ε will likely increase by an order of magnitude if D decreases by the same amount. However, such an increment of inaccuracy can be effectively removed by reducing the sample dimension l, which appears as a square term in the expression of ε. For example, assuming one performs high gradient calibration using dry glycerol, which diffuses at the rate of $D \sim 10^{-12}$ m^2/s at room temperature. One can still measure D on the order of 10^{-13} m^2/s with the same level of accuracy if reducing l by a factor of three.

The above analysis is also consistent with equation 3.4, where both q_{asym} and l contribute equally to the signal modulation. To investigate this concept further, we use a glycerol sample of 0.5 cm in length and attempt to match its center with the rf and gradient coils. Figure 3.6a shows a series of phase sensitive ^{1}H spectra (PGSTE slices) as g increases from 6.7 to 10 T/m. As expected, we observe greatly reduced gradient-dependent phase distortion in all these spectra, in contrast to the results shown in figure 3.2a. It is also possible that the center mismatch between the sample and rf coil partially contributes to the phase distortion. We then remove the phase distortion by processing the spectra in magnitude mode and show the Stejskal-Tanner plot

in figure 3.6b. The diffraction pattern disappears and linear regression is observed. In addition, the signal attenuation shows a significantly reduced dependence on diffusion time, as compared with figure 3.2b. All these results match our prediction that apparently matched gradient pairs or suppressed gradient transients may turn into a serious problem as γ and sample dimension increase.

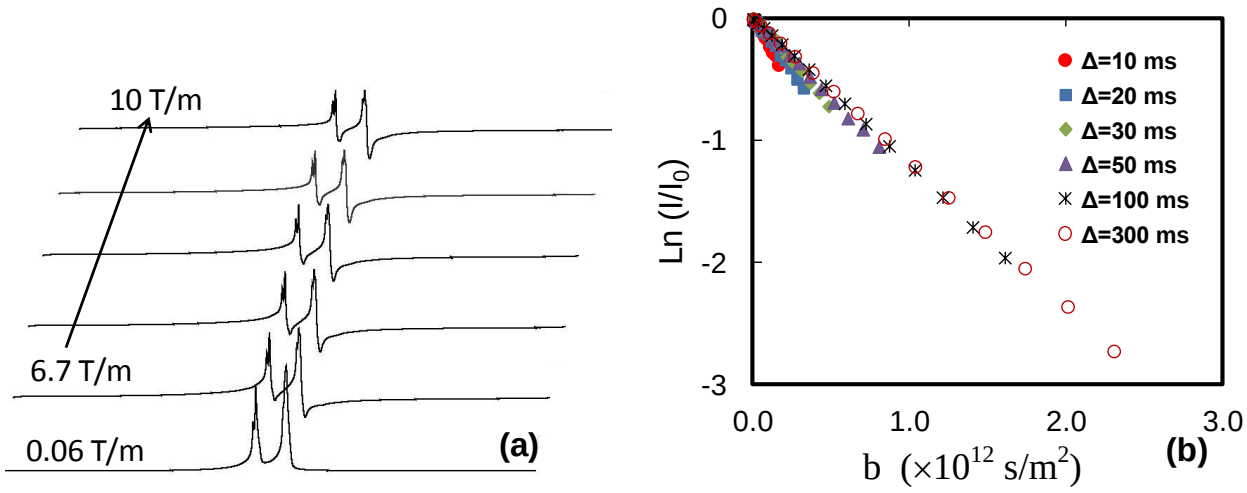

Figure 3.6. (^{1}H) glycerol spectra with less phase distortion and gradient dependence

(a) Stacked spectra showing ^{1}H signal attenuation for dry glycerol diffusion measurements as a function of gradient strength g at 20 ^{o}C. Experimental parameters are identical to that of figure 3.2 but the sample dimension is reduced to 0.5 cm. In comparison to figure 3.2, one obtains significantly improved phase distortion, which also shows a greatly reduced dependence on gradient strength. (b) Logarithmic plot of signal attenuation vs. the Stejskal-Tanner parameter with diffusion spectra processed in magnitude mode. The attenuation curves yield linear regression, in contrast to the diffraction patterns shown in figure 3.2, however there is still some Δ dependence.

We then use the same 3.2 cm height $^{2}H_2O$-$^{1}H_2O$ mixture to perform fine adjustments of the gradient preemphasis by examing the $^{1}H_2O$ signal and show relevant results in figure 3.7a and 3.7b. Experimental parameters remain identical to those used in figure 3.3. The gradient preemphasis is now almost perfect for $^{2}H_2O$ regardless of gradient strength, as the gradient transient effect becomes negligible after 0.6 ms delay time. We also observe similar results for $^{1}H_2O$ where 1 ms and 3 ms stabilization times are sufficient for the gradient transient decay under 10.5 T/m and 18 T/m gradient strengths, respectively. As mentioned earlier, a well adjusted gradient preemphasis is not sufficient to assure the absence of all the transient effects and we also remeasure glycerol diffusion to guarantee that these transient effects are negligible. Figure 3.8a shows a representative stack of ^{1}H diffusion spectra for glycerol obtained using the new gradient preemphasis settings. The spectra exhibit no phase distortion as gradient increases up to 13 T/m. As we expect, slight phase distortion still arises in the spectra as the gradient pulse becomes stronger. Despite these visible net phase shifts, the Stejskal-Tanner plot in figure 3.8b yields linear regression with no dependence on gradient strengths and diffusion times. This suggests that these small phase disturbances have negligible impact on the diffusion measurement. We also cross check the reliability of our current gradient calibration using other types of liquids, such as viscous ionic liquids and concentrated polystyrene solution with a low polydispersity index (data not shown). We consistently obtain D values independent of Δ for different ionic liquids, ranging from $D = (6.70 \pm 0.1)\times10^{-12}$ m^2/s to $(1.36 \pm 0.05)\times10^{-11}$ m^2/s, depending on the ionic liquid type. The concentrated polystyrene solution easily allows determination of the level of phase distortion since the NMR signal only decays by 8% at g=18 T/m. Again, no significant phase distortion appears in the spectrum, consistent with the glycerol diffusion results. However, we measure $D \sim 10^{-14}$ m^2/s, which could show a Δ dependence since

the diffusion length ($r_{rms} = (2D\Delta)^{1/2}$ ~10 nm) is close to the polymer chain dimension. We again confirm that the new gradient preemphasis can generate reproducible gradient pulses up to 18 T/m with an effective duration of 3 ms and decay of 1.5-3 ms. By following such a procedure to adjust gradient preemphasis and calibrate gradients using high gamma nuclei, one can monitor and minimize the gradient transient effect, which may not be evident when observing low gamma nuclei. This protocol provides a solid basis for diffusion studies, the results of which are reliable when switching to other low gamma samples. In comparison, if the high gradient is calibrated using low gamma nuclei, the accuracy of measured diffusion data can vary drastically, depending on the nature of studied nuclei and the strength of gradient applied.

(a)

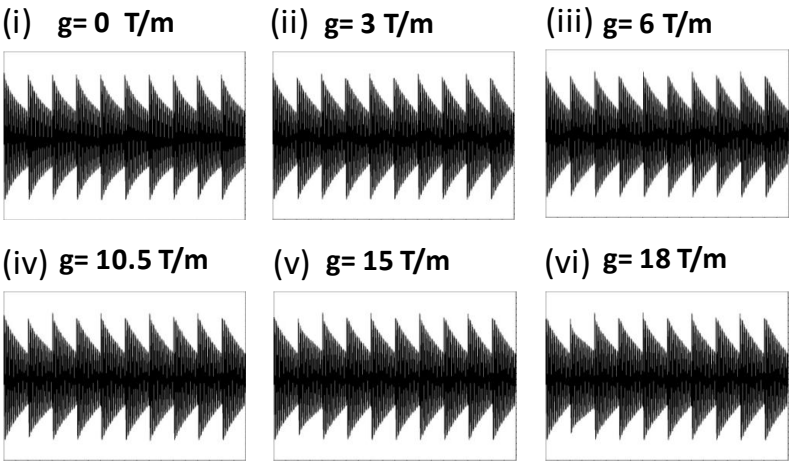

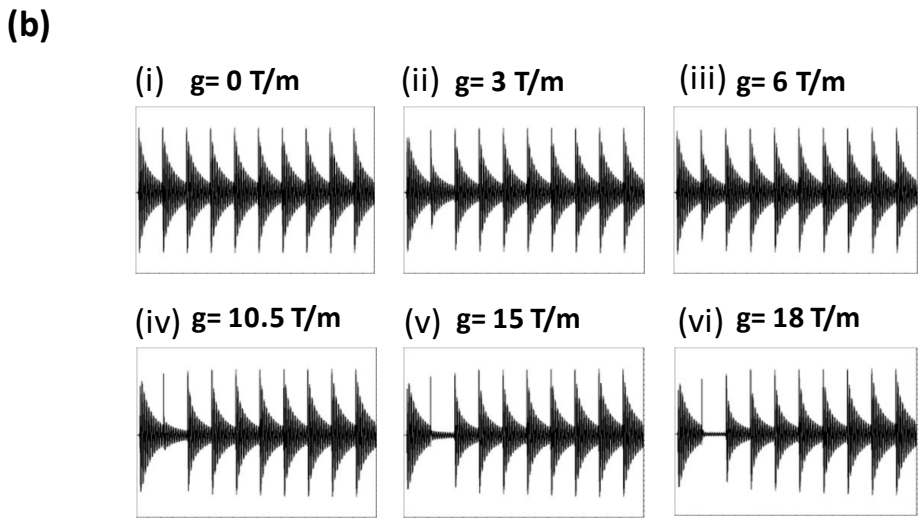

Figure 3.7. Improved gradient system after gradient preemphasis adjustment

Illustration of interference between gradient transients and FIDs for a) $^{2}H_2O$ and b) $^{1}H_2O$ samples after further preemphasis adjustment on a $^{1}H_2O$ sample. All experimental parameters and sample dimensions are identical to those shown in figure 3.3. For $^{2}H_2O$, a delay time of 0.8 ms appears sufficient to suppress the gradient transient effect even at gradient strengths of 18 T/m. For $^{1}H_2O$, a delay time of 3 ms is required for the 18 T/m gradient strength to minimize gradient transient effects prior to signal detection.

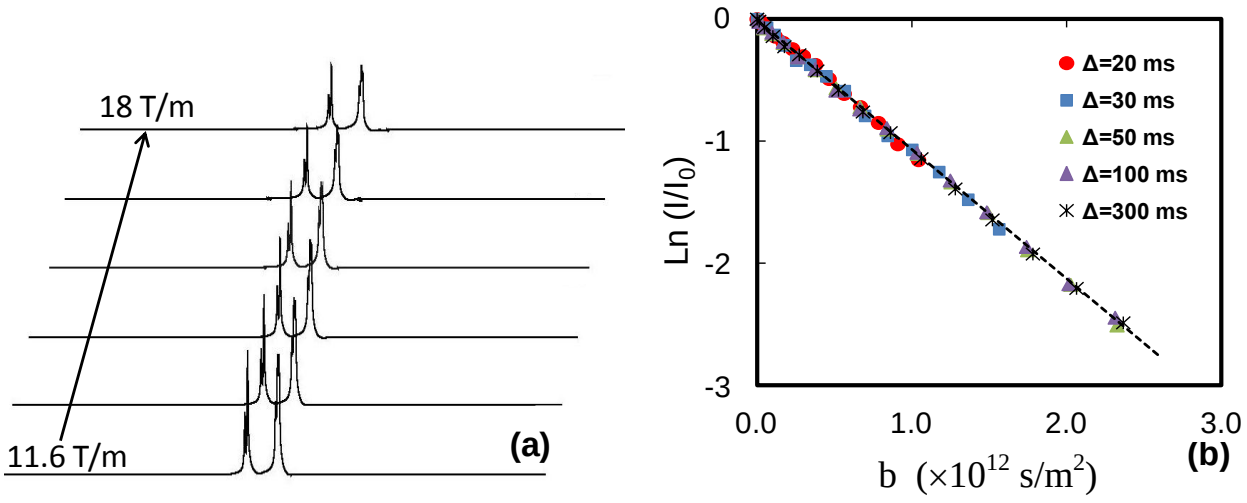

Figure 3.8. (^{1}H) glycerol spectra with no phase distortion and gradient dependence

(a) Representation of ^{1}H diffusion spectra for dry glycerol as a function of gradient strength g following further preemphasis adjustment on a ^1H_2O sample. All experimental parameters are identical to those used in figure 3.2. In contrast to both figure 3.2 and figure 3.5, the diffusion spectra exhibit no phase distortion with $g \leq 13$ T/m. Minor phase distortion exists above 14 T/m, which slightly increases with gradient strength. (b) Logarithmic plot of signal attenuation vs. the Stejskal-Tanner parameter. Diffusion spectra are processed in magnitude mode and all attenuation curves consistently overlap and yield linear regression ($D_{glycerol} = (1.10 \pm 0.05) \times 10^{-12}$ m^2/s) .

Finally, we calibrate gradient strength using pure ^2H_2O to agree with $D = 1.87 \times 10^{-9}$ m^2/s at 25^{o}C. We then utilize the 4.3 cm height glycerol sample to determine the effective range of the gradient coil by intentionally mismatching the gradient pair. Figure 3.9 represents a series of diffractive signal attenuations associated with different levels of gradient pair mismatch. In agreement with our simulations based on equation 3.4, variations in gradient pair mismatch produce well defined and periodic diffraction peaks which consistently yield a shortened sample dimension of 1.5 cm, corresponding to the effective range of the gradient coil. We further examine some diffusion data published in the literature.[15] Ohkubo et al. utilized ^2H_2O for high gradient calibration and observed restricted water diffusion (^1H_2O) using oscillating gradient spin echo (OGSE). They concluded the presence of micron-scale structrual characteristic inside the perfluorosulfonate ionomer. In comparison, we repeated some of their measurements without observing any restricted water diffusion in the same material (see SI). It is very likely they observed experimental artifact and misinterpretated the result as anomalous diffusion due to their

inappropriate gradient calibration by ^2H_2O. The low level of NMR signal attenuation (by 20% at maximum) further limited their observation of any artifact.

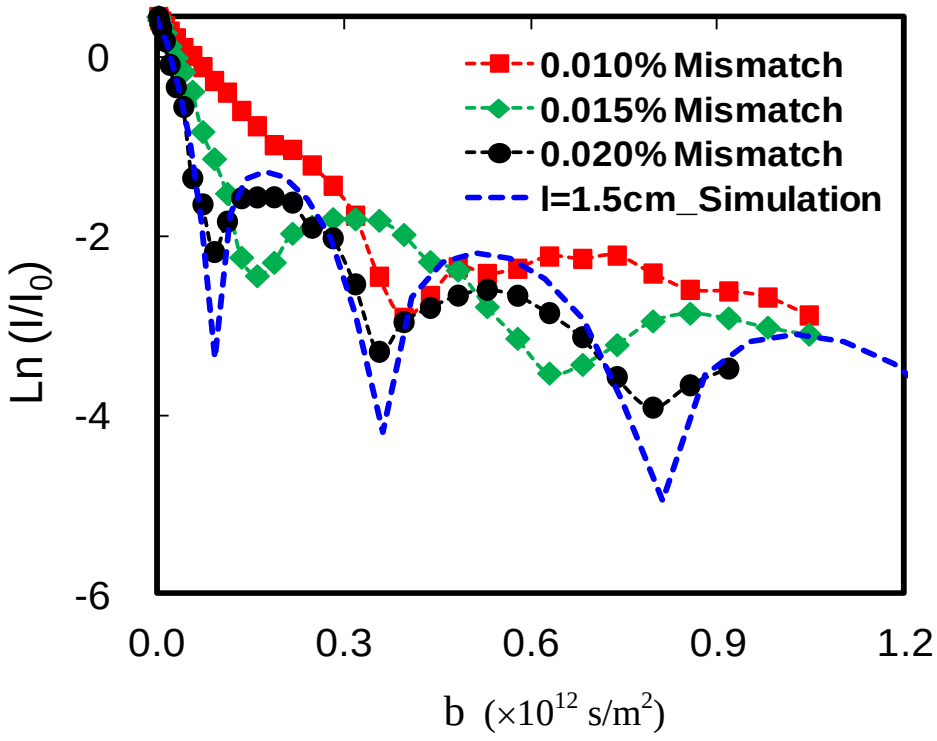

Figure 3.9. Estimation of the effect size of the gradient coil

Simulation and diffractive signal attenuation results on glycerol using an intentionally mismatched gradient pair. Simulation shown for 0.020% mismatch only, for clarity. The sample height is 4.3 cm. The gradient strength varies from 0 to 18 T/m, δ = 1.5 ms, and Δ =20 ms. Diffractive peaks for all mismatch conditions yield an apparent sample dimension of 1.5 cm, which corresponds to the effective range of the gradient coil.

3.4 Conclusion

We have examined the role of gyromagnetic ratio (γ) and sample dimension in the process of calibrating high magnetic field gradients. We observed no anomalies in ^2H_2O diffusion spectra

but significant phase distortion and diffractive signal attenuation when measuring ^{1}H glycerol diffusion. In addition, we observed dramatically enhanced interference between gradient transients and FIDs in $^{1}H_2O$, as compared to $^{2}H_2O$. We further mathematically analyzed the disturbed NMR signal by gradient transients and gradient pair mismatch to understand how γ and sample dimension impact diffusion measurements. Our analysis indicates that reducing sample length along the gradient direction can screen off the gradient transient effect and gradient pair mismatch, similar to changes in γ. Our subsequent diffusion measurements using a short glycerol sample significantly reduce phase distortion and anomalous signal attenuation, as predicted.

The combination of experimental observations and mathematical calculations show that low γ nuclei do not represent adequate candidates for general high gradient calibration due to their poor sensitivity to artifacts such as gradient transients and gradient pair mismatch. Thus, high gradients calibrated using low γ nuclei only should not be directly extended to determine slow diffusion coefficients with high γ nuclei. We further performed fine gradient preemphasis adjustments using $^{1}H_2O$ and achieved drastic improvement in matching the gradient pairs and suppressing gradient transients. The new gradient preemphasis settings allow the application of 3 ms gradient pulses with strengths up to 1800 G/cm without introducing significant errors (< 3 %) into the diffusion measurement. Using our newly calibrated gradient system, we intentionally slightly mismatched the gradient pair to measure the effective range of the gradient coil, which gave a value of 1.5 cm. Clearly, without these higher level calibrations, many observed slow diffusion coefficients and diffractive or restricted diffusion phenomena must be viewed with caution. This paper lays out strategies for effectively eliminating artifacts in diffusion measurements on slow moving species.

References

[1] W.S. Price, Pulsed-field gradient nuclear magnetic resonance as a tool for studying translational diffusion .1. Basic theory, Concepts Magn. Reson. 9 (1997) 299-336.
[2] E.O. Stejskal, J.E. Tanner, Spin diffusion measurements: Spin echoes in the presence of a time-dependent field gradient, J. Chem. Phys. 42 (1965) 288-292.
[3] L.L. Latour, K. Svoboda, P.P. Mitra, C.H. Sotak, Time-dependent diffusion of water in a biological model system, P. Natl. Acad. Sci. USA 91 (1994) 1229-1233.
[4] P.W. Kuchel, A. Coy, P. Stilbs, NMR "diffusion-diffraction" of water revealing alignment of erythrocytes in a magnetic field and their dimensions and membrane transport characteristics, Magn. Reson. Med. 37 (1997) 637-643.
[5] D.S. Tuch, T.G. Reese, M.R. Wiegell, N. Makris, J.W. Belliveau, V.J. Wedeen, High angular resolution diffusion imaging reveals intravoxel white matter fiber heterogeneity, Magn. Reson. Med. 48 (2002) 577-582.
[6] J. Li, K.G. Wilmsmeyer, L.A. Madsen, Anisotropic diffusion and morphology in perfluorosulfonate ionomers investigated by NMR, Macromolecules 42 (2009) 255-262.
[7] J.B. Hou, Z.Y. Zhang, L.A. Madsen, Cation/anion associations in ionic liquids modulated by hydration and ionic medium, J. Phys. Chem. B 115 (2011) 4576-4582.
[8] J. Li, J.K. Park, R.B. Moore, L.A. Madsen, Linear coupling of alignment with transport in a polymer electrolyte membrane, Nature Mater. 10 (2011) 507-511.
[9] R.W. Mair, M.N. Sen, M.D. Hurlimann, S. Patz, D.G. Cory, R.L. Walsworth, The narrow pulse approximation and long length scale determination in xenon gas diffusion NMR studies of model porous media, J. Magn. Reson. 156 (2002) 202-212.
[10] P. Kortunov, S. Vasenkov, J. Karger, R. Valiullin, P. Gottschalk, M.F. Elia, M. Perez, M. Stocker, B. Drescher, G. McElhiney, C. Berger, R. Glaser, J. Weitkamp, The role of mesopores in intracrystalline transport in usy zeolite: PFG NMR diffusion study on various length scales, J. Am. Chem. Soc. 127 (2005) 13055-13059.
[11] G. Fleischer, F. Fujara, Segmental diffusion in polymer melts and solutions of poly(ethylene oxide) measured with gield gradient NMR in high-field gradients, Macromolecules 25 (1992) 4210-4212.
[12] G. Annat, D.R. MacFarlane, M. Forsyth, Transport properties in ionic liquids and ionic liquid mixtures: The challenges of NMR pulsed field gradient diffusion measurements, J. Phys. Chem. B 111 (2007) 9018-9024.
[13] M. Cifelli, V. Domenici, S.V. Dvinskikh, M. Glogarova, C.A. Veracini, Translational self-diffusion in the synclinic to anticlinic phases of a ferroelectric liquid crystal, Soft Matter 6 (2010) 5999-6003.
[14] K. Hayamizu, Y. Aihara, W.S. Price, Correlating the NMR self-diffusion and relaxation measurements with ionic conductivity in polymer electrolytes composed of cross-linked poly(ethylene oxide-propylene oxide) doped with $LiN(SO_2CF_3)_2$, J. Chem. Phys. 113 (2000) 4785-4793.
[15] T. Ohkubo, K. Kidena, A. Ohira, Determination of a micron-scale restricted structure in a perfluorinated membrane from time-dependent self-diffusion measurements, Macromolecules 41 (2008) 8688-8693.
[16] K. Hayamizu, E. Akiba, T. Bando, Y. Aihara, W.S. Price, NMR studies on poly(ethylene oxide)-based polymer electrolytes with different cross-linking doped with $LiN(SO_2CF_3)_2$.

Restricted diffusion of the polymer and lithium ion and time-dependent diffusion of the anion, Macromolecules, 36 (2003) 2785-2792.
[17] N.N. Yadav, W.S. Price, Impediments to the accurate structural characterisation of a highly concentrated emulsion studied using NMR diffusion diffraction, J. Colloid Interface Sci. 338 (2009) 163-168.
[18] P.T. Callaghan, A. Coy, D. Macgowan, K.J. Packer, F.O. Zelaya, Diffraction-like effects in NMR diffusion studies of fluids in porous solids, Nature, 351 (1991) 467-469.
[19] W.S. Price, Pulsed-field gradient nuclear magnetic resonance as a tool for studying translational diffusion: Part II. Experimental aspects, Concepts Magn. Reson. 10 (1998) 197-237.
[20] P.T. Callaghan, PGSE MASSEY, a sequence for overcoming phase instability in very-high-gradient spin-echo NMR, J. Magn. Reson. 88 (1990) 493-500.
[21] W.S. Price, K. Hayamizu, H. Ide, Y. Arata, Strategies for diagnosing and alleviating artifactual attenuation associated with large gradient pulses in PGSE NMR diffusion measurements, J. Magn. Reson. 139 (1999) 205-212.
[22] J.S. Murday, Measurement of magnetic field gradient by its effect on the NMR free induction decay, J. Magn. Reson. 10 (1973) 111-120.
[23] M.I. Hrovat, C.G. Wade, NMR pulsed-gradient diffusion measurements .1. Spin-echo stability and gradient calibration, J. Magn. Reson. 44 (1981) 62-75.
[24] T.R. Saarinen, C.S. Johnson, Imaging of transient magnetization gratings in NMR - analogies with laser-induced gratings and applications to diffusion and flow, J. Magn. Reson. 78 (1988) 257-270.
[25] M. Holz, H. Weingartner, Calibration in accurate spin-echo self-diffusion measurements using ^{1}H and less-common nuclei, J. Magn. Reson. 92 (1991) 115-125.
[26] A.C. Wright, H. Bataille, H.H. Ong, S.L. Wehrli, H.K. Song, F.W. Wehrli, Construction and calibration of a 50 T/m z-gradient coil for quantitative diffusion microimaging, J. Magn. Reson. 186 (2007) 17-25.
[27] B. Antalek, Using pulsed gradient spin echo NMR for chemical mixture analysis: How to obtain optimum results, Concepts Magn. Reson. 14 (2002) 225-258.
[28] N.N. Yadav, A.M. Torres, W.S. Price, An improved approach to calibrating high magnetic field gradients for pulsed field gradient experiments, J. Magn. Reson. 194 (2008) 25-28.
[29] J.H. Chen, B. Cutting, G. Bodenhausen, Measurement of radiation damping rate constants in nuclear magnetic resonance by inversion recovery and automated compensation of selective pulses, J. Chem. Phys. 112 (2000) 6511-6514

Chapter 4

Anisotropy and Transport in Poly(arylene ether sulfone) Hydrophilic-Hydrophobic Block Copolymers

Reprinted with permission from Jianbo Hou, Jing Li and Louis A. Madsen, Macromolecules, **2010**,43, 347-353 © 2009, American Chemical Society.

Abstract

Designing tailored block copolymers represents a viable strategy for building polymer membranes with fruitful combinations of properties, such as the high ionic or small molecule conductivity and high mechanical strength needed for applications such as fuel cells and reverse-osmosis water purification. Here we present a systematic study of water transport and morphological alignment in a class of poly(arylene ether sulfone) hydrophilic-hydrophobic multi-block copolymer membranes and compare these with Nafion 212. Multi-axis pulsed-field-gradient NMR yields *diffusion anisotropy*, the ratio of diffusion coefficients measured both in plane ($\boldsymbol{D}_{//}$) and through plane ($\boldsymbol{D}_{\perp}$), as a function of water uptake and block lengths. As block mass increases, diffusion anisotropy exhibits an increasing dependence on water uptake, in contrast to Nafion 212, where diffusion is isotropic and displays no dependence on water uptake. ^{2}H NMR spectroscopy on absorbed D_2O further probes membrane alignment modes. Both types of measurements corroborate uniformly ordered planar structures oriented through the membrane plane in accordance with a lamellar morphology previously observed locally with microscopy. The combination of these two measurements also provides insights into average defect distributions.

4.1 Introduction

Ionomer membranes find wide applications in fuel cells, and reverse-osmosis water purification.[1,2] Many successful membrane materials consist of hydrophilic and hydrophobic polymer moieties, which phase separate into nanoscale water channels to facilitate the transport of mobile species, such as water molecules and protons. Structural characteristics like orientational ordering and multi-scale hierarchical morphologies strongly affect the macroscopic properties and performance of these materials, such as proton conductivity and water transport.[3,4] The current benchmark material for proton exchange membranes (PEM) is Nafion©, a commercially available perfluorosulfonate ionomer that has been studied extensively with respect to morphology, water transport, and proton conductivity.[5-10] Such materials exhibit high proton conductivity when absorbing an adequate amount of water. However, their performance in terms of thermal stability, mechanical strength, and proton conductivity decays drastically at elevated temperature, which limits their applications.[11,12] A current goal in fuel cell membrane design is to develop materials that can work efficiently at higher temperature (>120^{o}C) and low relative humidity.

Consequently, a class of aromatic-based block copolymers consisting of sharply separated hydrophilic and hydrophobic nanophase-separated morphologies are under development.[12-15] These block copolymers are potential candidates to work at low humidity due to their high water absorption. In addition, these materials show excellent thermal and chemical stabilities,[12] which enable them to work at elevated temperature without degradation in performance. Finally, due to the high cost of perfluorinated membranes (~ $2500/kg), these aromatic hydrocarbon materials promise substantially reduced cost in potential wide applications such as fuel cells and other separations applications. Figure 4.1 shows the structures of Nafion

and the BPSH-BPS polymers studied here,[16] where "BP" and "S" correspond to biphenol and sulfonated, respectively. While microscopy is useful for probing local environments, NMR can provide bulk average morphology, as well as convenient and reliable molecular (or ion) transport information. Here, we describe NMR measurements probing anisotropy over a range of block lengths and water uptakes in these solution-cast BPSH-BPS multi-block systems and compare them to the benchmark dispersion-cast polymer Nafion 212.

A.

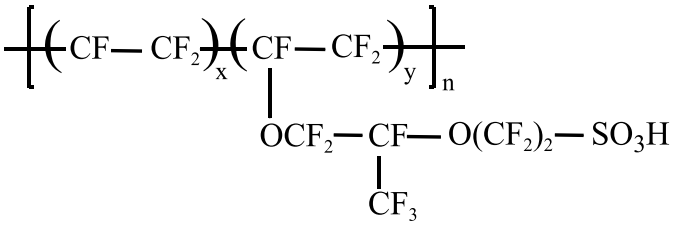

B.

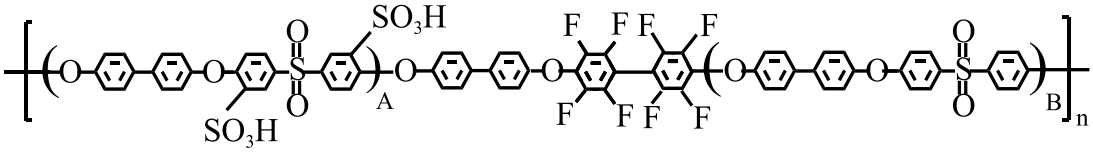

Figure 4.1. Chemical structure of Nafion and BPSH-BPS multi-block copolymers

For Nafion (A), (x:y) represents the ratio of hydrophobic to hydrophilic part. For the block copolymers (B), where A and B represent the hydrophilic and hydrophobic block masses, respectively.

We aim to explore relationships between properties and structures of these materials via diffusion studies using pulsed-field gradient (PFG) NMR diffusometry[17,18] and ^{2}H NMR spectroscopy.[19] Diffusometry is an effective, convenient and repeatable method that can provide quantitative data on how mobile species diffuse,[20,21] including in ionomer membranes.[3,22-24] Rollet *et al.* investigated the transport of different ions in sulfonated polyimide ionomers by PFG NMR and radiotracers techniques.[25] They found dramatic diffusion anisotropy of ions in plane vs

through plane, where ion diffusion in the former direction was much faster than the latter. Kidena *et al.* studied proton (water) diffusion anisotropy in Nafion at different temperatures via PFG NMR.[26] According to their measurement results, diffusion anisotropy was observable at low temperature (~0^{o}C) but was approximately isotropic above room temperature. We recently reported NMR studies of anisotropic structures in several types of Nafion processed under different conditions, based on which we proposed morphological symmetry models.[3]

Our group is among the first to perform correlated studies of local self diffusion and anisotropy in nanophase-separated polymers in order to understand the fundamental relationship between morphological alignment and transport in these materials. For these NMR experiments (diffusometry and spectroscopy), water molecules act as mobile probes interacting with the hydrophilic channels in the ionomers. Thus, the diffusion and partial alignment behavior can be considered as a reflection of the intrinsic characteristics of the materials. In this paper, we report the systematic studies of water diffusion and anisotropy for a series of aromatic hydrocarbon multi-block copolymers, both of which varied substantially over a range of water uptakes. We observe uptake-dependent and block-length-dependent diffusion anisotropy for these copolymers. ^{2}H NMR spectroscopy on these materials, which measures partial ordering of absorbed D_2O molecules through their quadrupole splittings, reflects the alignment of the polymer matrix as well as changes in hydrophilic channel dimensions. This distinct alignment information, on a different length scale than diffusion measurements, correlates with diffusion anisotropy. These two techniques combined provide insight into average defect and domain structures in these materials, specifically from the standpoint of water transport.

4.2 Experimental

4.2.1 Membrane Preparation and Properties

Nafion NRE212 (dispersion cast) membrane with equivalent weight of 1100 (grams of dry membrane per mole of sulfonate groups), and thickness of 50 μm was purchased from E.I. Dupont in the acid form. The multi-block copolymers named as BPSH-BPS (A: B) were obtained from Prof. James E. McGrath's group and the synthetic procedures have been reported elsewhere.[2] The chemical structures are shown in Figure 4.1. Similar to Nafion, these multi-block copolymers contain two parts, with A and B representing the block masses of hydrophilic and hydrophobic parts individually, and are coupled with the linkage group of decafluorobiphenyl (DFBP). For the materials presented in this work, the block masses range from 3 to 15 kg/mol, and in all cases A = B. As reported elsewhere,[13] all these block copolymers were redissolved in N-methyl-2-pyrrolidinone (NMP, Fisher), followed by solution casting onto a clean glass substrate. The prepared films were then cast under an infrared lamp with temperature controlled between 45^{o}C~55^{o}C for 2 days. Membranes were further dried in a vacuum oven at 110 ^{o}C for a whole day to remove the residual solvent. For acidification, the membranes were boiled in 0.5 M sulfuric acid for 2h, then rinsed and boiled in deionized water. Dry membrane thicknesses were 30-40 μm. Depending on membrane type and uptake, this value increased to 60-100 μm upon water swelling.

Table 4.1. Sample information of block copolymers

Sample ID	**Block mass**	**Water uptake**	T_1 **range (ms)**	T_2 **range (ms)**
BPSH-BPS(3k-3k)	3 kg/mol	11% – 24%	~ 9 – 12	~ 2.5 – 3.2
BPSH-BPS(5k-5k)	5 kg/mol	16% – 31%	~ 9 – 12	~ 2.9 – 3.5

BPSH-BPS(10k-10k)	10 kg/mol	16% – 62%	~ 6 – 20	~ 1.5 – 4.9
BPSH-BPS(15k-15k)	15 kg/mol	15% – 41%	~ 7 – 17	~ 2.0 – 4.7
Nafion 212	EW = 1.1kg/mol	9% – 22%	~24 – 50	~ 7.0 – 16

4.2.2 Water Uptake Control

A key issue in diffusion measurements is the water content in the membrane. Making measurements relevant to relative humidity is often set up as a standard parameter for operating fuel cells since it is easy to control. However, a drawback lies in the fact that the actual amount of water in the membrane may fluctuate during cell operation, and this water uptake directly determines membrane transport properties. To solve this problem, we developed several specially designed Teflon cells. Membranes were cut into pieces of 5.5 mm x 5 mm in size, stacked together to a total mass of ~ 40 mg, and trimmed to match the rectangular shaped cavity in the cell, as shown in Figure 4.2. Thus, dead volume is only ~ 20 % of membrane stack volume. A piston cap seals the cell in order to control the water uptake. An 8 mm NMR tube connects to the piston cap with Teflon tape wrapped around at the junction of the two, so as to rigidly fix the sample cell in the bore of the NMR probe. In this way, we locate the samples at the center of the NMR detection coil. Stacks of membranes were not dried in an oven but in a desiccator overnight at room temperature (~ 25 ^{o}C) to avoid any possible heating history effect. Later, membranes were soaked in H_2O for at least 24 h. The wet membranes were blotted to remove free surface water and transferred to the sealed Teflon cell to equilibrate for a period of 8 ~12 hours. All the diffusion measurements were performed at 25^{o}C after sample equilibration. Masses of wet membranes were determined gravimetrically after the NMR experiment. Water uptake is calculated using equation 4.1:

$$Water\ uptake = \frac{Mass_{wet} - Mass_{dry}}{Mass_{dry}} \times 100\% \qquad (4.1)$$

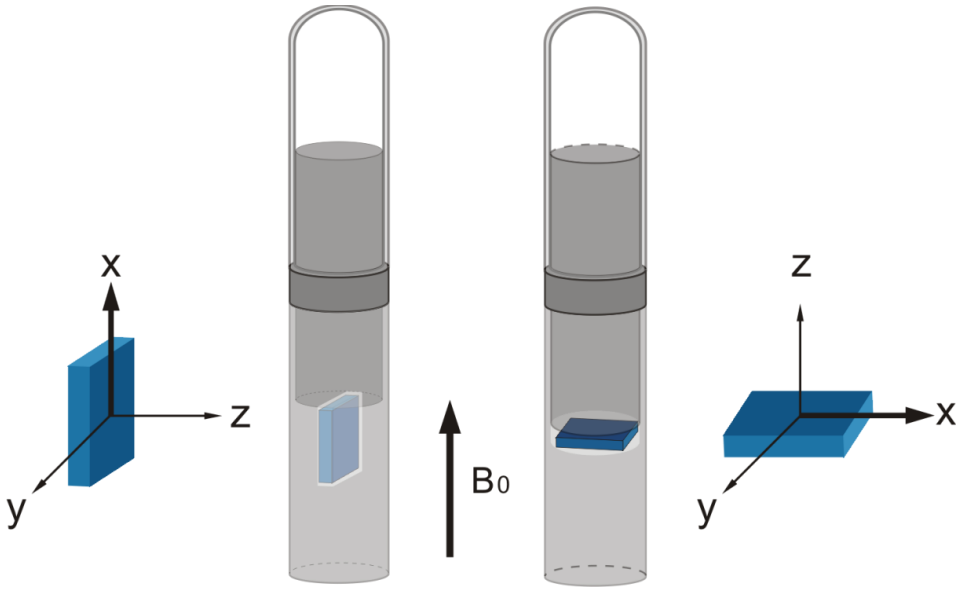

Figure 4.2. Sealed Teflon cells with different configurations

Membrane pieces are stacked in the same orientation to snugly fit the rectangular shaped cavity in the cell. A piston cap is used to seal the cell in which membranes are equilibrated. An NMR tube is connected to the piston cap for ease of handling and the sample cavity is centered in the NMR probe.

4.2.3 Diffusion Anisotropy Measurement by Pulsed-field-gradient NMR

We apply the robust and simple pulsed-gradient stimulated echo sequence (PGSTE) for all diffusion measurements. $^{1}H_2O$ diffusion in the membrane was measured using a Bruker Avance III WB 400 MHz (9.4 T) NMR equipped with a Micro5 triple-axis-gradient microimaging probe and 8 mm double resonance ($^{1}H/^{2}H$) rf coil. The triple axis gradients each have a maximum value of 300 G/cm and were employed here in three orthogonal directions

relative to the membranes, identified as X, Y and Z in Figure 4.2. Orientation of the membrane stacks in the magnetic field were verified using a Y-Z image slice collected with a RARE pulse sequence. The PGSTE sequence used a $\pi/2$ pulse time of 32 μs, gradient pulse durations (δ) ranging from 1 – 2 ms and diffusion times (Δ) ranging from 7 – 20 ms, depending on the specific material (see Table 4.1). 32 gradient steps were applied and the maximum gradient strength was selected to produce 70% - 90% of NMR signal attenuation. Due to differences in water uptake, the number of scans varied from 8 to 256 to produce sufficient signal to noise-ratio for each data point. All parameters for the gradient have been calibrated and optimized as reported earlier.[3] As shown in Figure 4.2, X and Y are two orthogonal directions parallel to the membrane plane while the Z direction is perpendicular to the membrane plane. Correspondingly, the measured self-diffusion coefficient is marked as $\boldsymbol{D_{xx}}$, $\boldsymbol{D_{yy}}$ and $\boldsymbol{D_{zz}}$ ($\boldsymbol{D_{\perp}}$). The diffusion anisotropy factor is defined as $\boldsymbol{S_D = D_{//} / D_{\perp}}$, where $\boldsymbol{D_{//}}$ is the average value of the in plane values $\boldsymbol{D_{xx}}$ and $\boldsymbol{D_{yy}}$. Using the sealed cell and triple axis gradient, we can interrogate diffusion along any direction to probe diffusion tensorial properties (anisotropy) without readjusting the membranes orientation. This feature greatly enhances the accuracy and reliability of the measurements.

4.2.4 ^{2}H NMR Spectroscopy

^{2}H NMR experiments were performed additionally to observe orientational ordering in the ionomers. This technique can assist in determining the alignment modes of materials with anisotropic structures,[3,19,22] Single pulse experiments ($\pi/2$ = 20 μs) were performed with repetition time of 0.5 s and number of scans ranging from 256-1024, depending on D_2O uptake. The studied materials were soaked in D_2O (99.9%, Cambridge Isotope Labs) with the measured uptake ranging from 6 - 20 wt %. Home-built Teflon cells with different configurations were utilized to allow orientation of membrane stacks either vertically or horizontally with respect to

the magnetic field. These cells were placed inside the above described imaging probe and rf coil. Relevant detailed procedures are summarized in our previous report.[3] Deuterium quadrupole splittings $\Delta\nu_Q$ were obtained by fitting each spectrum with two Lorentzian peaks using NutsPro software (Acorn NMR Inc., Livermore, CA).

4.3 Result and discussion

4.3.1 Sealed Sample Cell: Stable NMR Measurements on Water-Swollen Membranes

Figure 4.3 clearly illustrates the effectiveness of using the sealed cell. When a membrane is placed into a regular NMR tube, the measured diffusion coefficient (solid symbols) decreases linearly over the "equilibration" time. This phenomenon is due to water in the membranes evaporating into the space around the sample, resulting in the continual decrease of water diffusion. This same effect is seen in capped tubes, but to a lesser extent. In contrast, using our sealed cell (open symbols), and after 1 hour equilibration time, one observes no change in the measured diffusion coefficient over hours or even days, which demonstrates the function of our sealed cell in obtaining repeatable experiments.

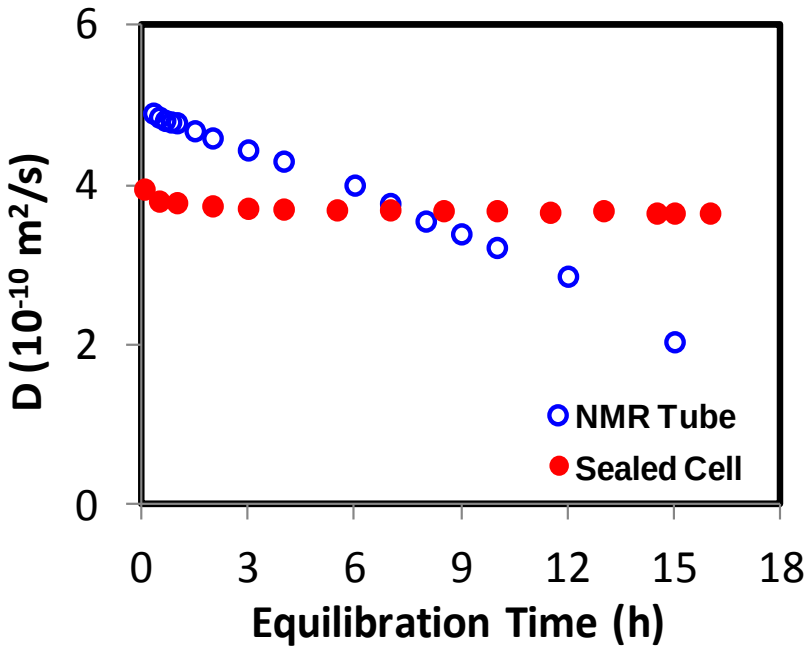

Figure 4.3. Controlled water content in the sealed sampled cell

Water self-diffusion coefficient (*D*) in BPSH-BPS (15k-15k) measured vs equilibration time. *D* decreasesd over time if membranes were put in an open NMR tube (solid); *D* was fairly constant over the whole equilibration time with use of the sealed Teflon cell.

4.3.2 Diffusion vs. Water Uptake

Since both T_1 and T_2 decrease with water uptake, and considering the limits they place on the PGSTE sequence, relevant experiment variables, such as diffusion time (Δ) and gradient pulse duration (δ) are properly selected ($\Delta < 1.5\ T_1$, $\delta < T_2$) to ensure sufficient signal-to-noise ratio and diffusion signal attenuation.

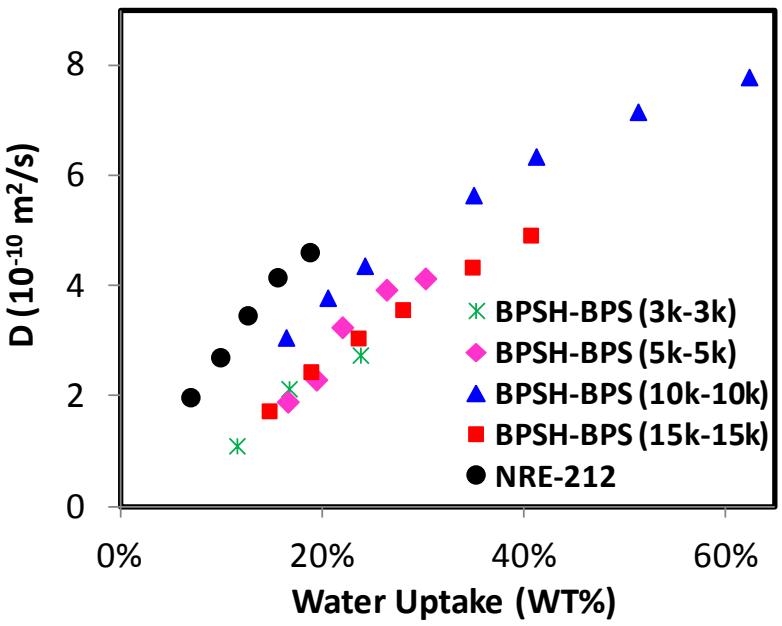

Figure 4.4. Plots of water diffusion in plane ($D_{//}$) vs. water uptake.

Results allow for comparison of water diffusion vs. water uptake among different materials. Error bars are within the size of each data point.

Following these conditions, Figure 4.4 shows the results of in-plane diffusion ($D_{//}$) measurements vs. water uptake. In order to further assess membrane transport and defect structure, we attempted to probe restricted diffusion over a range of Δ. At high water uptake (40-60%), *D* does not vary with Δ in the range of 10-30 ms ($\boldsymbol{T_1}$ and $\boldsymbol{T_2}$ limited) for any of these materials. At low water uptake, however, due to hardware (imaging probe) limitations (g_{max} = 300 G/ cm) as well as the short $\boldsymbol{T_1}$ and $\boldsymbol{T_2}$ values, the range of Δ cannot be varied substantially above 10 ms. For all materials, water diffusion coefficients monotonically increase with water uptake. Among the block copolymers, BPSH-BPS (10k-10k) exhibited the best water transport, which we attribute to its ordered morphology and high connectivity among hydrophilic domains.[2] Here, the length scale probed by the NMR diffusion measurement can be estimated via calculating the root-mean-

square displacement of a molecule undergoing a 1D random walk: $< r^2 >^{\frac{1}{2}} = \sqrt{2D\Delta}$, where D is the diffusion coefficient and Δ is the diffusion time in the PGSTE pulse sequence. In the case of BPSH-BPS (10k-10k) for instance, where $D_{//}$ varies from $3x10^{-10}m^2/s$ to $8x10^{-10}m^2/s$, we find that the diffusion length $< r^2 >^{\frac{1}{2}}$ ranges from 2.5 - 4 μm (Δ = 10 ms). In addition, at nearly the same water uptake, the water self-diffusion coefficient for BPSH-BPS(5k-5k) is lower than for BPSH-BPS(10k-10k), but slightly higher than that for BPSH-BPS(15k-15k). This indicates that the water transport in these membranes does not monotonically increase with block length, suggesting an optimum morphology or defect structure vs. molecular weight. We also note that the 10k-10k material has a much larger saturation value of the water uptake, allowing faster overall diffusion than the other block lengths or N212. However, when comparing at equivalent water uptake values, N212 attains the fastest water diffusion. The higher saturation water uptakes of the 10k-10k and 15k-15k materials also reflect a different (planar) morphology than the others,[2] which becomes more apparent in the next section.

4.3.3 Diffusion Anisotropy

We observe diffusion anisotropy, defined as the ratio of $\boldsymbol{D}_{//}$ to $\boldsymbol{D}_{\perp}$, ranging from 1.02 to 2.80 in the different materials at ~ 22wt% uptake (see Figure 4.5). Water diffusion in Nafion 212 behaves nearly isotropically as we reported earlier.[3] For the block copolymers, $\boldsymbol{D}_{//}/\boldsymbol{D}_{\perp}$ increased with the increase of block mass but again reached a maximum for 10k-10k. More importantly, $\boldsymbol{D}_{//} / \boldsymbol{D}_{\perp}$ increased by only 15% as the block mass increased from 3k to 5k, whereas the value increased by > 100% as the block mass increased from 5k to 10k. This large enhancement in diffusion anisotropy implies a transition in morphology since water diffusion reflects the symmetry of such structures.

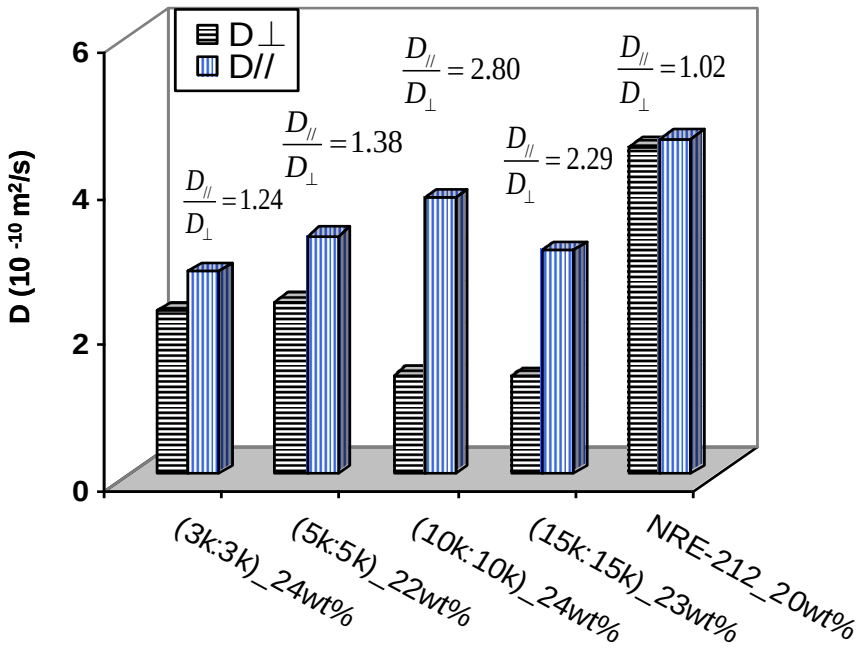

Figure 4.5. Illustration of diffusion anisotropy vs. membrane type

$\boldsymbol{D}_{\perp}$ (Through-plane); $\boldsymbol{D}_{//}$ (In-plane). At nearly the same water uptake, diffusion anisotropy dramatically varies with membrane type. Nafion 212 exhibits isotropic diffusion while BPSH-BPS (10k-10k) shows the maximum anisotropy in diffusion. (Error bar is estimated to be 3% for each data column)

This speculation is further supported by results of diffusion anisotropy vs. water uptake for the different materials as illustrated in Figure 4.6. In general, water diffusion is nearly isotropic for Nafion and only somewhat anisotropic for low block mass copolymers (3k-3k, 5k-5k). In addition, the ratio ($\boldsymbol{D}_{//}$ / $\boldsymbol{D}_{\perp}$) shows no dependence on water uptake in these three cases. This phenomenon most likely originates from similar morphological symmetries intermediate between 3D and 2D, giving rise to predominantly 3D elastic constraints in these materials, the presence of which do not allow preferential contraction or expansion of hydrophilic channels in

any specific direction. Thus, $D_{//}$ and $D_{\perp}$ would be affected similarly and their ratio stays constant.

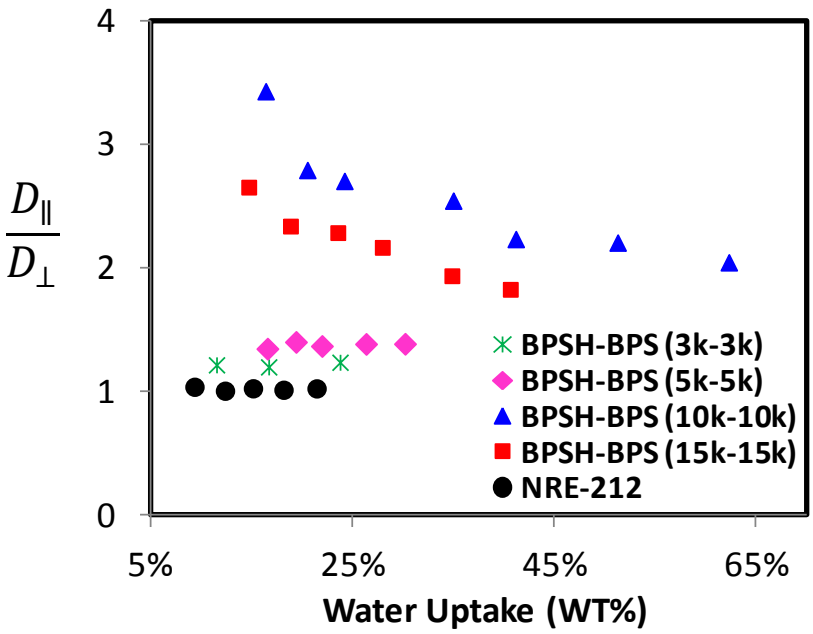

Figure 4.6. Plot diffusion anisotropy ($D_{//}/D_{\perp}$) of different materials vs. water uptake.

For (3k-3k) and (5k-5k) copolymers as well as Nafion 212, $D_{//}/D_{\perp}$ has no dependence on uptake. For (10k-10k) and (15k-15k), $D_{//}/D_{\perp}$ is large and decreases with uptake.

In contrast, $D_{//}$ / $D_{\perp}$ has a strong inverse dependence on water uptake for high block mass copolymers (10k-10k and 15k-15k). This phenomenon provides further evidence for the existence of a uniform planar (lamellar) structure globally within these block copolymers, which also exhibits agreement with the local TEM pictures,[16] wherein layers are stacked through the plane. As a result, the corresponding 3D elastic constraints would be drastically reduced, resulting in a quasi 2D symmetry with less rigidity in the through plane dimension. Such a configuration will lead to substantial growth of layer spacings with water uptake, which also correlates with anisotropic swelling results.[13] In the presence of higher amounts of water

swollen into the membrane, water molecules should experience fewer restrictions as they diffuse through the plane due to the improved connectivity among hydrophilic channels, and furthermore these faster diffusing water molecules should sample a larger average number of defects with pathways through the lamellar planes. However, with reduced water uptake, the smaller diffusion length probed by the water molecules during the measurement time Δ makes it less likely for water molecules to access routes to transport through the plane, thus leading to enhanced diffusion anisotropy.

4.3.4 Probing Alignment with ^{2}H Spectroscopy

To further inform our understanding of anisotropy in these materials, we examined them via quadrupole splittings ($\Delta\nu_Q$) observed in ^{2}H NMR spectroscopy on absorbed D_2O.[3,22] Figure 4.7 shows ^{2}H spectra from membrane stacks oriented in three orthogonal directions along the magnetic field. The broad linewidths in these spectra are due to the intrinsic properties of these materials rather than spectrometer field inhomogeneity. This linewidth may arise from a combination of two possible factors: 1) homogeneous $\boldsymbol{T_2}$ line broadening due to fundamental D_2O-matrix interactions, or 2) distributions of domain orientations where the domains are larger than the diffusion length the molecules sample during the experimental timescale ($1/\Delta\nu_Q$).

Single component ^{2}H lineshapes (two line spectra) are observed in all membranes with maximum splittings $\Delta\nu_Q$ when B_0 is along Z (through plane), thus revealing that these materials are uniformly macroscopically aligned with a symmetry axis (director) perpendicular to the membrane plane. At the same uptake, we observed that peak splitting increases as block mass increases, which represents the enhancement of ordering within the materials. The splittings in the other two in-plane directions are similar to each other and their values are close to half of the maximum splittings. These results exhibit the same pattern as observed in Nafion 212,[22]

indicating that the block copolymers are aligned ***uniaxially***, as would be expected for cast membranes, and which can be described by equation 4.2,[3]

$$\Delta\nu_Q = \frac{1}{2}\Delta\nu_0[3Cos^2\theta - 1 + \eta Sin^2\theta] \qquad (4.2)$$

where $\Delta\upsilon_0$ is the maximum splitting observed for these materials (Z-aligned) and θ is defined as the angle between material alignment axis with respect to the magnetic field direction. η is the biaxiality parameter and it is equal to zero for uniaxially aligned structures. In the present case, we attribute the small non-zero biaxialities (η < 0.06) to variations in both film casting conditions, and to small errors in peak fitting due to the broad linewidths observed.

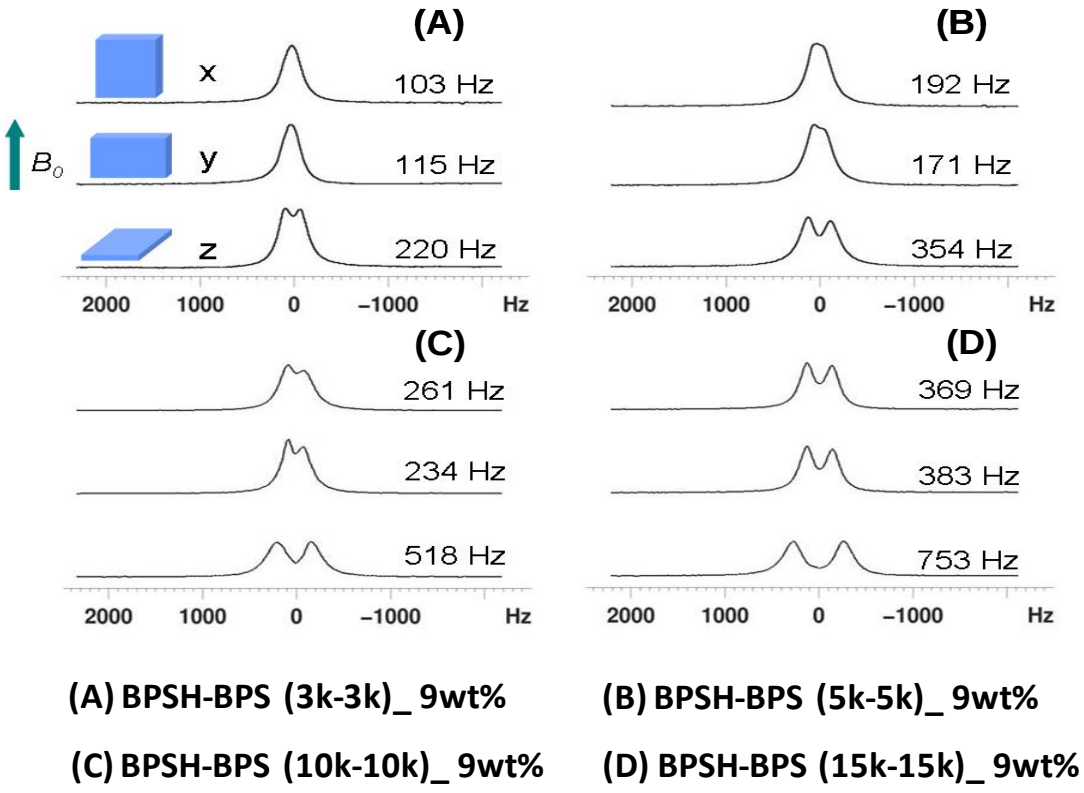

Figure 4.7. ^{2}H spectra of multi-block copolymers vs. block mass

Room temperature ^{2}H spectra of BPSH-BPS multi-block copolymers vs. block mass and at fixed D_2O uptake. Stacks of membranes were oriented in 3 orthogonal directions along the magnetic field $\boldsymbol{B_0}$. Maximum peak splitting $\Delta\nu_Q$ is observed when the membrane plane is perpendicular to $\boldsymbol{B_0}$ (Z direction); Minimum splitting is observed when $\boldsymbol{B_0}$ is parallel to the orientation of the membrane plane (X or Y). Maximum splittings are approximately twice the values of the minimum splittings.

Figure 4.8 lists the results of ^{2}H splittings through the plane vs. D_2O uptake. We attribute the strong inverse dependence of splitting on uptake, especially for high block mass copolymers, as arising from expansion of the hydrophilic channels with water, causing these highly mobile water molecules to experience on average more interactions with other (nearly isotropic) water molecules and fewer anisotropic "confinement interactions" with the channel walls. A striking result lies in that the largest splittings occur for the highest block mass, which contradicts the trend of diffusion anisotropy. We discuss this mystery in the next section.

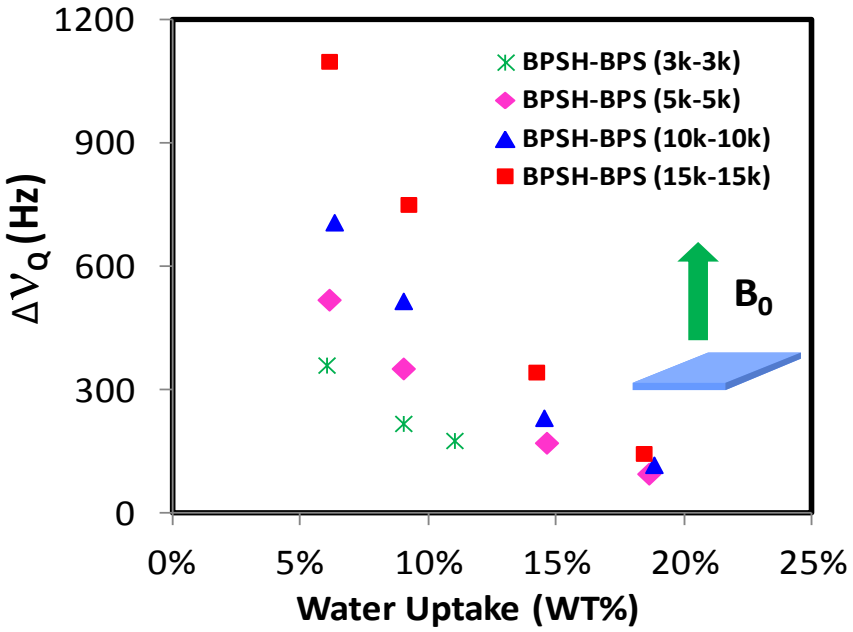

Figure 4.8. ^{2}H splitting vs. D_2O uptake for multi-block copolymers.

The results were obtained at room temperature with membrane stacks oriented perpendicular to $\boldsymbol{B_0}$. Splitting increases dramatically with block mass. Error bars are within the size of each data point.

4.3.5 Length Scales of Anisotropy and Defect Structure

Considering that both water diffusion and ^{2}H splitting measurements will reflect the anisotropy of a specific material, one notices an apparently contradictory pattern when comparing Figure 4.6 to Figure 4.8, where the anisotropy of 10k-10k is higher in the former case, but lower in the latter. To propose an answer to this intriguing question, we will discuss three factors which will mainly contribute to the anisotropy in materials: tilt angle distribution of hydrophilic domains, domain size, and defects (density, distribution, etc.). Our explanation to this paradox is aided by the illustrations in Figure 4.9, based on electron micrographs for similar materials.[16] We assert that the 10k-10k copolymer possesses more tilted domains, containing fewer dead ends (defects and layer plane tilt reversals) along the in-plane direction. On the other hand, 15k-15k possesses more uniformly oriented domains with more dead ends at length scales below the diffusion length, but on the same or larger scale than the ^{2}H spectroscopy measurement length scale (replace Δ with $1/\Delta\nu_Q$ in the random walk expression of section 3.2 to get ~ 0.4 μm). From this point of view, in terms of diffusion, water molecules will on average experience less barriers in plane for 10k-10k to give an enhanced diffusion anisotropy. In contrast, with respect to ^{2}H spectroscopy, which is sensitive to the global ordering (average of local ordering) of a material but probes a smaller length scale, it is reasonable that although 15k-15k contains more dead ends, it will exhibit larger quadrupole splittings due to its more uniformly aligned lamellar structure. In other words, as the dotted circle scans through the whole

picture of figure 4.9A and 4.9B to average over the local ordering, one would expect to obtain a higher splitting value for 15k-15k, given the fact that more local domains are aligned along the director. The structures in figure 4.9 are somewhat exaggerated to illustrate these points, which form a cohesive (if not infallible) explanation of our results. Thus, the combination of diffusion anisotropy and ^{2}H spectroscopy provide distinct yet complementary information regarding the symmetry of morphological anisotropy and transport on different length scales and time scales.

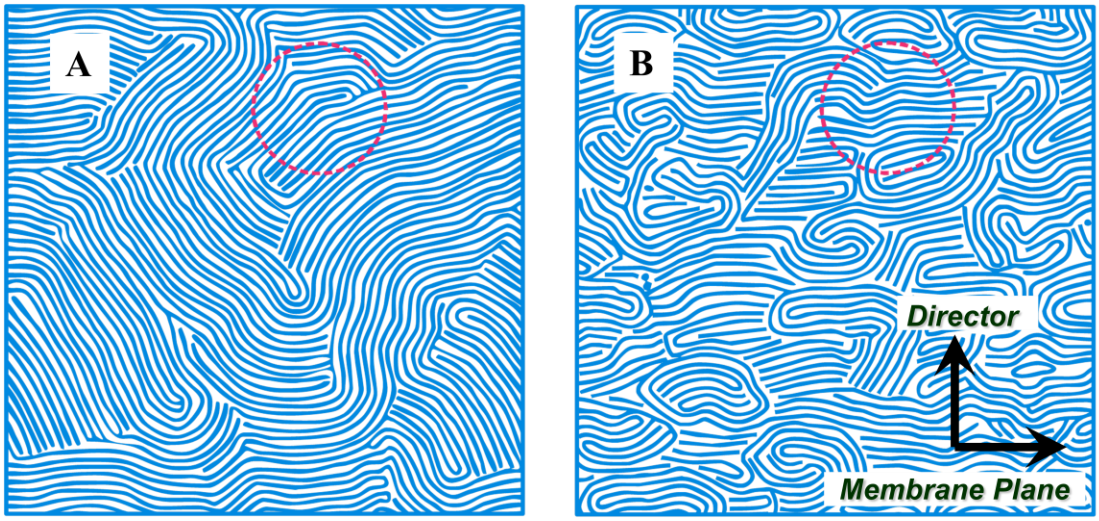

Figure 4.9. Illustrative models of morphologies for 10k-10k (A) and 15k-15k (B).

The model is based on NMR diffusion and ^{2}H spectroscopy results. The director on average is perpendicular to the membrane (and lamellar layer) plane, as indicated by the black arrow. The dotted circle in figure 4.9 serves to represent the average length scale that D_2O molecules sample during the spectroscopy experiments (~ 0.4 μm), thus reflecting more local alignment qualities. The diffusion experiments probe substantially larger length scales (~ 4 μm), comparable to the size of these pictures. Based on these NMR results we conclude that, compared to 10k-10k, the average local ordering is higher in 15k-15k resulting in less variation in domain tilt angles thus

larger ^{2}H splittings, while the defect structure has higher density resulting in lower diffusion anisotropy and slower in plane diffusion. Note layer spacings ~ 30 nm from TEM.[16]

Additionally, in view of the TEM images[16] where the average layer spacing may vary in the range of 20 to 40 nm depending on uptake, one should also note the low value of $\boldsymbol{D}_{//} / \boldsymbol{D}_{\perp}$ in our measurements, which should be higher by at least an order of magnitude as expected for similar materials with very few defects.[27,28] That is, we attribute these reasonably low anisotropy results to the distribution of defects (dislocations and disclinations), the presence of which not only provide pathways for water molecules to transport perpendicular to the lamellae, but also become dead ends to also reduce $\boldsymbol{D}_{//}$. It is quite conceivable that these materials can be controlled further in terms of synthesis and processing in order to minimize defects and improve anisotropy. Indeed, the methods described here provide a quantitative mechanism for feedback on such materials optimization. We are additionally working toward application of diffusion-diffusion correlation spectroscopy (DDCOSY)[29] to further probe the local as well as global anisotropy with the purpose of building a well defined physical model that can describe how defects (density, distribution, type etc.) will affect the diffusion and anisotropy in these and related materials.

4.4 Conclusions

We have performed systematic studies of water diffusion and anisotropy on a class of hydrocarbon multi-block copolymers as well as on Nafion 212. Both diffusion in plane and through plane have been measured and compared for all materials. Various levels of diffusion anisotropy were observed in all the multi-block copolymers, where water diffusion in plane was faster than through plane. In contrast, no anisotropy of diffusion was observed in Nafion 212.

For Nafion 212 and low block mass copolymers (3k,5k), $\boldsymbol{D}_{//}$ / $\boldsymbol{D}_{\perp}$ has no dependence on water uptake over the accessible range. However, a strong dependence of $\boldsymbol{D}_{//}$ / $\boldsymbol{D}_{\perp}$ on water uptake was observed in the high block mass copolymers (10k,15k), which corroborates the existence of macroscopically aligned lamellae parallel to the membrane plane. ^{2}H NMR spectroscopy further demonstrates macroscopically ordered lamellar structures aligned uniaxially with symmetry axis through the membrane plane. The combination of these two methods, each probing a different length scale in the materials, gives quantitative insight into domain sizes, domain alignments, and defect distributions. Further developments of these ideas and applications of these methods will provide a broader and deeper picture of how transport relates to morphology in ionomer membranes.

References

[1] A. Rahardianto, J.B. Gao, C.J. Gabelich, M.D. Williams, Y. Cohen, High recovery membrane desalting of low-salinity brackish water: Integration of accelerated precipitation softening with membrane RO, J. Membr. Sci., 289 (2007) 123-137.
[2] A. Roy, H.S. Lee, J.E. McGrath, Hydrophilic-hydrophobic multiblock copolymers based on poly(arylene ether sulfone)s as novel proton exchange membranes - Part B, Polymer, 49 (2008) 5037-5044.
[3] J. Li, K.G. Wilmsmeyer, L.A. Madsen, Anisotropic Diffusion and Morphology in Perfluorosulfonate Ionomers Investigated by NMR, Macromolecules, 42 (2009) 255-262.
[4] K. Schmidt-Rohr, Q. Chen, Parallel cylindrical water nanochannels in Nafion fuel-cell membranes, Nature Mater., 7 (2008) 75-83.
[5] T.D. Gierke, G.E. Munn, F.C. Wilson, The Morphology in Nafion Perfluorinated Membrane Products, as Determined by Wide-Angle and Small-Angle X-Ray Studies, J. Polym. Sci., Part B: Polym. Phys., 19 (1981) 1687-1704.
[6] S.R. Samms, S. Wasmus, R.F. Savinell, Thermal stability of Nafion(R) in simulated fuel cell environments, J. Electrochem. Soc., 143 (1996) 1498-1504.
[7] Y. Sone, P. Ekdunge, D. Simonsson, Proton conductivity of Nafion 117 as measured by a four-electrode AC impedance method, J. Electrochem. Soc., 143 (1996) 1254-1259.
[8] H.S. White, J. Leddy, A.J. Bard, Polymer films on electrodes. 8. Investigation of charge-transport mechanisms in Nafion polymer modified electrodes, J. Am. Chem. Soc., 104 (1982) 4811-4817.
[9] T.A. Zawodzinski, C. Derouin, S. Radzinski, R.J. Sherman, V.T. Smith, T.E. Springer, S. Gottesfeld, Water-uptake by and transport through Nafion® 117 membranes, J. Electrochem. Soc., 140 (1993) 1041-1047.

[10] P.J. James, J.A. Elliott, T.J. McMaster, J.M. Newton, A.M.S. Elliott, S. Hanna, M.J. Miles, Hydration of Nafion (R) studied by AFM and X-ray scattering, J. Mater. Sci, 35 (2000) 5111-5119.
[11] V. Mehta, J.S. Cooper, Review and analysis of PEM fuel cell design and manufacturing, J. Power Sources, 114 (2003) 32-53.
[12] Y.S. Kim, F. Wang, M. Hickner, S. McCartney, Y.T. Hong, W. Harrison, T.A. Zawodzinski, J.E. McGrath, Effect of acidification treatment and morphological stability of sulfonated poly(arylene ether sulfone) copolymer proton-exchange membranes for fuel-cell use above 100 degrees C, J. Polym. Sci., Part B: Polym. Phys., 41 (2003) 2816-2828.
[13] H.S. Lee, A. Roy, O. Lane, S. Dunn, J.E. McGrath, Hydrophilic-hydrophobic multiblock copolymers based on poly(arylene ether sulfone) via low-temperature coupling reactions for proton exchange membrane fuel cells, Polymer, 49 (2008) 715-723.
[14] M.A. Hickner, H. Ghassemi, Y.S. Kim, B.R. Einsla, J.E. McGrath, Alternative polymer systems for proton exchange membranes (PEMs), Chem. Rev., 104 (2004) 4587-4611.
[15] H. Wang, A.S. Badami, A. Roy, J.E. McGrath, Multiblock copolymers of poly(2,5-benzophenone) and disulfonated poly(arylene ether sulfone) for proton-exchange membranes. I. Synthesis and characterization, J. Polym. Sci., Part A: Polym. Chem., 45 (2007) 284-294.
[16] A.S. Badami, O. Lane, H.S. Lee, A. Roy, J.E. McGrath, Fundamental investigations of the effect of the linkage group on the behavior of hydrophilic-hydrophobic poly(arylene ether sulfone) multiblock copolymers for proton exchange membrane fuel cells, J. Membr. Sci., 333 (2009) 1-11.
[17] E.O. Stejskal, J.E. Tanner, Spin diffusion measuremnts:spin echoes in the presence of a time-dependent field gradient, J. Chem. Phys., 42 (1965) 288.
[18] J.E. Tanner, Use of the stimulated echo in NMR diffusion studies, J. Chem. Phys., 52 (1970).
[19] B. Deloche, E.T. Samulski, Nematic Order in Strained Elastomers via ^{2}H NMR, Bull. Am. Phys.Soc, 26 (1981) 327-328.
[20] C.S. Johnson, Diffusion ordered nuclear magnetic resonance spectroscopy: principles and applications, Prog. Nucl. Magn. Reson. Spectrosc., 34 (1999) 203-256.
[21] W.S. Price, Pulsed-field gradient nuclear magnetic resonance as a tool for studying translational diffusion .1. Basic theory, Concepts Magn. Reson., 9 (1997) 299-336.
[22] J. Li, K.G. Wilmsmeyer, L.A. Madsen, Hydrophilic channel alignment modes in perfluorosulfonate ionomers: Implications for proton transport, Macromolecules, 41 (2008) 4555-4557.
[23] X. Gong, A. Bandis, A. Tao, G. Meresi, Y. Wang, P.T. Inglefield, A.A. Jones, W.Y. Wen, Self-diffusion of water, ethanol and decafluropentane in perfluorosulfonate ionomer by pulse field gradient NMR, Polymer, 42 (2001) 6485-6492.
[24] T. Ohkubo, K. Kidena, A. Ohira, Determination of a micron-scale restricted structure in a perfluorinated membrane from time-dependent self-diffusion measurements, Macromolecules, 41 (2008) 8688-8693.
[25] A.L. Rollet, J. Blachot, A. Delville, O. Diat, A. Guillermo, P. Porion, L. Rubatat, G. Gebel, Characterization of porous structure through the dynamical properties of ions confined in sulfonated polyimide ionomers films, Eur. Phys. J E, 12 (2003) S131-S134.
[26] K. Kidena, Anisotropic diffusion of water in perfluorosulfonic acid membrane and hydrocarbon membranes, J. Membr. Sci., 323 (2008) 201-206.

[27] M.W. Hamersky, M. Tirrell, T.P. Lodge, Anisotropy of diffusion in a lamellar styrene-isoprene block copolymer, Langmuir, 14 (1998) 6974-6979.
[28] P. Wasterby, G. Oradd, G. Lindblom, Anisotropic water diffusion in macroscopically oriented lipid bilayers studied by pulsed magnetic field gradient NMR, J. Magn. Reson., 157 (2002) 156-159.
[29] P.T. Callaghan, I. Furo, Diffusion-diffusion correlation and exchange as a signature for local order and dynamics, J. Chem. Phys., 120 (2004) 4032-4038.

Chapter 5

Correlating Morphology, Proton Conductivity, and Water Transport in Polyelectrolyte-Fluoropolymer Blend Membranes

5.1 Introduction

Generating targeted high performance polymeric materials represents a grand challenge for meeting needs in alternative energy and global sustainability.[1-3] Polymer electrolyte membranes (PEMs) provide a unique medium to selectively transport ions and small polar molecules, therefore manifesting themselves as potential candidates in a variety of applications, from renewable energy materials[1,3-5] to water purification[6,7] to mechanical transducers.[8,9] In general, these ion-containing polymers consist of polar and non-polar segments that nanophase separate to form interconnected channels and domains − a three-dimensional network that enables water transport and ion conduction.[5,10-13] Over the past decade, great effort has been devoted to improving the performance and efficiency of relevant materials and devices.[2,14,15] Sophisticated synthetic strategies allow the creation of advanced materials with tailored properties.[4,16,17] On the other hand, post-synthesis material processing methods such as membrane casting,[15] mechanical stretching,[11] and electric field application[18] can also have an impact on tuning the product's final morphology and structural specificity, which fundamentally determine water and ion transport in polymer membranes.[11,18-20] Thus, systematic investigations on how membrane processing protocols impact transport in polymer membranes will provide instructive guidelines for new material design.

Pulsed-field-gradient (PFG) NMR renders its distinctive role in studies of motions of ions and molecules by virtue of its chemical selectivity and noninvasive nature. This method employs

magnetic field gradients (spatially varying magnetic fields), which couple the detected NMR signal with the average displacement of molecules, allowing the sensitive determination of the self-diffusion coefficient *D* for one or more species in a material.[21-23] NMR diffusometry further takes advantage of long-lived spectral coherences to measure molecular diffusion within a broad range of timescales, typically from ~ 1 ms to 1s. This can provide useful information on the heterogeneity within materials since molecular diffusants sample the host matrix and inherit structural hierarchy and complexity. More specifically, NMR diffusometry offers information on multiple length scales, ranging from ~100 nm up to ~ 10 μm, and when combined with microscopy studies can yield pivotal insights regarding morphology, anisotropy and defect or domain structure.[20,24-27]

In earlier studies,[12,20,24] we have surveyed a range of sulfonated random and block copolymers using multi-modal NMR, and demonstrated that water transport and anisotropy well correlate with morphological variations and structural anisotropy. Here we report detailed experiments and quantitative analysis based on porous media theories on a series of technologically promising polymer blend membranes with respect to morphology, transport, and anisotropy.

We have systematically examined the use of an alkylammonium compatibilizer in forming homogeneous polymer blends and will discuss its influence on membrane morphology and transport. Scanning electron microscopy (SEM), proton conductivity, and restricted water self-diffusion studies reveal the effects of changes in phase homogeneity on key transport parameters. In addition, we have carried out NMR T_1 and T_2 relaxometry studies that probe structural features at a smaller length scale than diffusion measurements. When combined, these findings highlight the utility of tuning the transport properties of polymer blend PEMs by

controlling the morphology and phase homogeneity, and emphasize the power of NMR diffusion and relaxation measurements in correlating transport properties with morphology as well as membrane fabrication.

5.2 Experimental

5.2.1 Membrane Preparation

Membranes were prepared from a solution blend of polyelectrolyte and PVDF (Kynar® 2801 from Arkema Inc.). The polyelectrolyte is a random copolymer of vinylbenzyl sulfonic acid and vinylbenzyl alcohol with a M_w of 143 kg/mol and a polydispersity of 3.15. Molecular weight (M_w) determination was performed using a Waters 2695 Separations Module with a Waters 2414 Refractive Index Detector. Polystyrene sulfonate standards ranging from 1,020,000 g/mol to 697 g/mol were used for M_w calibration. The polyelectrolyte ion exchange capacity was 4.3 meq/g (determined by solution ^{1}H NMR in D_2O). The polyelectrolyte was neutralized at three different levels with a tetraalkylammonium hydroxide (0, 75, and 95 mole % of the available acid groups). The use of the ammonium compound facilitates polyelectrolyte compatibilization with PVDF.[28]

The three polyelectrolytes were blended with PVDF in 1-methyl-2-pyrrolidinone (ACS grade from BDH) to form 20 wt% solutions. The ratio of PVDF to polyelectrolyte was 65/35 (w/w). A blocked isocyanate crosslinker (Trixene® BI7982 from Baxenden Chemicals Ltd.) was added to the solutions in a hydroxide/isocyanate mole ratio of 0.8:1. An organotin catalyst (Fascat® 4202 from Arkema Inc.) was also added to the solution in an amount equal to 0.5 wt% of the solids level. All solutions were blended with a high speed mixer for two hours and allowed to degas overnight before casting.

The solutions were cast into membranes using a Mathis LTE Labdryer. The casting substrate was 2 mil thick aluminum foil with approximate dimensions of 15x12 inches.

Approximately 15g of polymer solution was spread on the foil and drawn down to a wet film thickness of 300 microns using a doctor blade. The films were dried for 6 minutes at 200 ℃. The thickness of the dried membranes was approximately 25 μm.

The membranes were activated in 3 L of 1 M hydrochloric acid to remove the alkylammonium compound and obtain the acid form. The acid bath temperature was ramped from ambient to 80 ℃ at a rate of 40 ℃/hour and held at 80 ℃ for 30 minutes. After removal of the acid, the membranes were washed with 18 MΩ water and subsequently treated with 3 L of 1 M sulfuric acid using the same temperature profile as the hydrochloric acid. The sulfuric acid was then removed and the membranes were washed with 18 MΩ water until the wash water pH was greater than 4. The membranes were labeled A, B, and C, which reflect the different neutralization levels (A = 95%, B = 75%, and C = 0%).

5.2.2 NMR Sample Preparation

Membranes were cut into 4.5 mm × 4.5 mm pieces and stacked (6 - 14 layers) in the same orientation to enhance NMR signal. Membrane stacks were loosely wrapped with poly(tetrafluoroethylene) tape and dried at 70°C for 12 hrs in a vacuum oven to obtain their dry weight before soaking in H_2O until saturation. Water uptake (expressed in wt %) was determined using the following equation:

$$Water\ uptake = \frac{Mass_{wet} - Mass_{dry}}{Mass_{dry}} \times 100\% \qquad (5.1)$$

where $Mass_{wet}$ and $Mass_{dry}$ stand for the mass of wet and dry membranes, respectively. Partially swollen membranes were prepared by controlled evaporation of water before sealing with poly(tetrafluoroethylene) tape and LDPE plastic wrap, and the error in water uptake is less than +/-2%. The membrane stacks were further sealed inside the cavity of a homebuilt

poly(tetrafluoroethylene) sample cell[24] with low dead volume (< 20% of sample volume), which eliminates water evaporation during NMR analyses. Membrane samples were oriented with the in-plane direction along the magnetic field B_0. Diffusion anisotropy was measured by applying pulsed-field gradients along 3 orthogonal membrane axes without repositioning the sample. We use the following axis definitions: X and Y are the in-plane directions and Z is the through-plane direction. An equilibration time of 3 hours after sample cell sealing allowed a steady and even water distribution throughout the partially swollen membranes.

5.2.3 PFG NMR Diffusion and Relaxation Time Measurements

^1H_2O self-diffusion measurements were performed using the PGSTE sequence[29] at 25°C on a Bruker Avance III 9.4 T widebore spectrometer corresponding to a ^1H frequency of 400.13 MHz. A magnetic resonance imaging probe equipped with triple-axis gradients (maximum 300 G/cm) and an 8 mm rf coil was used. The NMR signal attenuation due to diffusion is described by the Stejskal-Tanner equation[21]:

$$I = I_0 e^{-D\gamma^2 g^2 \delta^2 (\Delta - \delta/3)} = I_0 e^{-Db} \qquad (5.2)$$

where I is the spin-echo signal intensity, I_0 is the signal intensity at zero gradient, γ is the gyromagnetic ratio of the probe nucleus (rad s^{-1} T^{-1}), δ (s) is the duration (2 ms in this work) of the gradient pulse with magnitude g (T m^{-1}), and D is the self-diffusion coefficient of water in the membranes derived by fitting equation 5.2. Δ is the duration (7-500 ms in this work) between the leading edges of the two gradient pulses, also known as the diffusion time, and b is commonly known as the Stejskal–Tanner parameter. The proton $\pi/2$ pulse was 32 μs, and a 16-step variation of gradient strength (g) was employed with 4 scans taken at each step. Errors in D are generally < +/- 5%, but at long diffusion times (Δ > 200 ms) can be +/- 10 or 15% due to low

signal-to-noise ratio (SNR). The longitudinal relaxation time T_1 was measured by the inversion-recovery method. Transverse relaxation T_2 was measured using an incremented echo-train CPMG pulse sequence. Errors in T_1 and T_2 values are generally +/- 3%, although the two-component T_1 fits described in section 3.3 below have larger errors of order +/- 10%.

5.2.4 Proton Conductivity Measurement

Membrane samples were cut using a 1 × 6 cm rectangular die and boiled in 18 MΩ deionized water for one hour. The membranes were then mounted in four point probe conductivity cells constructed of acrylic and 0.5 mm platinum wire. The inner electrode distance of the cells was 21 mm. Impedance data was collected in 70 ℃, 18 MΩ deionized water using a Gamry PC4/300 potentiostat connected to a 6 channel multiplexor. Conductivity σ was calculated using dimensions of the hydrated sample, inner electrode distance of the conductivity cell, and the sample impedance at 1,000 Hz (conductivity = inner electrode distance/([impedance]×[sample thickness]×[sample width]). Measurements for each sample were performed at least three times and averaged together.

5.2.5 Scanning Electron Microscopy

Membrane samples were freeze fractured after immersion in liquid nitrogen. The samples were then coated with a gold/palladium alloy using an ion-beam coater from South Bay Technologies (model IBS/e). Cross-section images were obtained for all samples using a LEO 1530 field emission scanning electron microscope (SEM) equipped with an Inlens secondary electron detector. The working voltage and distance were 2 kV and 4 mm, respectively. Images were collected at magnifications ranging from 2,000 – 10,000×, as appropriate to show relevant features in each sample.

5.3 Results and Discussion

5.3.1 Morphology, Anisotropy and Proton Conductivity

Polyelectrolyte processed with different degrees of alkylammonium compatibilizer was blended with PVDF to examine the impact on morphology, water transport, and proton conduction. Figure 5.1 shows the SEM images for membranes processed with the three alkylammonium levels. From membrane A to C, a decrease in ammonium compatibilizer loading is followed by a drastic change in phase homogeneity, from a highly homogeneous phase (A) to partial micron-scale phase separation (B) to a macroscopically phase-separated morphology (C), where the PVDF and polyelectrolyte separate on > 1 μm length scales. Phase separation greatly impacts the proton conduction performance of the membranes as marked in each figure, where the bulk proton conductivity values decrease from 144 mS/cm to 6 mS/cm as the alkylammonium compatibilizer level decreases, showing good agreement with the morphological variations.

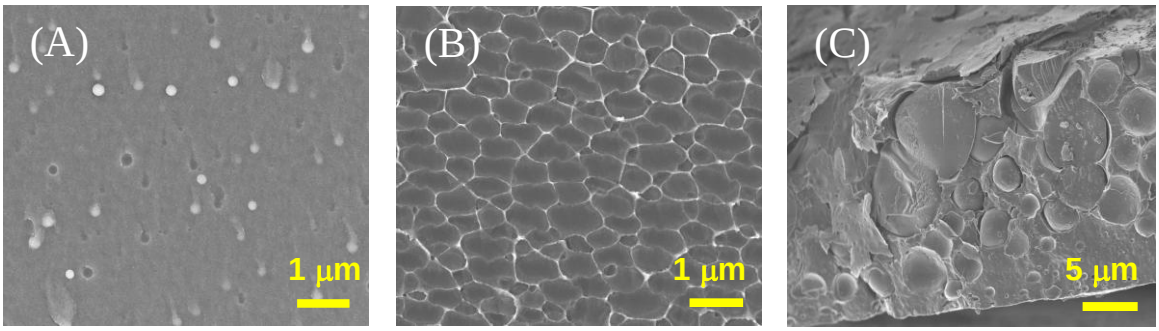

Figure 5.1. Impact of compatiblizer on morphology and proton conductivity (σ) of polymer blend membranes.

Images correspond to freeze-fractured membrane cross-sections. A decrease in compatibilizer loading results in a drastic change in phase homogeneity: from (A) a homogeneous phase to (B)

micron-scale platelet formation (some structural anisotropy) to (C) macroscopic phase separation.

We further measure diffusion along three orthogonal directions (X, Y, and Z) to quantify diffusion anisotropy, defined as $S = D_{xx}/D_{zz}$ or D_{yy}/D_{zz}. Figure 5.2 compares the measured diffusion coefficient in 3 orthogonal directions vs. sample modulations and diffusion time variations. For membrane A with the most homogenous phase (processed with 95% alkylammonium compatibilizer), diffusion is isotropic, at both short (S = 1.0) and long diffusion times (S = 1.1). However, membrane B (processed with 75% alkylammonium) yields notable diffusion anisotropy (S = 1.6), which correlates with the SEM image displaying anisotropic structures (Figure 5.1B). The situation becomes more complicated in membrane C (processed with 0% alkylammonium), as we obtain a non-Gaussian signal decay when fitting diffusion curves with equation 5.2. We attribute this phenomenon to the following: 1) A broad distribution of irregular structures is present, consistent with the structural heterogeneity revealed by the SEM image (Figure 5.1C), where the NMR signal becomes a superposition of signals from individual domains of different sizes, each with distinct diffusion coefficients. 2) Confinement effects due to small domain sizes on average can give rise to anomalous trajectories of water molecules after impinging on domain boundaries, which cause the NMR signal to decay non exponentially, and which has been well illustrated in the case of a well defined single cavity.[30] For simplicity, we fit the decay profile using a single Gaussian component to obtain an average of the measured diffusion coefficient for membrane C. This average diffusion appears to be isotropic regardless of the structural length scale probed (see section 3.2 below), likely due to the broad distribution of irregular structures.

Additionally, considering the membranes are 25 - 30 μm thick (depending on water swelling), one should also be aware of the interfacial effect when measuring diffusion through the plane. Indeed, for membrane A (95 % alkylammonium) we notice that the apparent through-plane diffusion D_{zz} drops off faster than the apparent in-plane diffusion D_{xx} (or D_{yy}) at long diffusion times, and the interfacial effect can partially account for this enhanced diffusion anisotropy. Relevant discussions regarding membrane interfaces affecting time-dependent diffusion behavior will be addressed in detail in a later publication. At this point, we emphasize that the drop in diffusion coefficient is not entirely due to the interfacial effect since we observe similar diffusion behavior in-plane, where the sample dimension (~ 4 mm) is much larger than the water diffusion length (< 10 μm).

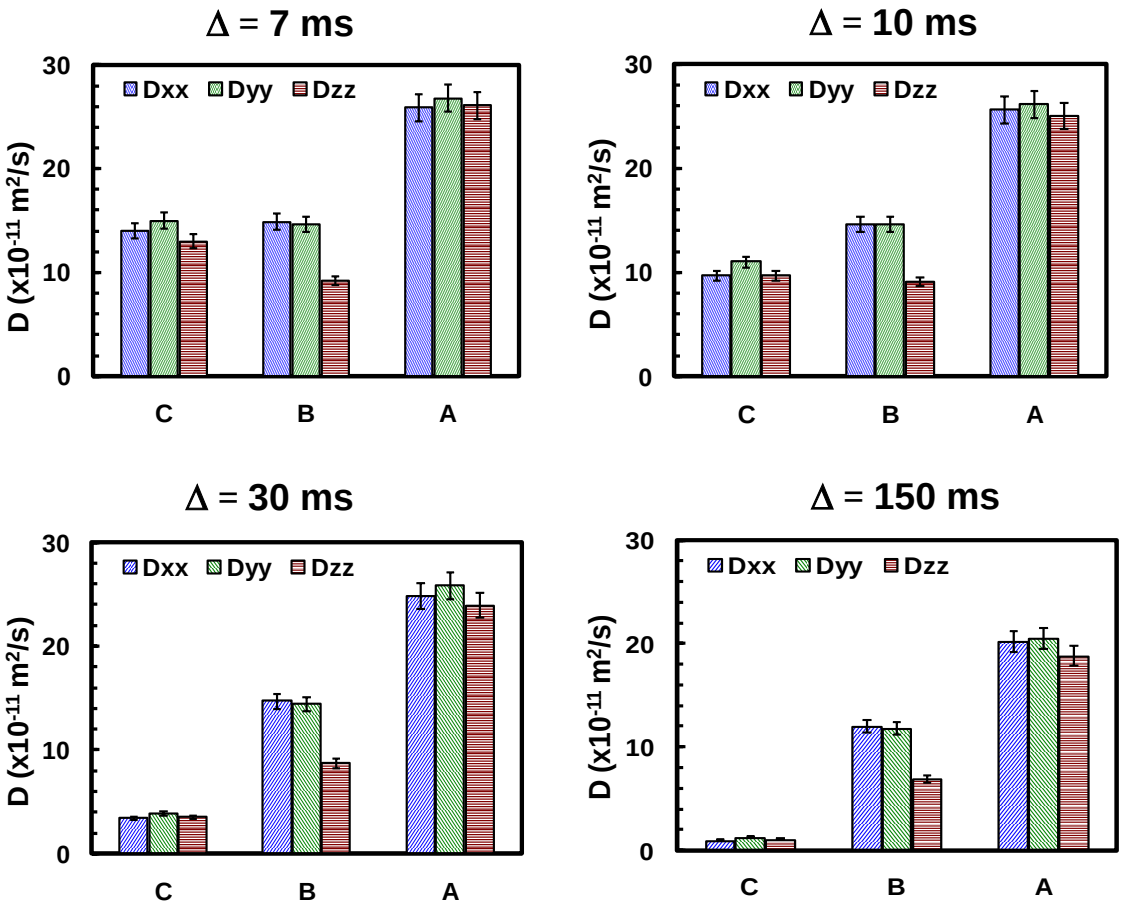

Figure 5.2. Diffusion isotropy and anisotropy among different blend membranes

Comparison of diffusion measured in three orthogonal directions (X, Y and Z) among different blend membranes at equivalent water uptake (24 +/-2 wt%). For membrane C (with 0 % compatibilizer), diffusion is nearly isotropic (D_{xx}/D_{zz} ~ 1.0) and exhibits a strong dependence on diffusion time. For membrane B (75 % compatibilizer), one observes notable diffusion anisotropy (D_{xx}/D_{zz} ~ 1.6), which correlates with the structural anisotropy (platelet structure) revealed by SEM. For membrane A (95 % compatibilizer), diffusion is isotropic (D_{xx}/D_{zz} ~ 1.0).

5.3.2 Restricted Water Diffusion

Figure 5.3 summarizes multi-directional diffusion measurements as a function of water uptake and diffusion time. The figure legend details compatibilizer loading, water uptake, and diffusion measurement direction. For example, the label "#95_48wt%_D_{xx}" designates a membrane processed with 95 % compatibilizer, containing 48 wt % water, and diffusion measurement along the X direction.

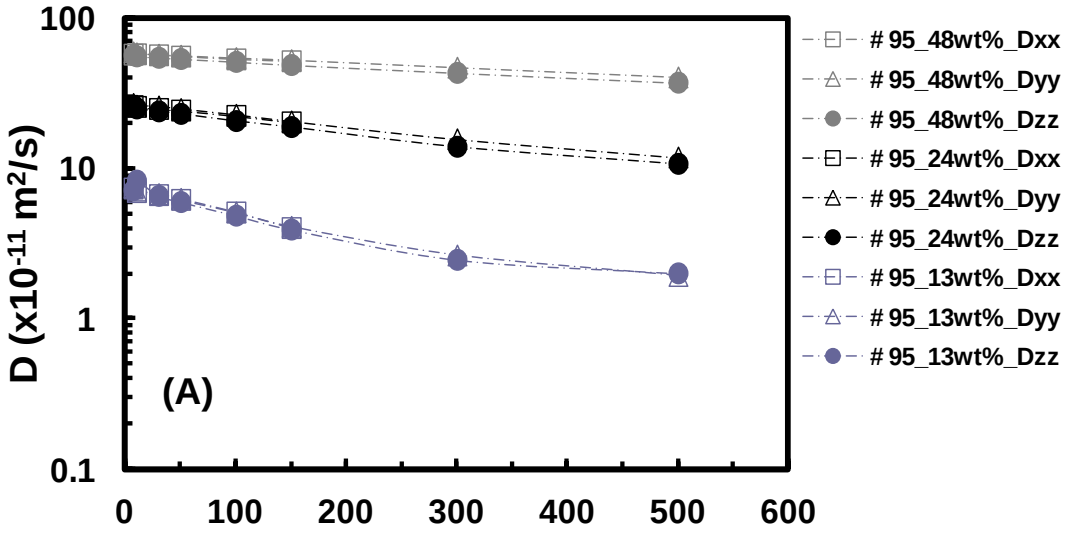

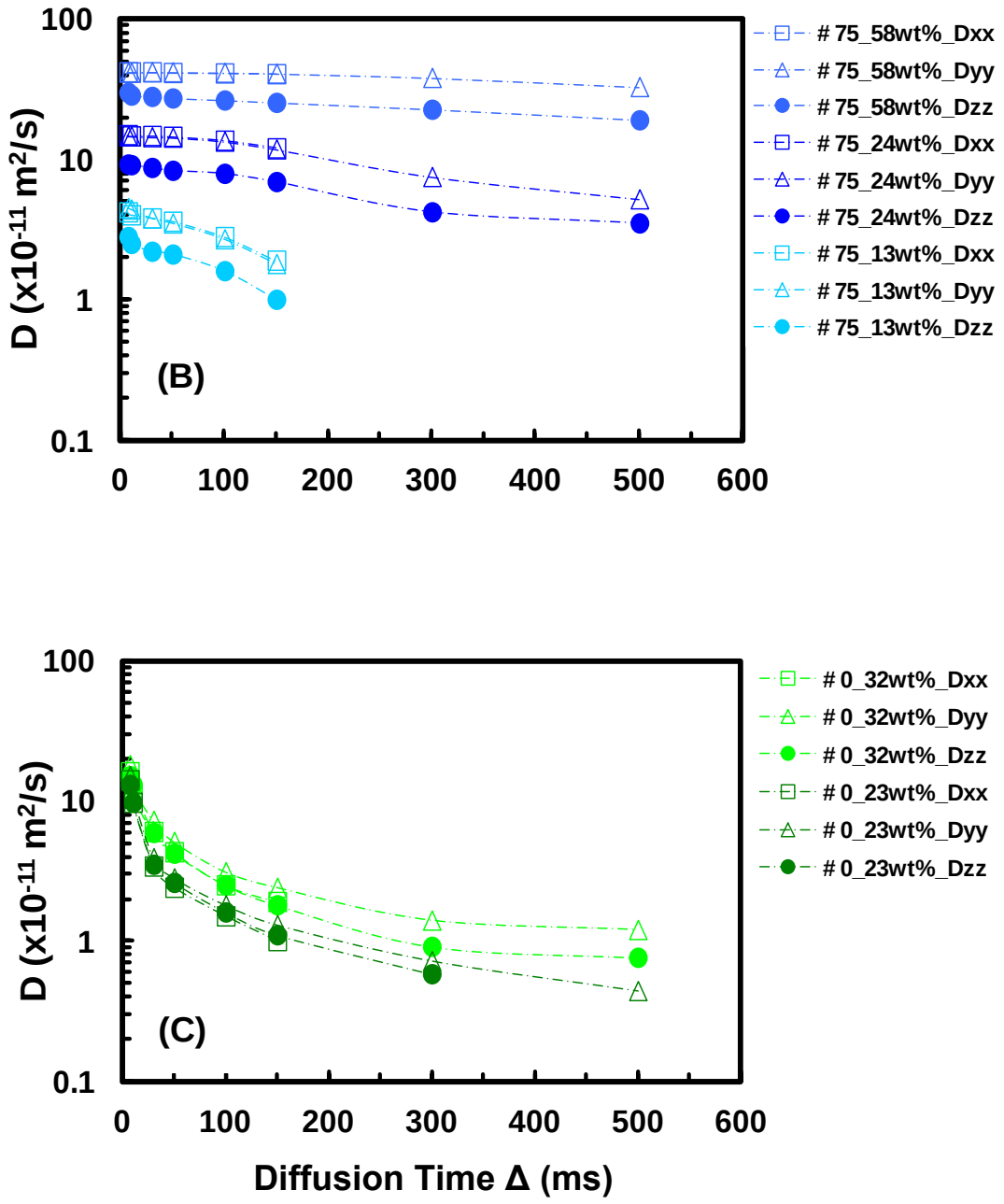

Figure 5.3. Restricted water diffusion vs. water uptake

Diffusion is measured along X, Y, and Z directions. Blend membrane results are shown with decreasing compatibilizer from top to bottom. Measured diffusion coefficient *D* increases with water uptake. However, *D* drops off as diffusion time Δ increases, indicating the presence of micron-scale local barriers sampled by diffusing water molecules. Consistent with the

morphologies observed by SEM, *D* has a relatively weak dependence on Δ for membrane (A) and (B) but a much stronger dependence on Δ for membrane (C). Errors in *D* are ≤ symbol size.

We emphasize that the NMR diffusion experiment reflects the *global material average* over *local transport properties*, therefore complementing the SEM images, which selectively represent local morphology examples. The measured apparent diffusion coefficient *D* monotonically increases as water uptake increases. *D* also monotonically decreases as diffusion time Δ increases for all membranes, a typical phenomenon that characterizes the restricted diffusion process inside polymer membranes due to the presence of local barriers (structural boundaries) sampled by diffusing molecules. The slope of each curve reports on the quantitative effects of restrictions, and this "restriction degree" varies as a function of water content and compatibilizer composition. A variation in water content results in a modest change of restriction degree. In contrast, changing the compatibilizer composition severely influences water diffusion when comparing diffusion curves among Figure 5.3A, 5.3B and 5.3C.

Figure 5.4 further illustrates this effect by plotting *D* versus the diffusion length $< r^2 >^{\frac{1}{2}} = \sqrt{(2D\Delta)}$. $< r^2 >^{\frac{1}{2}}$ is the root-mean-square displacement of molecules during the NMR experiment, a statistical quantity that represents the average distance a water molecule has traveled during the diffusion time Δ at the diffusion rate *D*. We compare restricted diffusion among different membranes at the same (moderate) water uptake of 24 wt% to normalize for differences in water content. A reduction of compatibilizer loading correlates with a drastic decrease in apparent diffusion coefficient *D*, especially in the long diffusion time (Δ) region. This is of great significance since the long-time-limit diffusion coefficient most closely relates to the bulk transport properties of membranes. Thus, one expects strong correlations between long-

time diffusion coefficient and proton conductivity measurements. As expected, membrane A exhibits the largest *D* value, which decreases only slightly (a factor of 2) over a relatively long diffusion length (~10 μm), correlating with its high phase homogeneity and best proton conduction. In contrast, there is a drastic decrease in *D* (a factor of 40) even over a short diffusion length (~ 2 μm) for membrane C, which agrees with its highly heterogeneous morphology and poor proton conduction. For membrane B, water diffusion and proton conduction results fall somewhat below those of membrane A, showing more impeded transport due to a restricted morphology.

To better understand the impact of morphology (domain size, connectivity) on transport in these blend membranes, we consider our membranes as an interconnected porous network and plot *D* vs. $\Delta^{1/2}$ in Figure 5.5 to estimate the average restriction size (domain size) via the Mitra equation[31]:

$$D = D_0(1 - \frac{4}{9\sqrt{\pi}}\sqrt{D_0\Delta}\frac{S}{V}) \qquad (5.3)$$

where S/V is the surface-to-volume ratio and D_0 is the so-called unbounded diffusion coefficient. D_0 is normally the diffusion coefficient one would measure for a pure liquid, if studying conventional porous media with molecules travelling through a network of open pores or channels that are generally > 1 μm in size. In the case of PEMs, we have instead a hierarchy of structures, with molecules travelling through ~ 1 nm-scale interconnected cavities or channels, possibly locally aligned[13] that are in turn part of domains > 100 nm in size.[11,32] In this context, D_0 is now the diffusion coefficient averaged over the ~ 1 nm channels (much smaller than the diffusion length measured), representing an effective unbounded diffusion coefficient for molecules averaged over the local topological and chemical interactions that are far too small to

be probed by NMR restricted diffusion studies. This new application of the Mitra equation holds promise for understanding a wide variety of membrane morphologies.

Equation 5.3 is then valid in the "short time" region for NMR, (diffusion length ~ 1 μm) where a linear regression allows for derivation of S/V values of the ~ 1 μm domains (grains) composed of large collections of nanochannels. If the water diffusion length is comparable to the domain size, a relatively large fraction of water molecules will appear to diffuse slowly due to their collisions with the domain boundaries. Thus, large surface-to-volume ratio (S/V) reflects small domains, and the reciprocal quantity $R_c = V/S$, denotes a structural length scale (of order the domain size) below which water molecules can move relatively freely (fully inside domains). R_c is shown in Table 5.1 and with each fitted curve in Fig. 5, and has an error of < +/- 10 %. Note that R_c increases from 0.8 μm to 5.3 μm as compatibilizer loading increases from 0% to 95%, indicating the formation of larger domains with optimized compatibilizer content. R_c also increases somewhat (by a factor of ~ 2) at higher water uptake (results not shown), signifying an expected enhancement in domain size caused by water swelling hydrophilic structures inside these PEMs.

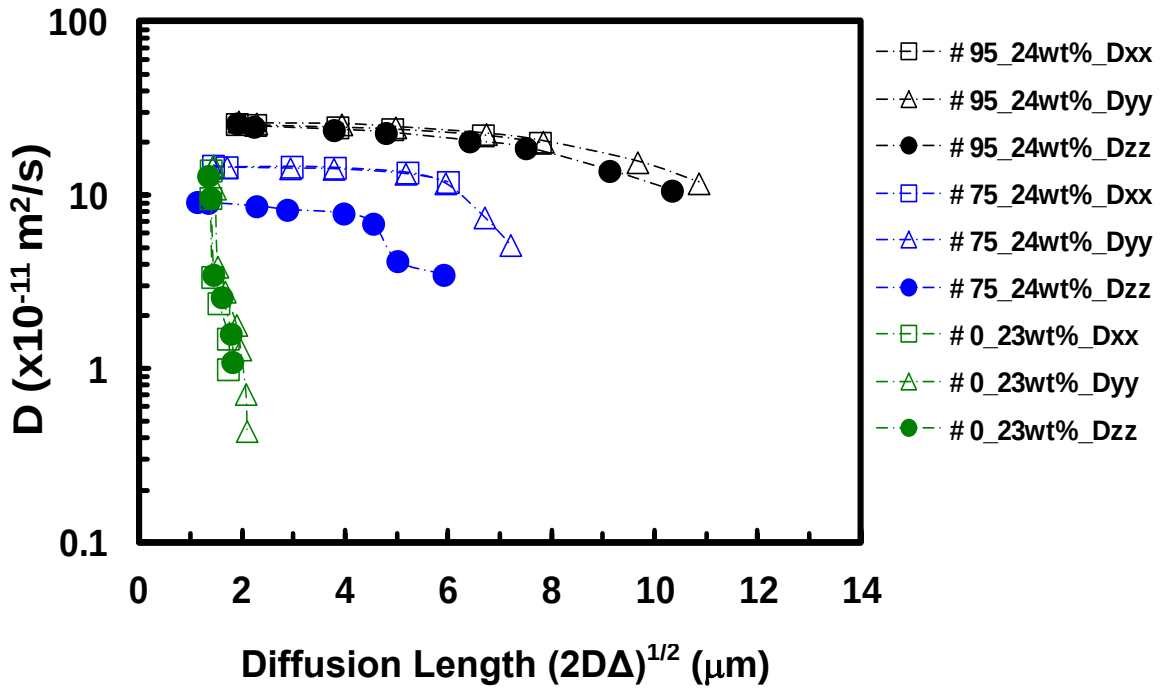

Figure 5.4. Diffusion coefficient as a function of diffusion length vs. membrane type

For membranes processed with different compatibilizer loading, the restricted diffusion behaviors are compared at the same water uptake. As the compatibilizer composition decreases from maximum (95 %) to minimum (0 %), the corresponding *D* decreases by a factor of 2, 3, and 40 respectively for membranes A, B, and C at long diffusion time. Errors in *D* are ≤ symbol size.

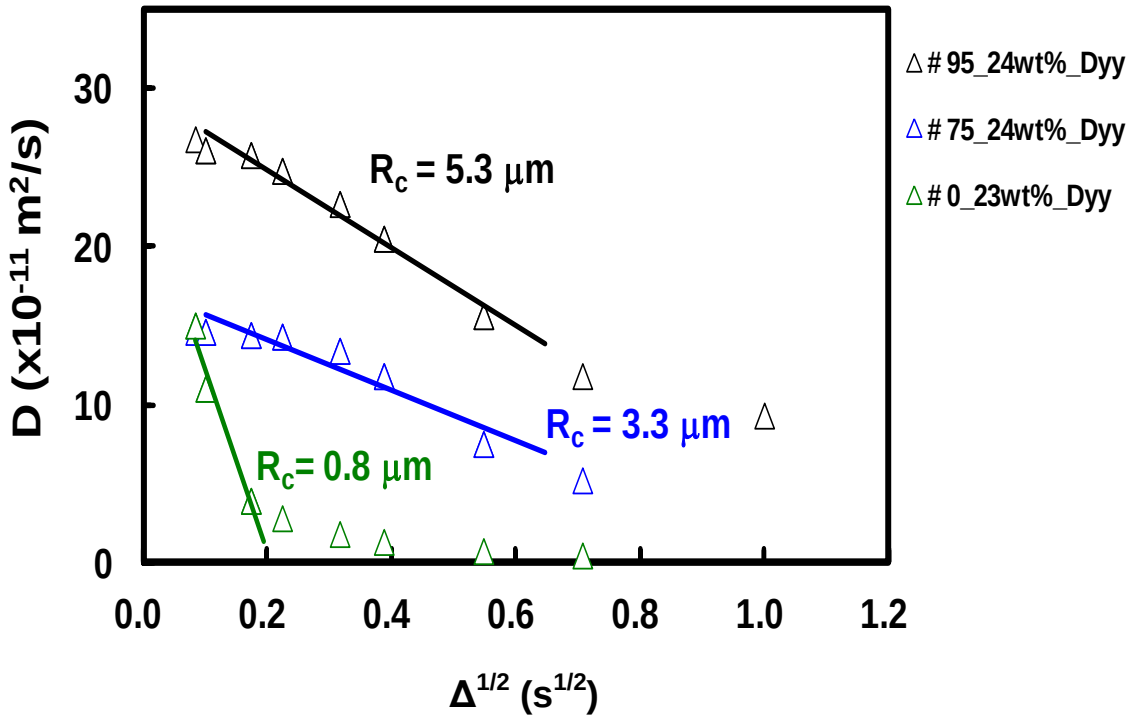

Figure 5.5. Determination of average domain dimension R_c via plotting D vs. $\Delta^{1/2}$

Fitting the linear dependence in the short time regime allows an estimation of surface-to-volume ratio (S/V) using equation 5.3. The reciprocal of S/V, called R_c represents the length scale of structural homogeneity, below which intradomain water diffusion is dominant. With the increment of compatibilizer compositions from 0 % to 75 % to 95 %, R_c increases from 0.8 to 3.3 to 5.3 μm, which signifies improvements in structural homogeneity. Errors in D are ≤ symbol size, and errors in R_c are +/- 10%.

Another key parameter for evaluating an interconnected porous network is the tortuosity $\Im$, where lower $\Im$ represents better domain connectivity within a PEM and thus faster transport. $\Im$ is defined as $\Im = \frac{D_0}{D_\infty}$ based on diffusion measurements. Here, the observed D will reach its plateau value D_∞ in the long-diffusion-time limit, when diffusants experience (average over) all

local structural heterogeneities.[33] Due to limitations in T_1 relaxation times, we can measure water diffusion up to 500 ms and our D_∞ may not completely reach the plateau values for different membranes, as shown in figure 5.3. Nevertheless, we uniformly use the measured diffusion coefficient D at 500 ms to represent D_∞ and quantify $\mathfrak{I}$ for the different membranes (Table 5.1). Here, D_0 is the "nanochannel averaged" unbounded diffusion coefficient derived based on equation 5.3, and we can see its values are relatively close together for the three membranes, and close in magnitude to other PEM observations of D where no restricted diffusion is observed.[19,20] At the same water uptake, there is a drastic decrease in $\mathfrak{I}$ with compatibilizer loading, which strongly demonstrates the improvement in connectivity among PEM domains. For each membrane, $\mathfrak{I}$ also decreases somewhat as water uptake increases (roughly by a factor of 3), signifying an expected increase in connectivity between domains with increasing water content. Note that $\mathfrak{I}$ has an estimated error on the order of +/- 20 % due to the D_0 fits and low SNR in D_{500} measurements. This quantitative analysis of domain size and tortuosity based on restricted water diffusion measurements correlates strongly with the phase homogeneity displayed in the SEM images.

Table 5.1. Tortuosity and domain size for blend membranes

Sample ID	$\mathbf{D_0}$ **(10^{-10} m^2/s)**	$\mathbf{D_{500}}$ **(10^{-10} m^2/s)**	$\mathfrak{I} = D_0/D_{500}$	$\mathbf{R_c}$ **(μm)**
#95_24wt%	3.1	1.2	2.6	5.3
#75_24wt%	1.9	0.5	3.8	3.3
#0_ 23wt%	2.4	0.04	60	0.8

5.3.3 NMR Relaxometry Studies: T_1 and T_2 Measurements

Figure 5.6 shows our T_1 and T_2 results for H_2O in the three PEM samples as a function of water uptake. T_1 relaxation times probe molecular motions on a time scale of ~$1/\omega_0$ (ns), where ω_0 is the ^{1}H larmor frequency (400 MHz), and thus can further inform on the effects of varying membrane type and water uptake. Interestingly, single component fits do not apply to any T_1 curves, although we obtain a single component diffusion coefficient for some of these membranes. Since these T_1 curves fit well to two distinct exponential decay components, we attribute these anomalous T_1 results to two separate mechanisms affecting the motions of water molecules on the $1/\omega_0$ time scale. This implies a structural heterogeneity on a smaller length scale (~ 10 nm) that is not accessible by a PFG-NMR diffusion measurement. Our fits yield a long T_1 component which is an order of magnitude larger than the short component. The origin of this two component behavior requires further study and will form the basis of future work. Strikingly, both long and short T_1 components are independent of compatibilizer loading, likely signifying that local structures in only the polyelectrolyte component of the blend affect the water motion. One explanation for the two components might be that two populations of water are present in two distinct 1-10 nm scale environments.

On the other hand, single component fitting applies well to all T_2 measurements, which probe a larger structural length scale (~ 100 nm, corresponding to ~ 10 kHz molecular motions). Surprisingly, T_1 (both long and short) and T_2 values of different membranes exhibit similar dependence on water uptake as shown in Figure 5.6. These observations again suggest that variation in compatibilizer loading does not affect the intrinsic structural characteristics among blend membranes at or below the 100 nm length scale.

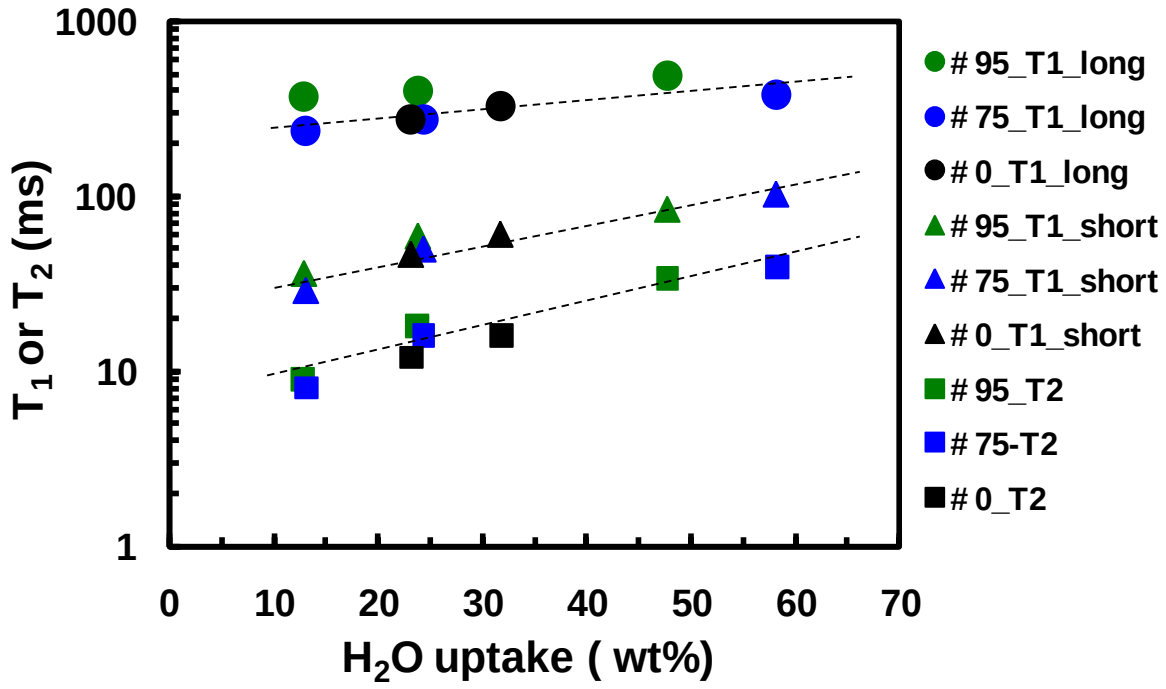

Figure 5.6. T_1 and T_2 relaxation times vs. water uptake and membrane type

Both T_1 and T_2 increase with water content. All T_2 signal decay curves result in single component fits. However, two component fits are applied to measure T_1 values for all samples. The fitted long T_1 component is an order of magnitude larger than the short one. Both T_1 (long and short) and T_2 values show a similar dependence on water utpake, suggesting the existence of similar intrinsic structural characteristics on < 100 nm scales among the three membranes. Errors in relaxation times are ≤ symbol size.

5.4 Conclusions

We have systematically investigated the role of compatibilizers in forming PEM blend membranes by examining their impact on morphology, proton conduction, and water transport properties. Representative SEM images of surface morphology confirm drastic changes in phase homogeneity by varying compatibilizer loading. In agreement with phase homogeneity

variations, proton conductivity varies from 144 mS/cm (optimized compatibilizer loading) down to 6 mS/cm (no compatibilizer). Pulsed-field-gradient NMR reports on the average transport properties and anisotropy in these blend membranes. Our detailed PFG-NMR observations of different levels of restricted water diffusion strongly correlates with the SEM images and proton conductivity measurements, probing the domain structure and tortuosity experienced by diffusing water molecules.

Using the Mitra equation for porous media, we estimate the relevant domain dimension R_c via diffusion measurements and compare R_c values among the different polymer blends. Long-diffusion-time experiments allow for determination of the tortuosity $\mathfrak{I}$ associated with inter-domain diffusion. An increase in R_c and decrease in $\mathfrak{I}$ with compatibilizer loading represent improvements to structural homogeneity and connectivity within the polymer membranes. Finally, NMR T_1 and T_2 relaxometry experiments reveal intrinsic structural features on < 100 nm length scales that are unperturbed by variation of compatibilizer, and these likely are associated with structures inherent only to the polyelectrolyte. The fruitful combination of these methods underlines the significance of phase homogeneity and connectivity for water transport and proton conduction, and exposes the important roles of compatibilizer and component polymer properties in blend membrane fabrication.

References

[1] Y.A. Elabd, M.A. Hickner, Block Copolymers for Fuel Cells, Macromolecules, 44 (2011) 1-11.
[2] J.E. McGrath, H.S. Lee, A. Roy, O. Lane, S. Dunn, Hydrophilic-hydrophobic multiblock copolymers based on poly(arylene ether sulfone) via low-temperature coupling reactions for proton exchange membrane fuel cells, Polymer, 49 (2008) 715-723.
[3] J.E. McGrath, M.A. Hickner, H. Ghassemi, Y.S. Kim, B.R. Einsla, Alternative polymer systems for proton exchange membranes (PEMs), Chem. Rev., 104 (2004) 4587-4611.

[4] S. Holdcroft, E.M.W. Tsang, Z. Zhang, Z. Shi, T. Soboleva, Considerations of macromolecular structure in the design of proton conducting polymer membranes: Graft versus diblock polyelectrolytes, J. Am. Chem. Soc., 129 (2007) 15106-+.
[5] K.A. Mauritz, R.B. Moore, State of understanding of Nafion, Chem. Rev., 104 (2004) 4535-4585.
[6] Y. Cohen, A. Rahardianto, J.B. Gao, C.J. Gabelich, M.D. Williams, High recovery membrane desalting of low-salinity brackish water: Integration of accelerated precipitation softening with membrane RO, J. Membr. Sci., 289 (2007) 123-137.
[7] J.E. McGrath, C.H. Lee, D. VanHouten, O. Lane, J.B. Hou, L.A. Madsen, J. Spano, S. Wi, J. Cook, W. Xie, H.J. Oh, G.M. Geise, B.D. Freeman, Disulfonated Poly(arylene ether sulfone) Random Copolymer Blends Tuned for Rapid Water Permeation via Cation Complexation with Poly(ethylene glycol) Oligomers, Chem. of Mater., 23 (2011) 1039-1049.
[8] M.D. Bennett, D.J. Leo, Ionic liquids as stable solvents for ionic polymer transducers, Sensor Actuat A-Phys., 115 (2004) 79-90.
[9] T.E. Long, A.J. Duncan, D.J. Leo, Beyond Nafion: Charged Macromolecules Tailored for Performance as Ionic Polymer Transducers, Macromolecules, 41 (2008) 7765-7775.
[10] T.D. Gierke, G.E. Munn, F.C. Wilson, The Morphology in Nafion Perfluorinated Membrane Products, as Determined by Wide-Angle and Small-Angle X-Ray Studies, J. Polym. Sci., Part B: Polym. Phys., 19 (1981) 1687-1704.
[11] J. Li, J.K. Park, R.B. Moore, L.A. Madsen, Linear coupling of alignment with transport in a polymer electrolyte membrane, Nature Mater., 10 (2011) 507-511.
[12] J. Li, K.G. Wilmsmeyer, L.A. Madsen, Hydrophilic channel alignment modes in perfluorosulfonate ionomers: Implications for proton transport, Macromolecules, 41 (2008) 4555-4557.
[13] K. Schmidt-Rohr, Q. Chen, Parallel cylindrical water nanochannels in Nafion fuel-cell membranes, Nature Mater., 7 (2008) 75-83.
[14] S. Holdcroft, T.J. Peckham, Structure-Morphology-Property Relationships of Non-Perfluorinated Proton-Conducting Membranes, Adv. Mater., 22 (2010) 4667-4690.
[15] T.L. Yu, H.L. Lin, F.H. Han, A method for improving ionic conductivity of Nafion membranes and its application to PEMFC, J. Poly. Research, 13 (2006) 379-385.
[16] Y.A. Elabd, L. Chen, D.T. Hallinan, M.A. Hillmyer, Highly Selective Polymer Electrolyte Membranes from Reactive Block Polymers, Macromolecules, 42 (2009) 6075-6085.
[17] J.H. Kim, Y.W. Kim, D.K. Lee, K.J. Lee, Single-step synthesis of proton conducting poly(vinylidene fluoride) (PVDF) graft copolymer electrolytes, Eur. Poly. J., 44 (2008) 932-939.
[18] M.J. Park, N.P. Balsara, Anisotropic Proton Conduction in Aligned Block Copolymer Electrolyte Membranes at Equilibrium with Humid Air, Macromolecules, 43 (2010) 292-298.
[19] J.K. Park, J. Li, G.M. Divoux, L.A. Madsen, R.B. Moore, Oriented Morphology and Anisotropic Transport in Uniaxially Stretched Perfluorosulfonate Ionomer Membranes, Macromolecules, 44 (2011) 5701-5710.
[20] J. Li, K.G. Wilmsmeyer, L.A. Madsen, Anisotropic Diffusion and Morphology in Perfluorosulfonate Ionomers Investigated by NMR, Macromolecules, 42 (2009) 255-262.
[21] E.O. Stejskal, J.E. Tanner, Spin Diffusion Measurements: Spin Echoes in the Presence of a Time-Dependent Field Gradient, J. Chem. Phys., 42 (1965) 288-292.
[22] P.S. Pregosin, Ion pairing using PGSE diffusion methods, Prog. Nucl. Magn. Reson. Spectrosc., 49 (2006) 261-288.

[23] J.B. Hou, Z.Y. Zhang, L.A. Madsen, Cation/Anion Associations in Ionic Liquids Modulated by Hydration and Ionic Medium, J. Phys. Chem. B, 115 (2011) 4576-4582.
[24] J.B. Hou, J. Li, L.A. Madsen, Anisotropy and Transport in Poly(arylene ether sulfone) Hydrophilic-Hydrophobic Block Copolymers, Macromolecules, 43 (2010) 347-353.
[25] A.L. Rollet, O. Diat, G. Gebel, Transport anisotropy of ions in sulfonated polyimide ionomer membranes, J. Phys. Chem. B, 108 (2004) 1130-1136.
[26] W.S. Price, Pulsed-field gradient nuclear magnetic resonance as a tool for studying translational diffusion .1. Basic theory, Concepts in Magn. Reson., 9 (1997) 299-336.
[27] P.T. Callaghan, A. Coy, D. Macgowan, K.J. Packer, F.O. Zelaya, Diffraction-Like Effects in Nmr Diffusion Studies of Fluids in Porous Solids, Nature, 351 (1991) 467-469.
[28] J. Goldbach, S. Gaboury, R. Umpleby, J. Parvole, D. Mountz, Blend of ionic (co)polymer resins and matrix (co)polymers, U.S. Patent #7,396,880, (2008).
[29] J.E. Tanner, Use of the Stimulated Echo in NMR Diffusion Studies, J. Chem. Phys., 52 (1970) 2523-2526.
[30] M.L. Milne, M.S. Conradi, Multi-exponential signal decay from diffusion in a single compartment, J. Magn. Reson., 197 (2009) 87-90.
[31] P.P. Mitra, P.N. Sen, L.M. Schwartz, P. Ledoussal, Diffusion Propagator as a Probe of the Structure of Porous-Media, Phys. Rev. Lett., 68 (1992) 3555-3558.
[32] L. Rubatat, A.L. Rollet, G. Gebel, O. Diat, Evidence of elongated polymeric aggregates in Nafion, Macromolecules, 35 (2002) 4050-4055.
[33] L.J. Zielinski, P.N. Sen, Effects of finite-width pulses in the pulsed-field gradient measurement of the diffusion coefficient in connected porous media, J. Magn. Reson., 165 (2003) 153-161.

Chapter 6

Cation/Anion Associations in Ionic Liquids Modulated by Hydration and Ionic Medium

Reprinted with permission from Jianbo Hou, Zhiyang Zhang and Louis A. Madsen, Journal of Physical Chemistry B, **2011**, *115*, 4576-4582© 2011, American Chemical Society.

Abstract

In order to understand the unique solvation and conduction properties of ionic liquids (ILs), we explore their inter-ionic associations modulated by hydration level and ionic medium. Pulsed-field-gradient NMR allows sensitive measurement of separate cation and anion diffusion coefficients, which combine to reflect ionic aggregation. With increasing hydration of ILs, the anomalous ratio of cation to anion diffusion coefficients reverses, then plateaus to values consistent with expected hydrodynamic radii ratios (r_{cation}/r_{anion} = 1.4 for $[C_2mim][BF_4]$). When ILs diffuse inside an ionic polymer, ion associations are modulated by ionic interactions between mobile cations and anions, and drag from fixed $-SO_3^-$ lining the polymer's hydrophilic channels. Surprisingly, cations diffuse substantially faster ($\leq$ 3X) at low hydration inside membranes, revealing prevalent anionic aggregates. At high hydration, isolated anions diffuse faster ($\leq$ 4X) than cations. Probing ionic interactions provides pivotal insight into these subtle fluids, with quantitative implications for electrolyte applications such as batteries and "artificial muscle" mechanical actuators.

6.1 Introduction

Ionic liquids (ILs) are salts consisting of bulky cations and/or anions possessing much lower charge density than simple ionic species (*e.g.*, Cl^-, Na^+, SO_4^{2-}), thus enabling their fluidity

at or near room temperature. The delicate combination of non-covalent interactions among these ions imbue ILs with a curious and useful set of behaviors, highly tunable by cation and anion choice. ILs find expanding applications in catalysis and bioscience, and as electrolytes in batteries and polymer-based mechanical actuators due to their high ionic conductivity, thermal and electrochemical stability, and low volatility.[1,2] When combined with ionic polymers, ILs become potential candidates for the design of ion-based batteries and ionic transducers since they provide mobile charged species while maintaining the performance of these devices after many operation cycles due to their negligible vapor pressure.[3,4] In particular, transport behaviors of both cations and anions in ILs strongly impact the performance of these materials and devices.[5,6] Exploring the interplay among ionic species in ILs will improve our fundamental understanding of ion transport[7-11], thus enabling targeted design of new ILs as well as novel applications.

A viable strategy for probing interactions between cations and anions is pulsed-field-gradient (PFG) NMR diffusometry.[12,13] Ion pairing or aggregation in ILs[14,15] will reduce ion self-diffusion since the diffusion coefficient D is inversely proportional to the size of a diffusing particle as described by the Stokes-Einstein relation:

$$D = \frac{kT}{c\eta r_H} \qquad (6.1)$$

where k is the Boltzmann constant, T is absolute temperature, c is a constant factor depending on the shape and relative size of the diffusing particle to its surrounding fluid,[16] η is fluid viscosity, and r_H is the diffusing particle's hydrodynamic radius. Empirical observations[16,17] and theoretical studies[17] on the inverse proportionality between the diffusion coefficient and viscosity agree with the prediction of the Stokes-Einstein equation, even for molecular-scale diffusants where the factor c is less than the 6π obtained for a hard sphere diffusing particle that is large compared

with the surrounding fluid molecules (no-slip boundary condition). Thus, we propose that for a given equilibrium ionic fluid, *c* is fixed for all diffusing ionic species, and we may use equation 1 to assess relative hydrodynamic radii of ionic aggregates. Great effort has been devoted to understand ion associations in ILs,[18-22] which strongly impact ion transport. Ion conductivity measurements on ILs deviate by 20%-70% from the values calculated using the Nernst-Einstein equation and diffusion coefficients,[22,23] suggesting a moderate degree of ion associations. However, using the Nernst-Einstein equation to estimate ion associations strongly rests on the assumption of a single ion conduction mechanism, which is inappropriate for ILs considering the strong inter-ionic interactions. Further studies are necessary for understanding ion aggregation, and quantifying aggregate populations and dynamics.

We aim to understand specific intermolecular interactions among charged species as reflected by their transport properties via pulsed-field-gradient (PFG) NMR diffusometry. Here we have explored the use of an ionomer (Nafion ©) as a medium to study ion associations in ILs. This ionomer consists of hydrophilic and hydrophobic polymer moieties that microphase separate into a nanoscale network of interconnected hydrophilic channels to facilitate transport of mobile species, such as water molecules and ions.[24,25] Our strategy allows for investigation of effects of acidity (Nafion is a polyacid in the H^+ form), specific molecular interactions between different ions, and the effect of a matrix-fixed ion ($-SO_3^-$ on the polymer) on the motion of IL ions. In our previous study, we examined the effects of IL uptake, temperature and water content on the IL-water-ionomer system, where dramatic acceleration of ion transport was observed with increased hydration.[26]

Here we report striking transport phenomena for four types of ILs based on systematic studies, either as “free liquids” (neat liquids or solutions with water), or absorbed into ionomer

membranes. We scan through a much wider range of water content as compared to our previous study[26] and measure diffusion of mobile species. To accurately study ion hydration, we carefully adjust and maintain water content in all cases using a sealed Teflon cell.[27] Using spectroscopic resolution, we separately measure *D* for water, cations, and anions via PFG NMR.[26] For free liquids, cations diffuse faster than anions by 30-50% at low water content (χ_{water}, mole ratio of water to ILs), while this reverses at high water content. Inside ionomer membranes this effect is greatly enhanced, exhibiting up to 4X faster (slower) cation diffusion at low (high) water contents. Furthermore, at high χ_{water}, the cation/anion *D* ratio in the free liquid state agrees with expected hydrodynamic radii (r_H, equation 6.1), in contrast to free dry ILs, where in all cases studied to date ion aggregation inflates this ratio.[9,26] These results provide new insights into ion associations in ILs, both as free liquids and inside ionomers.

6.2 Experimental Methods

6.2.1 Sample Preparation and Liquid Uptake Determination

Transport behaviors of ions and water in the following four ILs were studied: 1-ethyl-3-methyl imidazolium trifluoromethanesulfonate ([C_2mim][TfO]), 1-butyl-3-methyl imidazolium trifluoromethanesulfonate ([C_4mim][TfO]), 1-ethyl-3-methyl imidazolium tetrafluoroborate ([C_2mim][BF_4]) and 1-butyl-3-methyl imidazolium tetrafluoroborate ([C_4mim][BF_4]). All these ILs were purchased from Solvent Innovation GMBH (Cologne, Germany) with purity >99%. Due to their hygroscopic nature, these pure ILs were further dried in vacuum at 70^{o}C for 48h to remove residual water prior to diffusion measurements, and diffusion coefficients and NMR spectra were checked for stability over time to verify that water absorption was insignificant. Extruded Nafion 117 (N117) membranes with equivalent weight of 1100 (grams of dry membrane per mole of sulfonate groups), were purchased from E.I Dupont in the acid form with

the thickness of 175 μm. Membranes were cut into pieces of 5 mm x 5 mm in size, stacked together to a total mass of ~60 mg and dried in a vacuum oven for 12h at room temperature to determine the dry membrane mass ($mass_{dry}$). The samples were then soaked with IL-D_2O mixtures (D_2O, 99.9%, Cambridge Isotope Labs) at different temperatures to achieve different uptakes. The wet membranes were blotted to remove any free surface liquid (ILs and water) and transferred to a sealed Teflon cell to equilibrate for later diffusion measurement as reported earlier.[27] All diffusion measurements were performed at 25°C after sample equilibration. To vary water content, we allowed the samples to dry in open air while the content of IL in the membranes ($mass_{IL}$) remained constant due to its negligible vapor pressure. Masses of wet membranes ($mass_{wet}$) including water and IL were determined gravimetrically after the NMR experiments. IL uptake and water mole ratio (χ_{water}) were calculated respectively using equations 6.2 and 6.3:

$$IL\ uptake = \frac{mass_{IL} - mass_{dry}}{mass_{dry}} \times 100\% \qquad (6.2)$$

$$\chi_{water} = \frac{mass_{wet} - mass_{IL}}{mass_{IL} - mass_{dry}} \times \frac{M_{IL}}{M_{D_2O}} \qquad (6.3)$$

6.2.2 Diffusion Measurement by Pulsed-Field-Gradient NMR

We apply the robust and simple pulsed-gradient stimulated echo (PGSTE) sequence for all diffusion measurements. We measured ^{1}H and ^{19}F diffusion for ILs using a Bruker Avance III WB 400 MHz (9.4 T) NMR equipped with a Micro5 triple-axis-gradient microimaging probe and 8 mm double resonance ($^{1}H/^{2}H$) RF coil. The triple axis gradients each having a maximum value of 300 G/cm allowed for measurement of diffusion along three orthogonal directions

relative to membranes, denoted as X, Y (in plane) and Z (through plane).[27] Verification of orientations of the membrane stacks in the magnetic field is via using a Y-Z image slice collected with a RARE pulse sequence (Rapid Acquisition with Relaxation Enhancement).[28] The PGSTE sequence used a $\pi/2$ pulse time of 32 μs, gradient pulse durations δ ranging from 2 – 5 ms, and diffusion times Δ ranging from 30 – 600 ms, depending on the uptake of IL and water in the membranes and suited to the corresponding relaxation times. 16 gradient steps with appropriate selection of maximum gradient strength resulted in 50% - 90% of NMR signal attenuation. Due to differences in signal intensity, the number of scans varied from 4 to 512 to produce sufficient signal-to-noise ratio for each data point. All parameters for the gradient have been calibrated and optimized as reported earlier.[27,29]

We have performed diffusion measurements on both free ILs and ILs inside Nafion membranes at room temperature (25^{o}C). For free IL experiments (aqueous solutions), a water mixture (n_{D2O}: n_{H2O} = 9:1) forms a homogeneous phase with ILs as they are mixed. ^{1}H NMR allowed the determination of the mole ratio of water to IL. For ILs inside membranes, depending on the type of ILs and content of liquid (ILs and water) in Nafion membranes, the longitudinal relaxation time (T_1) varied in the range of 580 ms – 1.3s for cations, and 300 ms – 2s for anions. The spin-spin relaxation time (T_2) fell in the range of 5 - 40 ms for cations and 10 - 900 ms for anions. Measurement of cation and anion diffusion vs. diffusion time Δ allowed probing of any possible heterogeneous structures that may exist over the 0.5 – 3.3 μm range. Due to limiting factors within the experiment (gradient strength, relaxation time), Δ could vary over a relatively wide range at higher liquid uptake but Δ was limited (>250 ms) at low uptake to produce sufficient signal attenuation. All measurements resulted in clean single component fittings to determine diffusion coefficients. Consistent with our previous studies,[29,30] diffusion in Nafion

117 membranes was slightly anisotropic (slightly faster diffusion along extruded direction) and we uniformly measured diffusion along the extrusion direction in this study.

6.3 Results and Discussion

6.3.1 Hydration Effects on Ion Transport in Free ILs

For free ILs, we examine a broad range of water content in order to understand how variation in hydration level (water content) affects ion diffusion and thus the intermolecular associations of cations and anions. "Free" is defined as IL or IL+water solution in the liquid state, not inside the ionomers. Figure 6.1 shows the plot of cation, anion, and water (D_2O) diffusion in free $[C_2mim][BF_4]$ vs. water content χ_{water}, which is defined as the mole ratio of water to IL ($n_{water} : n_{IL}$).

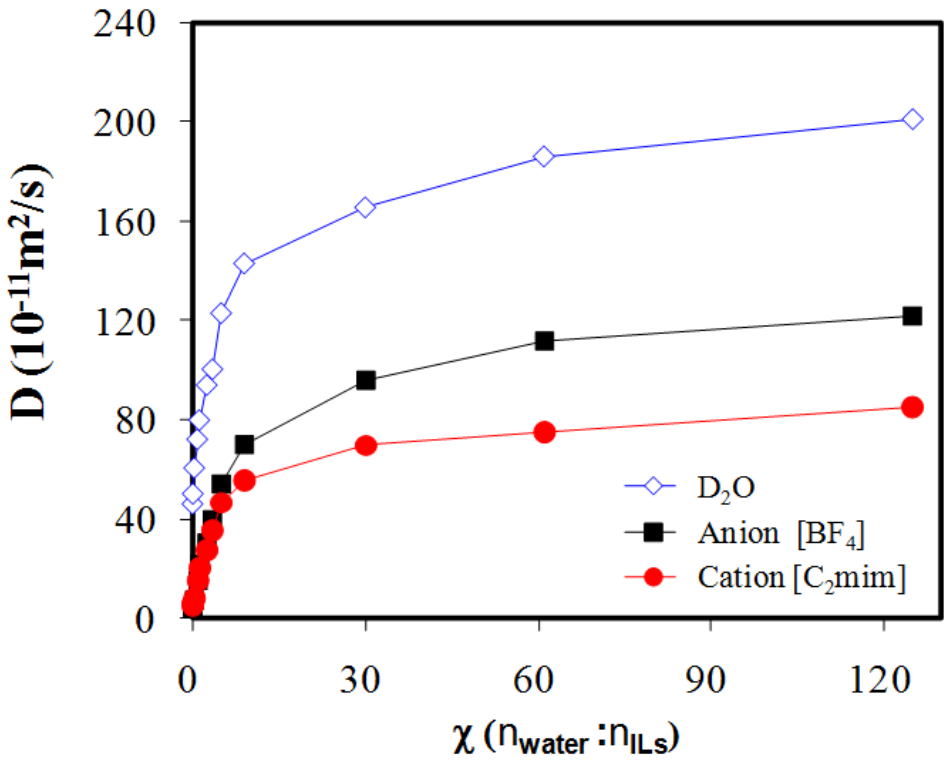

Figure 6.1. Water and ion diffusion of "free" $[C_2mim][BF_4]$ vs. water content

Water and ion diffusion of "free" [C_2mim][BF_4] vs. water content (χ_{water}) at 25°C. D_{cation} is faster than D_{anion} at low χ_{water} but becomes slower than D_{anion} at high χ_{water}. Both D_{cation} and D_{anion} increase with water content, with anion diffusion increasing slightly faster. Error bars are within the size of each data point.

Here, one mole of IL includes one mole of cations and one mole of anions. In general, both cation and anion diffusion increase with water content, however, anion diffusion increases faster than cation diffusion to result in faster moving anions at high water content. To quantify the difference between cation and anion diffusion, Figure 6.2 shows D_{cation}/D_{anion} vs. water content χ_{water} for free [C_2mim][BF_4] and [C_2mim][TfO].

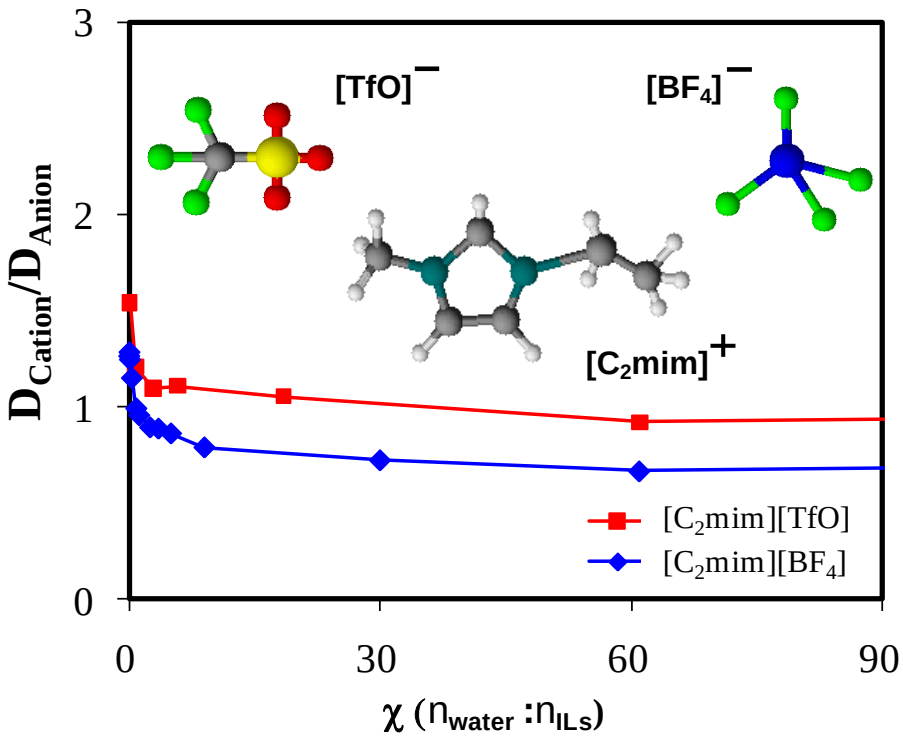

Figure 6.2. Diffusion ratio vs. water content for different ILs

D_{cation}/D_{anion} vs. water content χ_{water} in free [C_2mim][BF_4] and [C_2mim][TfO] ILs. Cations diffuse faster than anions by 30-50 % in the absence of water whereas the trend reverses at high χ_{water},

where the diffusion ratios match those expected from the Stokes-Einstein equation. Errors in D ratios are +/-5 %.

We use equation 6.1 to quantify the difference between cation and anion diffusion in free ILs. Molecular dynamics simulations[31,32] suggest the formation of structured ionic domains in pure ILs due to ion associations (specific molecular packing) the presence of which obscures the picture of isolated ions with uniformly well defined sizes. Thus, at the moment, we cannot directly quantify individual ion size using diffusion coefficients and equation 6.1. Nevertheless, equation 6.1 should provide relative information on transport of different diffusing particles with effective radii r_H, if ions are aggregated.

The average hydrodynamic radii of cation and anion are estimated from the volume of ions mentioned above ($r_H \sim V^{1/3}$).[6] Since these two ions exist in the same thermodynamic phase, D_{cation}/D_{anion} equals the reciprocal of their hydrodynamic radius ratio, or $r_{Hanion}/r_{Hcation}$. Under low χ_{water}, cation diffusion is faster than that of the anion by 30-50%, regardless of its relatively much larger size. However, at high χ_{water}, where ions are fully hydrated and inter-ion interactions are screened, the pattern is reversed and one experimentally obtains $D_{[C_2mim]^+} / D_{[BF_4]^-} = 0.70$ and $D_{[C_2mim]^+} / D_{[TfO]^-} = 0.93$, which agree with the results of density-based ion radius calculations (0.74 for $[C_2mim][BF_4]$ and 0.92 for $[C_2mim][TfO]$).[6] The agreement of diffusion ratio with r_H ratio, as predicted by the Stokes-Einstein equation, supports the picture of totally isolated ions under dilute conditions, shedding light on the puzzle of the anomalous cation/anion diffusion ratio in dry ILs, which is at odds with expected (isolated) ionic radii. In addition, the ratio of water to cation diffusion at low and high water content further supports these arguments, where $D_{water} / D_{[C_2mim]^+}$ approximates to 8.0 and 2.3 respectively under low ($\chi_{water} = 0.035$) and high

($\chi_{water} = 125$) water content. If one estimates the volume occupied by a water molecule from water density ($v = \frac{M}{N_A \rho}$) and uses equation 6.1 to calculate the diffusion ratio, one would expect to have D_{water}/D_{EMI+} equal to 1.8, which is similar to the experimental value of 2.3 at high water content, and implies that the ion's hydration sphere slightly enlarges its effective radius. Again, consistent with cation/anion diffusion at low water content, the unexpected high value of $D_{water} / D_{[C_2mim]^+}$ (= 8) implies specific interactions exist among ions within ILs, which will be further discussed in the next section. Differences in aggregates involving cations and anions must arise from specific molecular interactions (*e.g.*, excluded volume, shape anisotropy, charge distribution, polarizability, hydrogen bonding), among groups of cations and anions in neat ILs.

6.3.2 Hydration Effects on Ion Transport Inside an Ionomer

In order to obtain a fundamental understanding of hydration effects on ion transport in ionomers membranes and to compare ion behaviors with the case of free ILs, we soaked various D_2O-IL mixtures into Nafion© membranes to achieve certain uptakes using our procedures reported earlier.[26] In our previous study, we noticed that the ^1H_2O proton NMR peak shifts as a function of water content, and sometimes overlaps with other IL cation peaks. Using D_2O rather than H_2O to prepare the liquid mixture allows accurate measurement of water diffusion (eliminating multicomponent fitting due to overlap of proton peaks) and simplifies proton spectra as well. Figure 6.3 lists chemical structures of the $[C_2mim]^+$and $[C_4mim]^+$ cations used in this study, along with the relevant proton spectra for free state ILs (dry) and IL-D_2O mixtures soaked into Nafion membranes (spectra for $[BF_4]^-$ counterions shown, spectra with $[TfO]^-$ anions similar but not shown, *See SI*). For IL-D_2O mixtures in Nafion, spectral resolution varies from case to case, depending on the uptake of IL and water in the system (*see SI* for representative

spectra). We observe minimal $^{1}H_2O$ peaks in these spectra due to the high purity of D_2O. In ^{2}H spectra (not shown), we observe only a doublet of $^{2}H_2O$ peaks ($\leq$ 50 Hz splitting) due to the partially averaged quadrupolar interactions of water O-D bonds in the weakly aligned hydrophilic channels.[29] For ^{19}F spectra (*see SI*), one peak appears for $[TfO]^-$ and two peaks for $[BF_4]^-$ (not observable for ILs inside ionomers due to broad line) due to the two boron isotopes present (^{10}B and ^{11}B).

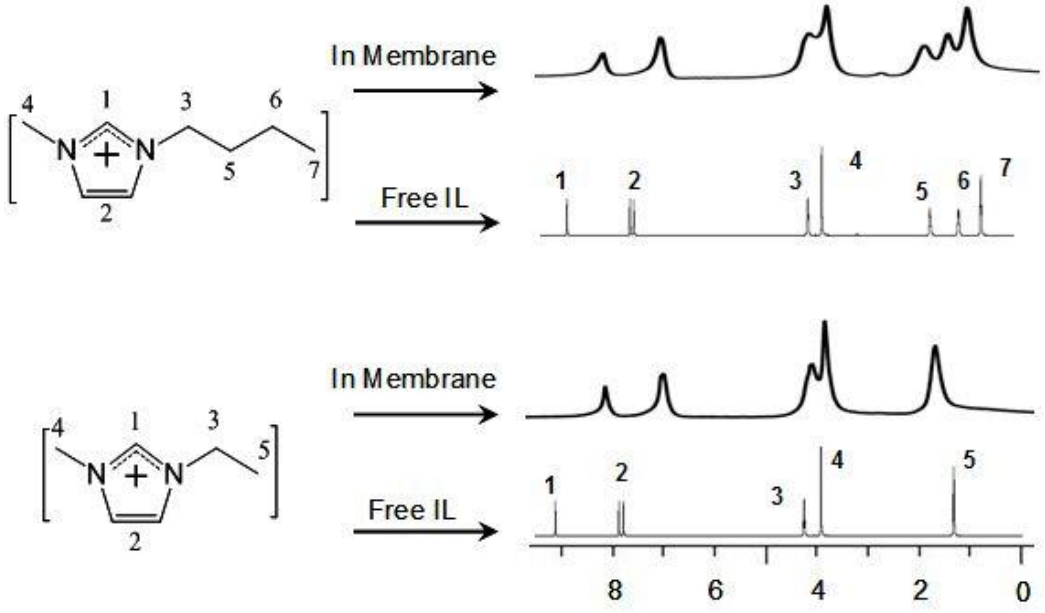

Figure 6.3. Chemical structures of cations and proton spectra at different conditions

Chemical structures of $[C_2mim]^+$ and $[C_4mim]^+$ cations with corresponding ^{1}H spectra for free state dry ILs, and for IL-D_2O mixtures soaked into Nafion (N117) membranes. We assign proton peaks using numbers, as shown. For ILs inside membranes, peak 3 includes a small residual $^{1}H_2O$ signal due to slightly impure D_2O.

Figure 6.4 shows ion diffusion vs. diffusion time of $[C_4mim][BF_4]$ inside the ionomer membrane over a range of χ_{water}. The root-mean-square displacement based on measured

diffusion coefficient $< r^2 >^{\frac{1}{2}} = \sqrt{(2D\Delta)}$ is plotted vs. $\sqrt{\Delta}$, resulting in linear regression for both cation and anion diffusion. Diffusion is independent of diffusion time Δ, characterizing an absence of restricted diffusion effects in these membranes. At relatively high χ_{water}, where ion diffusion is fast and the T_2 relaxation time is long, diffusion is measured over a relatively wide range of Δ (30 ms – 600 ms). Note that this diffusion measurement lengthscale ranges from 0.5 – 3.3 μm (low and high water content, large and small Δ), in agreement with our previous study of ion diffusion in Nafion 212.[26]

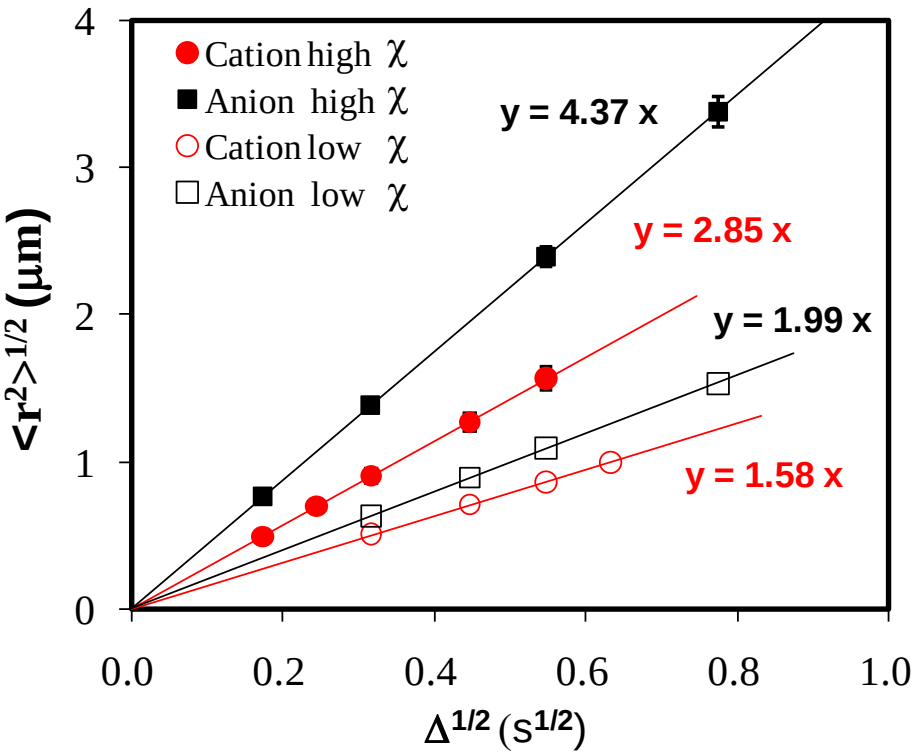

Figure 6.4. Non-restricted ion diffusion inside ionomer membranes

Root-mean-square displacement ($<\mathbf{r}^2>^{1/2}$) of cation and anion vs. $\mathbf{\Delta}^{1/2}$ for [C_4mim][BF_4] IL inside the ionomers membrane at low and high χ_{water}. These linear regressions indicate non-restricted

diffusion behavior in the experimental diffusion length range 0.5 – 3.3 μm. Each individual line slope equals $(2D)^{1/2}$.

In addition, one also notes that the corresponding slopes associated with cation and anion in Figure 6.4 deviate significantly from each other at high water content, reflecting the fact that the slope ratio is equal to the square root of the diffusion ratio. Interestingly, cation and anion diffusion behaviors substantially differ inside the ~ 2 nm hydrophilic channels of Nafion membranes, as revealed in Figure 6.5. We note several attributes of these observations as follows. D_{anion} is more sensitive to the presence of water than D_{cation}, especially at low IL uptake. As IL uptake increases, water still preferentially accelerates D_{anion}, but less strongly. More generally, for BF_4-based ILs ([C_2mim][BF_4], [C_4mim][BF_4]) we observe striking enhancement in anion diffusion as compared to cations (up to a factor of 4.3) at high water content. However, TfO-based ILs ([C_2mim][TfO], [C_4mim][TfO]) exhibit a smaller effect.

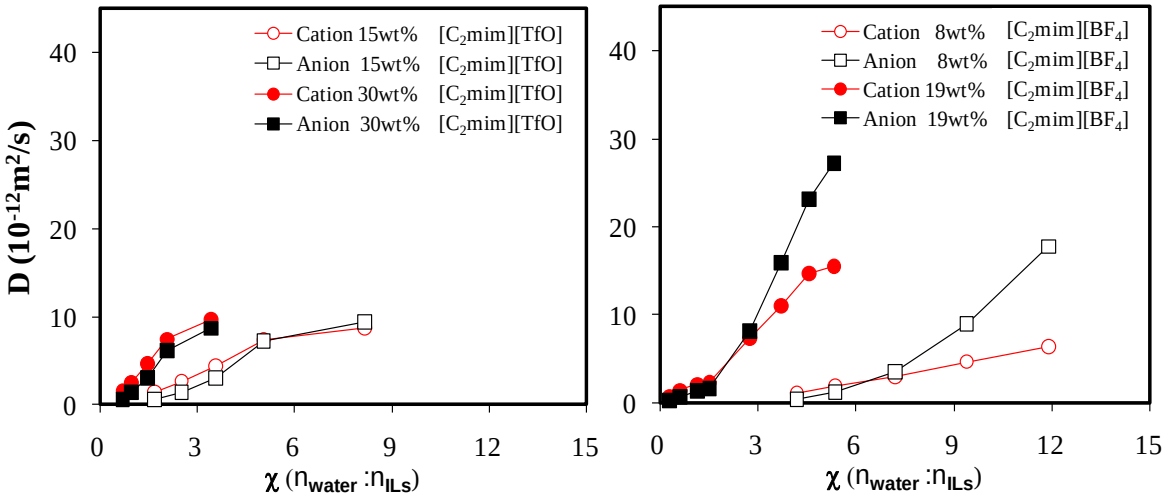

Figure 6.5. Ion diffusion inside membranes vs. water content with different IL uptakes

Cation and anion diffusion inside Nafion membrane vs. water content χ_{water} with different uptakes of [C_2mim][BF_4] and [C_2mim][TfO]. Higher IL uptake results in substantially faster ion

(cation and anion) transport under the same χ_{water} value. Water accelerates the transport of both cation and anion whereas the anion is more highly accelerated than the cation for $[C_2mim][BF_4]$.

We attribute such observations to the following factors: 1) interactions of polymer-fixed sulfonate groups and cations, 2) difference in basicity and ion pairing between $[TfO]^-$ and $[BF_4]^-$.[33] Sulfonate groups on the side chains can attract positively charged species to reduce the average transport of cations inside the hydrophilic channels of Nafion. $[BF_4]^-$ will be more inert than the more Lewis-basic $[TfO]^-$ anion[33] and thus will travel more freely. On the cation side, $[C_2mim]^+$ or $[C_4mim]^+$ will tend to equally pair with free $[TfO]^-$ and fixed $-SO_3^-$ groups on the polymer chain due to the similarity in chemical structures between these two anions. Thus, in TfO-based ILs, cations and anions are more likely to move in pairs (than BF_4-based ILs) and show less enhanced anion diffusion. One may suppose that fast diffusing $[F]^-$ may be generated, which might skew our diffusion measurements in the BF_4-based systems. We emphasize that there is no evidence of hydrolysis for $[BF_4]^-$ inside ionomers at high water content since we obtained a single ^{19}F spectral peak (no other observed ^{19}F anion signals) and a single diffusion coefficient over the full range of membrane hydration. It is also worth mentioning that even at high water content, interactions (columbic, ion packing) between cation and anion are only partially screened by water molecules for ILs inside ionomers, as compared to the case of free ILs. This effect is illustrated by the diffusion ratio of water to anion as shown in Figure 6.6. Here the Stokes-Einstein equation can aid in understanding ionic interactions in our water-IL-ionomer systems. As mentioned earlier, our measured apparent diffusion coefficients exhibit no dependence on diffusion lengthscale, which suggests the diffusion results on both water and ions should equally reflect global (averaged over ~ 1 μm) information on structures as sampled by diffusants. Based on this consideration, the global viscosity should affect both ions and water

molecules in the same way. Thus, one can rule out the factor η in the Stokes-Einstein equation and compare the diffusion ratio (D_{water}/D_{anion} or D_{water}/D_{cation}) inside ionomers with the values for free ILs to understand the degree of ion association. For example at $\chi_{water} = 9$, the diffusion ratio of water to anion $D_{water}/D_{anion} \approx 12$, in contrast to the corresponding values for free water-IL mixture ($D_{water}/D_{anion} \approx 2$) mentioned earlier.

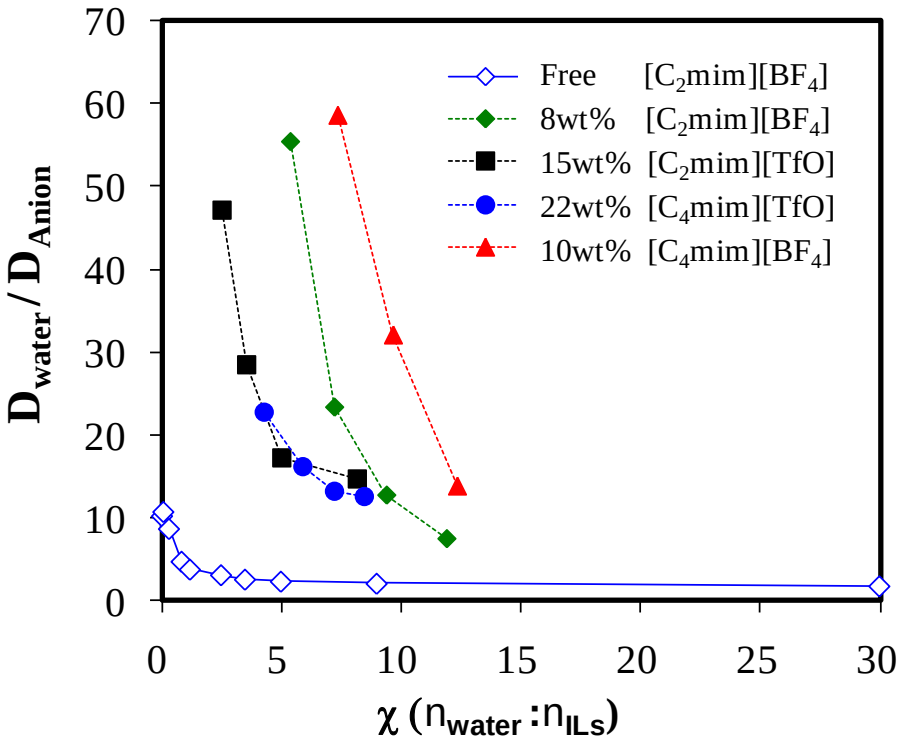

Figure 6.6. (D_{water}/D_{anion}) vs. water content for free IL and IL inside Nafion membrane

Diffusion ratio of water to anion (D_{water}/D_{anion}) as a function of water content χ_{water} for free [C_2mim][BF_4] and for ILs inside Nafion membrane. Even at high hydration ($\chi_{water} \sim 9$), water diffusion in Nafion is > 10X faster than anion diffusion, as compared with free IL, where water is only 2X faster. The difference between D_{water} and D_{anion} drastically increases as χ_{water} decreases, indicating the interactions among ions and ion-charged polymer at low χ_{water} are

more dynamically constrained than at high χ_{water}, while water moves relatively freely at low hydration.

Moreover, as shown in Figure 6.6, in comparison with free ILs, D_{water}/D_{anion} inside the ionomer increases drastically as the hydration level decreases, indicating progressively enhanced ionic interactions that highly impact the translational motion of ions. As a result, these strong ionic interactions among ions and ion-lined polymer nanochannels critically determine the transport properties of IL-based materials and devices at both high and low water content.

We further examine ion transport inside ionomer membranes at low water contents. As a result, in order to further assess specific ionic associations as a function of hydration and IL uptake, Figure 6.7 summarizes systematic results regarding cation and anion diffusion vs. water content for different types and uptakes of ILs. Surprisingly, D_{cation} becomes substantially faster than D_{anion} at low water content for C_2mim-based ILs, where D_{cation}/D_{anion} approaches 2.5 for [C_2mim][TfO] and 3.0 for [C_2mim][BF_4]. This clearly contradicts the conventional expectation that cations will diffuse slower in an anionic matrix due to drag from the polymer-fixed sulfonate groups. Again, considering that both cations and anions exhibit non-restricted diffusion behavior in the same phase, differences in viscosity experienced by cations and anions can be ruled out, and specific ionic interactions should account for these phenomena. In addition, as compared to the diffusion ratios for free ILs, these results strongly demonstrate the formation of ionic aggregates with specific features,[34] based on which we postulate the prevalence of anion-rich ionic aggregates inside the ionomer at low water content. The use of ion aggregation to explain the behavior of concentrated ionic solutions has a long history, both in solutions[35] and inside polymer.[36] For ion-dense fluids such as these ILs at low hydration, many-body effects will likely

be prevalent and thus difficult to conceptualize. With this in mind, we begin by attempting to understand the problem in terms of ionic aggregates.

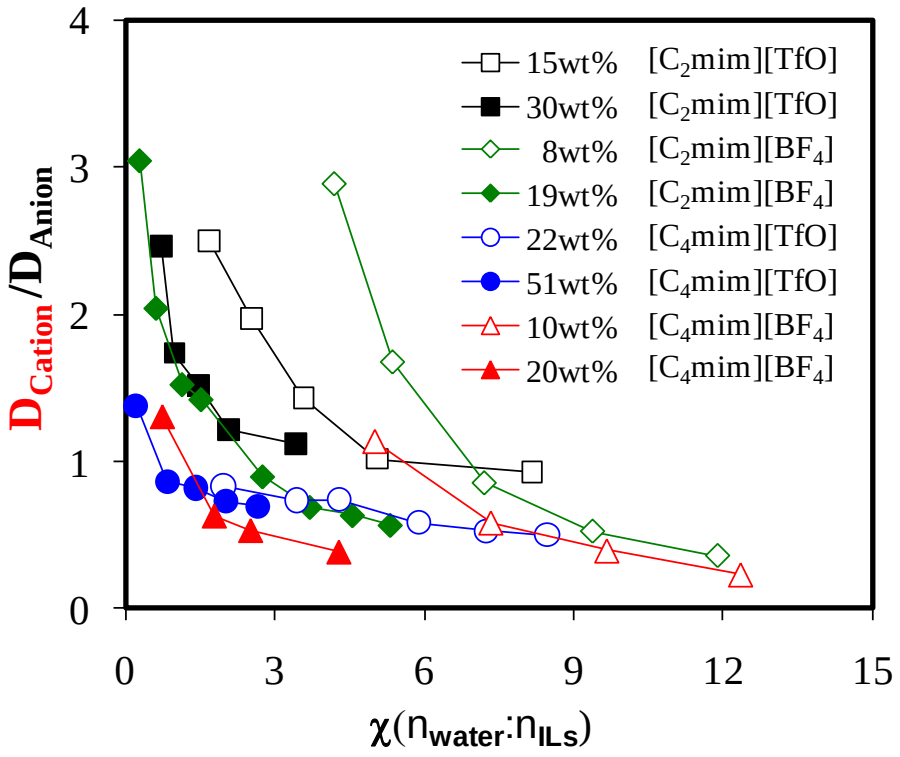

Figure 6.7. Impact of χ_{water} on D_{cation}/D_{anion} inside membranes vs. IL types and uptakes

Anion diffusion dramatically accelerates at higher hydration levels for BF_4-based ILs, and D_{anion}/D_{cation} reaches 3 and 4 for [C_2mim][BF_4] and [C_4mim][BF_4], respectively. At low hydration, cation diffusion becomes substantially faster than anion diffusion for [C_2mim][TfO] and [C_2mim][BF_4], where D_{cation}/D_{anion} reach 2.5 and 3.1 respectively.

We explain our rationale for aggregation as follows. Considering the NMR experimental time scale (~100 ms) during which ionic clusters form and disassociate due to fast dynamic processes (~ ns to 100 ps), our NMR measurements on ion transport (cation or anion) represent

average diffusion behaviors of all the ionic species (single, dipole, triple, etc.) involved, which can be interpreted by the following equations:

$$D^{+}_{Average} = \sum_{i} x_i^{+} D_i^{+} \qquad (6.4)$$

$$D^{-}_{Average} = \sum_{i} x_i^{-} D_i^{-} \qquad (6.5)$$

where $D^{+}_{Average}$ and $D^{-}_{Average}$ are average cation and anion diffusion coefficients measured by NMR experiments. D_i^{+} and D_i^{-} correspond to the diffusion of individual ionic species that contain cations and/or anions, *e.g.*, single ions, dipoles, triple ions, etc. Similarly, x_i^{+} and x_i^{-} represent the mole fraction of each type of ionic cluster that contains cations and/or anions. We are working toward a quantitative aggregation model using these concepts, but we require more data and most likely molecular dynamics simulations as further inputs. To illustrate these concepts, Figure 6.8 depicts a simple model in which only four types of ionic species are considered: single, dipole, triple and quadrupole ions. According to this model, anionic triple ions dominate at low hydration and lead to more isolated (single) cations, resulting in enhanced cation diffusion. Dipoles and quadrupoles do not produce imbalanced average *D* ratios since cations and anions are symmetrically distributed, and cationic triple ions will be less likely to exist as they contribute negatively to the observed $D^{+}_{Average}$. In other words, we conclude that anionic aggregates with reduced diffusion are prevalent at low hydration, while the presence of more isolated cations results in faster cation diffusion on average.

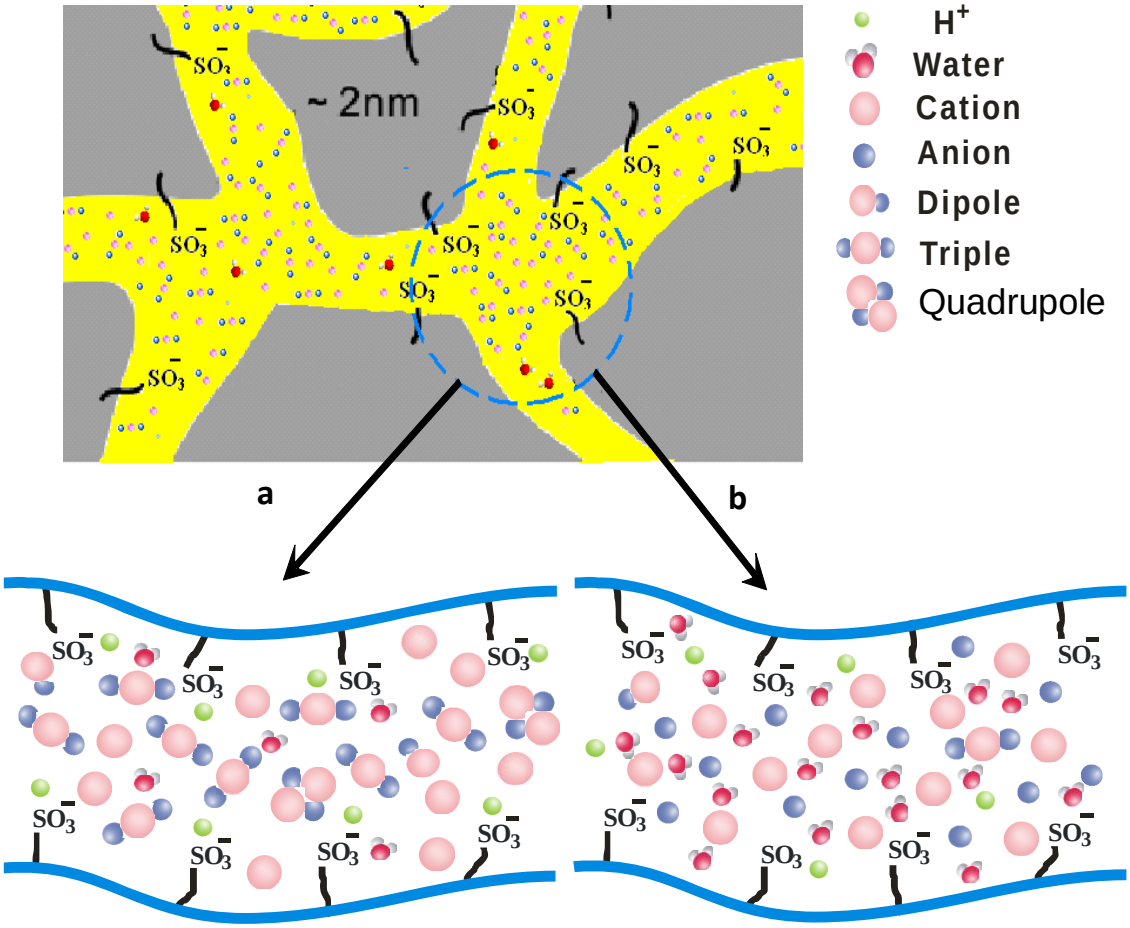

Figure 6.8. Ion associations of ILs inside Nafion membrane

Ion associations of ILs inside the ~ 2 nm hydrophilic channels of Nafion membrane. (a) Low water content. (b) High water content. At low water content (a), negatively charged triple ions are prevalent due to strong electrostatic attractions among charged species, leaving more isolated cations and resulting in enhanced cation diffusion on average. At high water content (b), water dramatically reduces electrostatic interactions among cations and anions and leads to ion disassociation. Anions (especially $[BF_4]^-$) are released from local electrostatic networks and move relatively freely, while sulfonate groups fixed to polymer side chains attract cations and thus slow their average translational motion.

While we have not revealed the fundamental molecular mechanisms driving formation of these anionic aggregates, recent bending tests on $[C_2mim][TfO]$ based ionic polymer actuators support our aggregation model. With applied DC voltage, the actuator bends toward the anode at short times, followed by reversed bending back toward the cathode at longer times and with greatly enhanced bending curvature.[37,38] This is consistent with 1) cations transporting quickly to accumulate at and swell the cathode, and 2) anionic aggregates transporting slowly to accumulate at the anode, and then resulting in increased swelling due to their larger size. Regarding specific intermolecular interactions, we emphasize that we do not observe significantly higher D_{cation}/D_{anion} for $[C_4mim]^+$ based ILs ($[C_4mim][TfO]$ or $[C_4mim][BF_4]$) at low water content χ_{water}. This further signifies that anionic aggregation caused by specific molecular packing strongly depends on the structural features of the cation. When comparing $[C_2mim]^+$ with $[C_4mim]^+$, factors such as shape anisotropy (*e.g.*, planar or rodlike structures), charge distribution and conformational flexibility (short alkyl chain of the $[C_2mim]^+$ vs. $[C_4mim]^+$ chain) should strongly impact and determine molecular packing among cations and anions. Finally, in correlation with practical mechanical actuator studies, these trends, in terms of ion transport, qualitatively correlate with empirical observations that $[C_2mim][TfO]$ and $[C_2mim][BF_4]$ appear to form the best performing IL-based polymer actuators.[6,39] If anions and cations conduct equally well in an ionomer membrane, electrolyte efficiency is greatly diminished, since anion conduction can cancel out cation conduction. This work provides further insight into the mechanism of ion conduction inside an ionomer membrane and may facilitate design of new types of ion containing polymers.

6.4 Conclusions

We have investigated cation and anion diffusion of four related ILs ([C_2mim][TfO],[C_2mim][BF_4], [C_4mim][TfO] and [C_4mim][BF_4]) both outside and inside Nafion membranes, and as a function of water content. With increasing hydration of free ILs, the ratio of cation to anion diffusion coefficients reverses, then plateaus to values consistent with expected hydrodynamic radii ratios for cations and anions (r_{cation}/r_{anion} = 1.4 for [C_2mim][BF_4] and 1.1 for [C_2mim][TfO]). When ILs are absorbed into an ionomer membrane, a drastically different ionic environment, associations are modulated by relative anion basicity (protonation) and drag from the fixed -SO_3^- anions lining the polymer's hydrophilic channels. Cations are substantially faster (up to 3X) at low water contents inside membranes and these observations may be explained by a simple aggregation model, indicating an excess of negatively charged triple ions. At high water contents, this trend reverses to give faster isolated anions (up to 4X), while cation transport is slowed by interactions with immobile SO_3^- anions. Investigating such cation/anion interactions provides insight into these complex fluids, and informs design strategies for IL electrolyte applications such as batteries and polymer-based "artificial muscle" mechanical actuators. We are working toward quantitative models to assess relative aggregate populations, as well as chemically specific measurements of E-field-driven ion motion.

References

[1] T. Welton, Room-temperature ionic liquids. Solvents for synthesis and catalysis, Chem. Rev., 99 (1999) 2071-2083.
[2] M. Armand, F. Endres, D.R. MacFarlane, H. Ohno, B. Scrosati, Ionic-liquid materials for the electrochemical challenges of the future, Nature Mater., 8 (2009) 621-629.
[3] F. Vidal, C. Plesse, D. Teyssie, C. Chevrot, Long-life air working conducting semi-IPN/ionic liquid based actuator, Synth. Met., 142 (2004) 287-291.
[4] M.D. Bennett, D.J. Leo, Ionic liquids as stable solvents for ionic polymer transducers, Sensor Actuat A-Phys., 115 (2004) 79-90.

[5] A.J. Duncan, D.J. Leo, T.E. Long, Beyond Nafion: Charged Macromolecules Tailored for Performance as Ionic Polymer Transducers, Macromolecules, 41 (2008) 7765-7775.
[6] S. Liu, W.J. Liu, Y. Liu, J.H. Lin, X. Zhou, M.J. Janik, R.H. Colby, Q.M. Zhang, Influence of imidazolium-based ionic liquids on the performance of ionic polymer conductor network composite actuators, Polym. Int., 59 (2010) 321-328.
[7] P.M. Bayley, G.H. Lane, N.M. Rocher, B.R. Clare, A.S. Best, D.R. MacFarlane, M. Forsyth, Transport properties of ionic liquid electrolytes with organic diluents, Phys.Chem.Chem.Phys., 11 (2009) 7202-7208.
[8] M.G. Del Popolo, C.L. Mullan, J.D. Holbrey, C. Hardacre, P. Ballone, Ion association in [bmim][PF6]/naphthalene mixtures: An experimental and computational study, J. Am. Chem. Soc., 130 (2008) 7032-7041.
[9] H. Tokuda, K. Hayamizu, K. Ishii, M.A.B.H. Susan, M. Watanabe, Physicochemical properties and structures of room temperature ionic liquids. 2. Variation of alkyl chain length in imidazolium cation, J. Phys. Chem. B, 109 (2005) 6103-6110.
[10] W. Zhao, F. Leroy, B. Heggen, S. Zahn, B. Kirchner, S. Balasubramanian, F. Muller-Plathe, Are There Stable Ion-Pairs in Room-Temperature Ionic Liquids? Molecular Dynamics Simulations of 1-n-Butyl-3-methylimidazolium Hexafluorophosphate, J. Am. Chem. Soc., 131 (2009) 15825-15833.
[11] H.V. Spohr, G.N. Patey, Structural and dynamical properties of ionic liquids: Competing influences of molecular properties, J. Chem. Phys., 132 (2010) .
[12] P.S. Pregosin, Ion pairing using PGSE diffusion methods, Prog. Nucl. Magn. Reson. Spectrosc., 49 (2006) 261-288.
[13] P. Stilbs, Fourier transform pulsed-gradient spin-echo studies of molecular diffusion, Prog. Nucl. Magn. Reson. Spectrosc., 19 (1987) 1-45.
[14] R. Katoh, M. Hara, S. Tsuzuki, Ion Pair Formation in [bmim]I Ionic Liquids, J. Phys. Chem. B, 112 (2008) 15426-15430.
[15] H. Weingaertner, Understanding ionic liquids at the molecular level: Facts, problems, and controversies, Angew. Chem. Int. Ed., 47 (2008) 654-670.
[16] J.T. Edward, Molecular Volumes and Stokes-Einstein Equation, J. Chem. Edu., 47 (1970) 261.
[17] R. Schiller, The Stokes-Einstein Law by Macroscopic Arguments, Int. J. Radiat. Appl. Instrum., Part C. Radiat. Phys. Chem. , 37 (2002) 549.
[18] H. Every, A.G. Bishop, M. Forsyth, D.R. MacFarlane, Ion diffusion in molten salt mixtures, Electrochim. Acta, 45 (2000) 1279-1284.
[19] K.J. Fraser, E.I. Izgorodina, M. Forsyth, J.L. Scott, D.R. MacFarlane, Liquids intermediate between "molecular" and "ionic" liquids: Liquid Ion Pairs?, Chem. Commun., (2007) 3817-3819.
[20] M.A. Susan, T. Kaneko, A. Noda, M. Watanabe, Ion gels prepared by in situ radical polymerization of vinyl monomers in an ionic liquid and their characterization as polymer electrolytes, J. Am. Chem. Soc., 127 (2005) 4976-4983.
[21] W. Xu, E.I. Cooper, C.A. Angell, Ionic liquids: Ion mobilities, glass temperatures, and fragilities, J. Phys. Chem. B, 107 (2003) 6170-6178.
[22] A. Noda, K. Hayamizu, M. Watanabe, Pulsed-gradient spin-echo H-1 and F-19 NMR ionic diffusion coefficient, viscosity, and ionic conductivity of non-chloroaluminate room-temperature ionic liquids, J. Phys. Chem. B, 105 (2001) 4603-4610.
[23] H.A. Every, A.G. Bishop, D.R. MacFarlane, G. Oradd, M. Forsyth, Transport properties in a family of dialkylimidazolium ionic liquids, Phys.Chem.Chem.Phys., 6 (2004) 1758-1765.

[24] T.D. Gierke, G.E. Munn, F.C. Wilson, The morphology in Nafion perfluorinated membrane products, as determined by wide-angle and small-angle X-ray studies, J. Polym. Sci., Part B: Polym. Phys., 19 (1981) 1687-1704.
[25] K. Schmidt-Rohr, Q. Chen, Parallel cylindrical water nanochannels in Nafion fuel-cell membranes, Nature Mater., 7 (2008) 75-83.
[26] J. Li, K.G. Wilmsmeyer, J.B. Hou, L.A. Madsen, The role of water in transport of ionic liquids in polymeric artificial muscle actuators, Soft Matter, 5 (2009) 2596-2602.
[27] J.B. Hou, J. Li, L.A. Madsen, Anisotropy and Transport in Poly(arylene ether sulfone) Hydrophilic-Hydrophobic Block Copolymers, Macromolecules, 43 (2010) 347-353.
[28] J. Hennig, A. Nauerth, H. Friedburg, Rare Imaging - a Fast Imaging Method for Clinical Mr, Magn. Reson. Med., 3 (1986) 823-833.
[29] J. Li, K.G. Wilmsmeyer, L.A. Madsen, Anisotropic Diffusion and Morphology in Perfluorosulfonate Ionomers Investigated by NMR, Macromolecules, 42 (2009) 255-262.
[30] J. Li, K.G. Wilmsmeyer, L.A. Madsen, Hydrophilic channel alignment modes in perfluorosulfonate ionomers: Implications for proton transport, Macromolecules, 41 (2008) 4555-4557.
[31] T. Koddermann, R. Ludwig, D. Paschek, On the validity of Stokes-Einstein and Stokes-Einstein-Debye relations in ionic liquids and ionic-liquid mixtures, Chem.Phys.Chem., 9 (2008) 1851-1858.
[32] Y.T. Wang, G.A. Voth, Unique spatial heterogeneity in ionic liquids, J. Am. Chem. Soc., 127 (2005) 12192-12193.
[33] D.R. MacFarlane, J.M. Pringle, K.M. Johansson, S.A. Forsyth, M. Forsyth, Lewis base ionic liquids, Chem. Commun., (2006) 1905-1917.
[34] D. Nama, P.G.A. Kumar, P.S. Pregosin, T.J. Geldbach, P.J. Dyson, ^{1}H-^{19}F HOESY and PGSE diffusion studies on ionic liquids: The effect of co-solvent on structure, Inorg. Chim. Acta, 359 (2006) 1907-1911.
[35] R.M. Fuoss, C.A. Kraus, Properties of Electrolytic Solutions. IV. The conductance minimum and the formation of triple ions due to the action of coulomb forces, J. Am. Chem. Soc., 55 (1933) 2387-2399.
[36] A.V. Dobrynin, M. Rubinstein, Theory of polyelectrolytes in solutions and at surfaces, Prog. Polym. Sci., 30 (2005) 1049-1118.
[37] S. Liu, R. Montazami, Y. Liu, V. Jain, M.R. Lin, J.R. Heflin, Q.M. Zhang, Layer-by-layer self-assembled conductor network composites in ionic polymer metal composite actuators with high strain response, Appl. Phys. Lett., 95 (2009) -.
[38] D. Wang, J.R. Heflin, Personal Communication, (2010).
[39] M.D. Bennett, D.J. Leo, G.L. Wilkes, F.L. Beyer, T.W. Pechar, A model of charge transport and electromechanical transduction in ionic liquid-swollen Nafion membranes, Polymer, 47 (2006) 6782-6796.

Chapter 7

Imaging the Ionic Nature and Local Fluctuations of Ionomers

7.1 Introduction

Innovative design and targeted synthesis represent a promising strategy for the creation of next generation functional materials for renewable energy and global sustainability. A critical step toward optimizing polymer synthesis is structural elucidation, including morphology, local anisotropy and domain structures, which fundamentally influence the performance of many useful polymeric materials. Nafion, a perflurosulfonate ionomer (PFSI), is the state of the art polymer electrolyte that covalently links tetrafluoroethylene backbones to short perfluorovinylether side chains terminated with sulfonate groups. Consequently, phase separation occurs on a microscopic level due to the difference in polarity between the fluorocarbon backbone and sulfonate groups. This delicate combination of polar and non-polar chemical moieties endow the material with novel conduction and mechanical properties. Thus, they find diverse applications in many fields, such as fuel cell membranes,[1] nanofiltration,[2] battery electrolytes[3] and soft mechanical actuators.[4] Previous studies[5-8] relied heavily on X-ray and neutron scatting methods to extract morphological information from these ionomers, followed by numerous models attempting to fit scattering data and explain the structural complexity and excellent transport properties.

Of the many models to date, Gierke's primitive cluster-network model[9] remains the most popular. In this model, ionic aggregates are conceptualized as spherical inverted micelle clusters that swell in the presence of polar solvent and percolate into a three dimensional network embedded within the polymer matrix. Other morphological models of these ionomers including

cylinders,[7] lamellae[8] and fibrillar bundles[5] have also been proposed. More recently, Schmidt-Rohr and coworkers re-examined X-ray data published in the literature and proposed a parallel cylindrical nanochannel model for Nafion based on their meticulous simulations.[7] This "new" model is featured by the presence of elongated cylindrical hydrophilic nanochannels, which are randomly packed in the polymer matrix. Recent NMR proton diffusion[10] studies also signified the presence of sub-micron domain structures in PFSI materials as confirmed by the restricted diffusion phenomenon.

One of the main objectives in this dissertation is to present the NMR experimental strategy and analytical protocols to correlate transport properties with the structural specificity of ionomers. Following our work in chapter 6, we employ pulsed field gradient (PFG) NMR,[11-13] using high magnetic field gradients to study slow ion diffusion, and coupled that with quantitative data analysis to understand the impact of ion density variation and thermal fluctuation on ion transport inside ionomers. Our strategy relies on using ionic liquids (ILs) to probe multiple length scales within these materials by tracing the time dependent behavior of ion diffusion. ILs are ideal candidates for this purpose for the following reasons: (1) Their relatively high viscosity and dense ion packing (ionic aggregates) result in much slower ion diffusion inside ionomers, compared to traditional solvents (water, methanol), thereby offering probes that are more sensitive to local restrictions at shorter length scales. (2) The chemical selectivity of NMR spectroscopy allows for accurate measurements of cation and anion diffusion separately, the results of which complement each other and can yield more comprehensive information with regard to the local environment within the ionic channels and domains. (3) Varying the diffusion time to probe a wide range of length scale information is practical given the fact that NMR relaxation times are moderate (both T_1 and T_2) for both cations and anions in the chosen ILs.

Here, we report systematic cation and anion diffusion studies at varying temperatures, hydration levels and IL uptakes. In contrast to the published water diffusion data,[10] our measured cation diffusion does not show dependence on diffusion time, which suggests the absence of domain boundaries on a submicron scale. More strikingly, we observe various levels of anomalous anion diffusion, where the average displacement of anions remains unchanged after diffusion time increases above particular values. This unique feature provides solid evidence to demonstrate that anion motions are confined within a distribution of specific local structures that are characterized by the anomalous (NMR) diffusion decay curves. We quantitatively determine the size and distribution of these local structures by analyzing the restricted molecular motions inside polydisperse pores. We further show that these local structures (size and distribution) are ion selective and non-static in nature, as they exhibit high sensitivity to temperature, water content and IL uptake. We attribute the origin of these structures to an inhomogeneous distribution of local electrical potentials due to the density variation of negatively charged sulfonate groups on the polymer side chain. For the first time, we have shown a useful way to successfully "image" ionomers by virtue of the NMR approach and highlight the critical role of ion density and local fluctuations in the process of ion transport.

7.2 Theory and Experimental

7.2.1 Diffusion in Confined Pores

PFG NMR utilizes magnetic field gradients to relate signal attenuation to molecular self-diffusion coefficient and other relevant experimental parameters. For free diffusion, the Stejeskal-Tanner equation applies[14]:

$$I = I_0 \exp(-D\gamma^2\delta^2 g^2 (\Delta - \frac{\delta}{3})) \qquad (7.1)$$

where γ is the gyromagnetic ratio, g is the gradient pulse strength, δ is the effective duration of the gradient pulse and *D* is the self-diffusion coefficient. For diffusion confined within isolated (confined) and monodispersed pores (R is the pore size), if $D\Delta \gg R^2$, equation (7.1) becomes[15]:

$$I = I_0 \exp(-\frac{\gamma^2\delta^2 g^2 R^2}{5}) \qquad (7.2)$$

If the pore size follows a certain distribution, (assuming a Gaussian distribution), then equation (7.2) evolves into:

$$I = I_0 \int_0^{+\infty} P(R) \exp\left(-\frac{\gamma^2\delta^2 g^2 R^2}{5}\right) dR \quad (7.3)$$

$$P(R) = \frac{1}{\sqrt{\pi}\sigma} \exp\left(-\frac{(R - R_0)^2}{\sigma^2}\right) \qquad (7.4)$$

where R_0 and σ denote the mean value and standard deviation of the pore size, respectively. Plug equation (7.4) into (7.3), one obtains that[16]

$$I = I_0 \frac{1}{\sqrt{1 + \frac{\gamma^2\delta^2 g^2 \sigma^2}{5}}} \exp\left(-\frac{\gamma^2\delta^2 g^2 R_0^2}{5 + \gamma^2\delta^2 g^2 \sigma^2}\right) \qquad (7.5)$$

In comparison to equation 7.1, equation 7.5 deviates from the normal Gaussian decay and its curvature is governed by both R_0 and σ. This provides an unique way of "imaging" the pore size and distribution. A computer program written in Matlab, which allows varying R_0 and σ individually, is applied to best fit the diffusion data using equation 7.5. The error bar for data fitting is < 5%.

7.2.2 Ionic Liquids and Ionomers

1-ethyl-3-methyl imidazolium trifluoromethanesulfonate ([C_2mim][TfO]), 1-butyl-3-methyl imidazolium trifluoromethanesulfonate ([C_4mim][TfO]) and 1-ethyl-3-methyl

imidazolium tetrafluoroborate ([C_2mim][BF_4]) were used to study ion transport inside ionomers. All these ILs were obtained from Solvent Innovation GMBH (Cologne, Germany) with purity >99% and preserved in a desiccator to avoid further water adsorption. Extruded Nafion 117 (N117) membranes with equivalent weight of 1100 (grams of dry membrane per mole of sulfonate groups), were purchased from E.I. Dupont in the acid form with the thickness of 175 μm. Membranes were cut into pieces of 5 mm x 5 mm in size, stacked together to a total mass of ~60 mg and dried in a vacuum oven for 12h at room temperature to determine the dry membrane mass ($mass_{dry}$) gravimetrically. The samples were then soaked with ILs at 60-90^{o}C for 8-10 hours to achieve different IL uptakes. The wet membranes were blotted to remove surface liquid and then dried in the vacuum oven for >24h at room temperature to determine ILs content ($mass_{IL}$) inside membranes. The dry membranes stack were then wrapped with a piece of plastic film and quickly transferred into our home built sealed Teflon cell to equilibrate for later diffusion measurement as reported earlier. Such a protocol effectively prevents water absorption into membranes. Diffusion measurement was performed as temperature increased from 30^{o}C to 65^{o}C, with 2 hours of sample equilibration at each temperature prior to any experiment. Due to its negligible vapor pressure, IL in the membranes ($mass_{IL}$) remained constant even at elevated temperatures, which was verified via checking the mass of dry membranes afterwards. No obvious changes in sample mass also signified insignificant water adsorption during diffusion measurements. IL uptake was calculated using equation (7.6):

$$\text{IL uptake} = \frac{\text{mass}_{\text{IL}} - \text{mass}_{\text{dry}}}{\text{mass}_{\text{dry}}} \times 100\% \qquad (7.6)$$

7.2.3 High Gradient Calibration and Ion Diffusion by PFG NMR

We employ ^{1}H and ^{19}F NMR to study cation and anion diffusion separately using the PGSTE sequence on a Bruker Avance III WB 400 MHz (9.4 T) NMR spectrometer, equipped with a 8 mm single resonance ^{1}H RF coil and a single axis gradient probe. The gradient probe has a maximum gradient of 30 T m^{-1} along the magnetic field direction, which allows measuring relatively slow diffusion coefficient (~ 10^{-14}-10^{-15} m^2/s). As mentioned in chapter 3, we optimize the gradient pre-emphasis, select appropriate range of gradient pulse duration (δ) and gradient delay time to minimize eddy current effect at high gradients, the presence of which will result in phase distortions or fast signal decay. Using the dry glycerol sample, we observe no variation in measured diffusion coefficient as a function of gradient pulse duration (δ), diffusion time (Δ) (when $\delta \geq 1.5$ ms, $\Delta \geq 20$ ms and $g_{max} \leq 1800$ G/cm) and no deviation from linear regression as well, which all confirm the stability and reliability of our gradient system. The PGSTE sequence used a $\pi/2$ pulse time of 6.4 μs for ^{1}H and 8 μs for ^{19}F, effective gradient pulse durations δ ranging from 2.0 – 3.0 ms, and diffusion times Δ ranging from 20 – 2000 ms, depending on the limit of relaxation time, which changes as a function of IL uptake and measured temperatures. 10-16 gradient steps with appropriate selection of maximum gradient strength resulted in > 90% NMR signal attenuation. Due to the differences in signal to noise ratio (SNR), the number of scans varied from 4 to 1000 to produce sufficient signal-to-noise ratio for each data point.

7.3 Results and Discussion

7.3.1 Impact of Temperature on Ion Transport

We first examine the temperature effect on ion diffusion inside ionomer membranes and focus on the "dry" membranes soaked with 28wt% [C_2mim][TfO] IL. Here, the term "dry" refers

to the membrane sample dried under vacuum at room temperature (25 ^{o}C). We define the water content using the conventional label λ, which equals the number of water molecules per sulfonate group ($\lambda = \frac{n(H_2O)}{n(SO_3^-)}$) and λ=0 for dry membranes. Figure 7.1 shows the ^{1}H and ^{19}F spectra for the dry membrane at different temperatures. In general, the line width becomes narrower at elevated temperatures due to the enhanced molecular tumbling. Though the drying process may still leave some residual water inside the membrane, there is no evident $^{1}H_2O$ peak in all the ^{1}H spectra and the peak integrals also show quantitative agreement with the chemical structure of the cation.

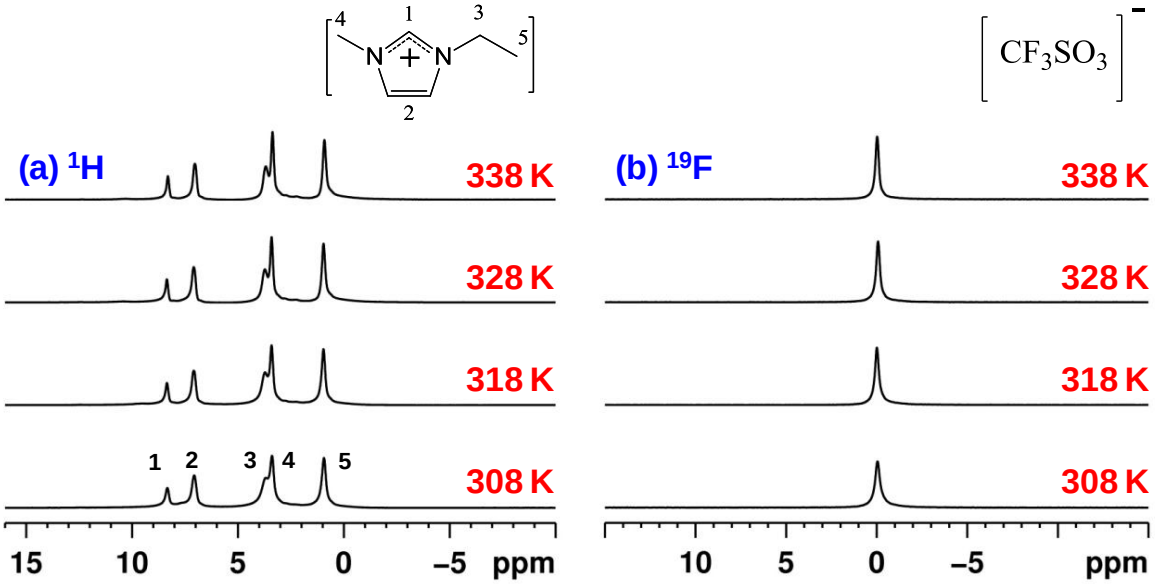

Figure 7.1. ^{1}H and ^{19}F spectra of IL inside dry Nafion membranes vs. temperature

(a) ^{1}H and (b) ^{19}F spectra for 28wt%[C_2mim][TfO] IL inside dry Nafion membranes (λ =0) at different temperatures. Different proton peaks are assigned by numbers. The line width decreases with temperatures and there is no observable water peak in all the ^{1}H spectra.

We compare cation and anion diffusion results by plotting the logarithm of signal intensity vs. the Stejskal-Tanner parameter ($\gamma^2 g^2 \delta^2(\Delta - \delta/3)$) as shown in figure 7.2. For non-

restricted diffusion, the plot should yield a linear regression. The absolute value of the slope equals the diffusion coefficient, which should be independent of the diffusion time Δ. For the restricted (or anomalous) diffusion, the slope may vary with Δ and the plot may deviate from the linear regression. Strikingly, we observe dramatic difference between cation and anion diffusion, especially at long Δ. For the [C_2mim] cation, we consistently obtain non-restricted diffusion at different temperatures. In contrast, the [TfO] anion only shows non-restricted diffusion at short Δ but restricted diffusion at long Δ, as manifested by the anomalous decay curves. The curvature degree also increases with Δ. One may notice that cations diffuse approximately 3X faster as compared with the non-restricted anion diffusion at short Δ (Δ < 200 ms). Such a phenomenon is consistent with our previous observation regarding cation/anion diffusion ratio at low water content. However, we did not observe the anomalous signal decay at long Δ in our previous study because the signal intensity only attenuated by 50% at maximum due to the limit in gradient strength (<300 G/cm) and transverse relaxation time (T_2 < 10 ms). For the restricted anion diffusion, a more straightforward explanation is likely to associate with the physical barrier (structural heterogeneity) that impacts the anion diffusion at long Δ and such an effect tends to be less evident for short diffusion length (short Δ). However, this explanation presents an obvious contradiction to our observed non-restricted cation diffusion, given the fact that cations and anions associate and reside in the same environment. Additionally, cations should exhibit more evident restricted diffusion at short Δ since they diffuse much faster than anions. Consequently, two serious questions arise: (1) What is the mechanism behind that drives the anomalous anion diffusion? (2) Why cation and anion diffusion behaviors are dramatically different inside ionomer membranes?

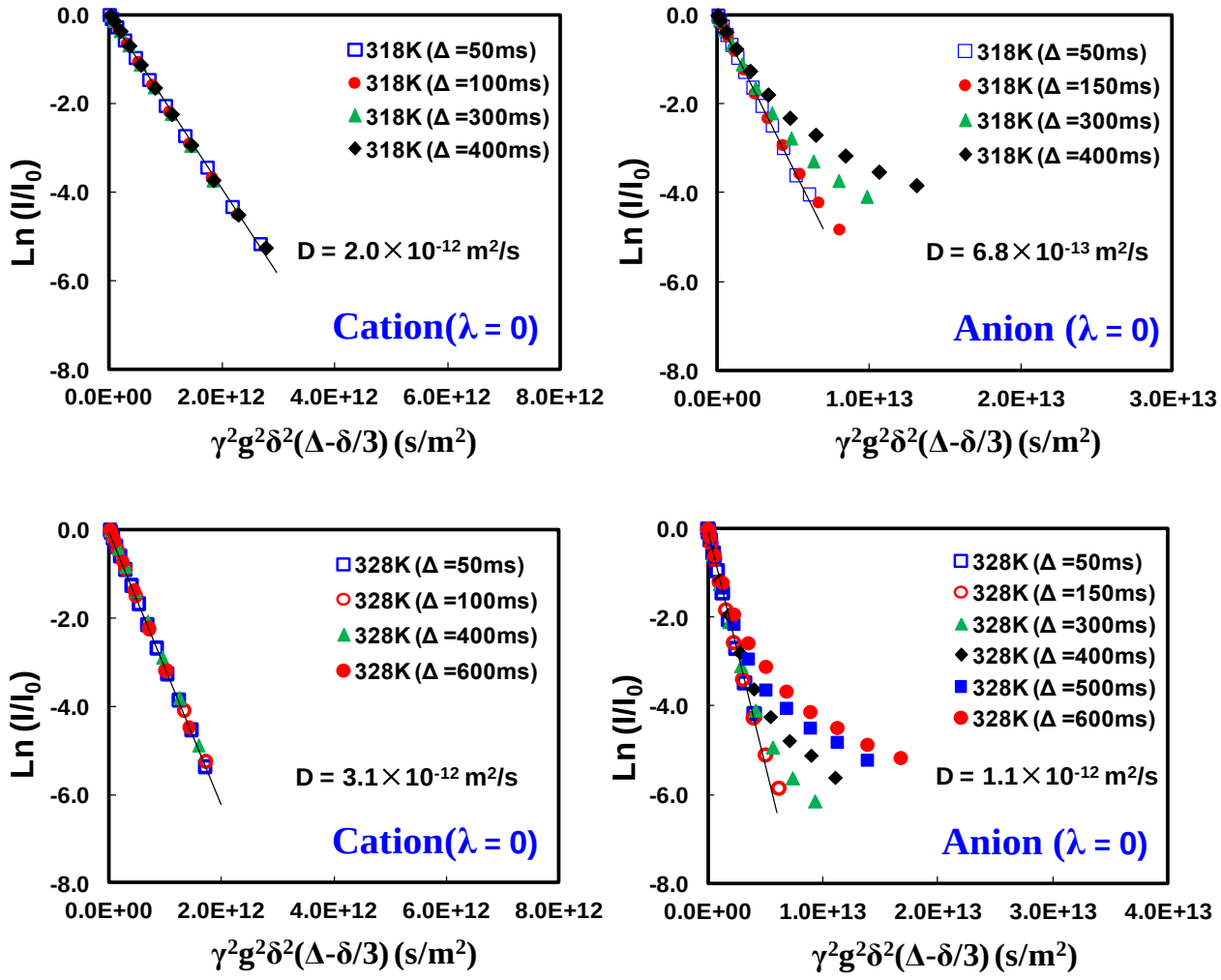

Figure 7.2. Stejskal-Tanner plot for ion diffusion inside dry membranes

Representative plot of signal decay vs. the Stejskal-Tanner parameter for the 28wt% [C_2mim][TfO] IL inside dry membranes at two different temperatures. For cation diffusion, all data points consistently overlap and show linear regression, the negative slope of which equals the measured diffusion coefficient. For anion diffusion, the signal attenuation yields linear regression at short Δ but anomalous decay curves when Δ is longer, which characterize the local restriction to anion diffusion.

To address question (1), several other possibilities might explain our observed anomalous anion diffusion, such as the distribution of diffusion coefficients,[17] chemical exchange effect,[18]

orientation of local domain structures,[19] etc. However, a detailed examination indicates that none of these explanations could rationalize the experimental observations. If one attributes the anomalous signal decay to the distribution of diffusion coefficients, one should also observe the same phenomenon at short Δ. If one considers the chemical exchange effect as the origin, the plot curvature should become less evident as Δ increases, which is opposite to our observations. If the anomalous anion diffusion is due to the orientation of local domain structures, the size of which is comparable with the diffusion length at long Δ, then a similar curvature should also appear at short Δ, which is not observed experimentally. Beyond these arguments, any rational explanation must satisfy two conditions: anion diffusion is free at short Δ and restricted at long Δ.

Considering the fact that NMR diffusion experiments determine the molecular diffusion coefficient by measuring the mean square displacement ($<Z^2>$) of molecular ensembles during Δ, we plot Ln (I/I_0) vs. $\gamma^2g^2\delta^2$ to understand how $<Z^2>$ scales with Δ as shown in figure 7.3. For the non-restricted cation diffusion at each temperature, $<Z^2> = 2D\Delta$ and $<Z^2>$ increases monotonically with Δ as expected. However, for anion diffusion at a given temperature, an interesting phenomenon emerges: the data plot overlaps when Δ is long enough, indicating that $<Z^2>$ remains constant with respect to Δ. The situation is equivalent to molecular diffusion in isolated pores, where the molecular diffusion is completely confined in the pores by impermeable walls. Such an experimental phenomenon provides solid evidence to demonstrate that anion motions are confined within specific local structures. For simplification, we consider these confinement structures as isotropic "closed" pores (spherical shape). If these pore structures are monodispersed, figure 7.3 should still yield a linear regression as governed by equation 7.2. Thus, the decay curvature in figure 7.3 further suggests the pore structures have a

certain size distribution. The statistical value $<Z^2>$ of molecular motions therefore reflects both the average pore size and distribution. Consequently, the NMR diffusion measurement offers a special way to image the local confinement structures by virtue of measuring molecular self-diffusion coefficient.

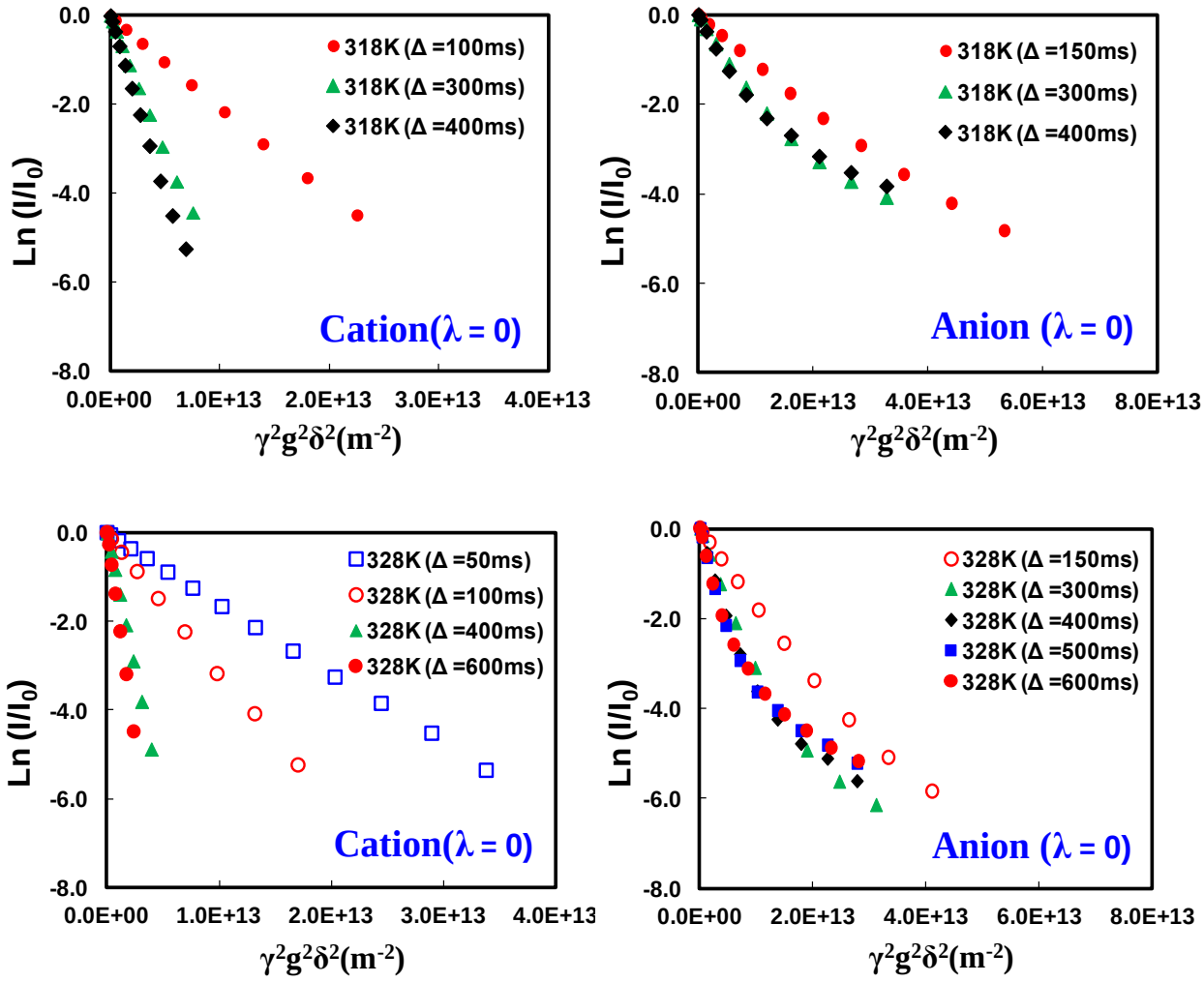

Figure 7.3. Plot of mean square displacement for ion diffusion inside dry membranes

Signal decay vs. $\gamma^2\delta^2g^2$ for ion diffusion inside dry membranes (λ=0) at two different temperatures. The slope of each curve equals the mean square displacement ($<R^2>$) sampled by

ion diffusion, which increases monotonically with Δ for the cation but stays constant for the anion at long Δ values.

We further compare $<Z^2>$ of anions among different temperatures using long Δ values to examine the impact of temperatures on the confinement pore size and distribution. We set Δ sufficiently long so that the signal decay becomes independent of Δ. If the confined anion diffusion is due to the presence of static physical barriers associated with the ionomer structures, such as impermeable domain boundaries, the $<Z^2>$ value, which couples to the pore size and distribution, should not exhibit large variations within a certain temperature range. In other words, the confinement structures should not expand/shrink much upon temperature variations. Surprisingly, the plot curvature varies significantly with temperatures as shown by different colored dots in figure 7.4a. For a quantitative analysis, we assume the pore size follows the Gaussian distribution and employ equation 7.5 to fit the experimental data to derive the average pore size and distribution at each temperature. The good fitting results shown in figure 7.4a, on the other hand, support our assumption regarding the Gaussian distribution. Figure 7.4b represents the fitting results by plotting the probability density function vs. pore size R. The horizontal coordinate of individual peak corresponds to the mean value of the pore size R_0 at each temperature. The full width at half maximum (FWHM) for each peak is proportional to the pore size distribution, σ. In consistency with figure 7.4a, R_0 increases as 0.64, 1.17, 1.78 and 2.48 μm and σ increases as 0.35, 0.5, 0.72 and 0.98 μm. In comparison of the fitting results between 308 K (35^{o}C) and 318 K (45^{o}C), we notice that R_0 increases by >80% even though the temperature merely increases by 10 K. A similar effect also holds for the other temperatures. These results demonstrate the non-static nature of those "closed" pore structures, which tend to "interconnect" with each other and merge into larger pores at high temperatures. This also sheds

light into the puzzle of question (2), where an obvious contradiction exists between cation and anion diffusion in response to the local restriction. If the confinement effect (local restriction) truly originates from the physical boundaries associated with the polymer structures, one should also expect to observe anomalous cation diffusion since both ions diffuse in the same phase and it is thermal dynamically impossible to separate them on a large scale. This further informs us that these non-static pores selectively transport cations over anions, the property of which likely originates from the anionic nature (SO_3^- groups) of the polymer.

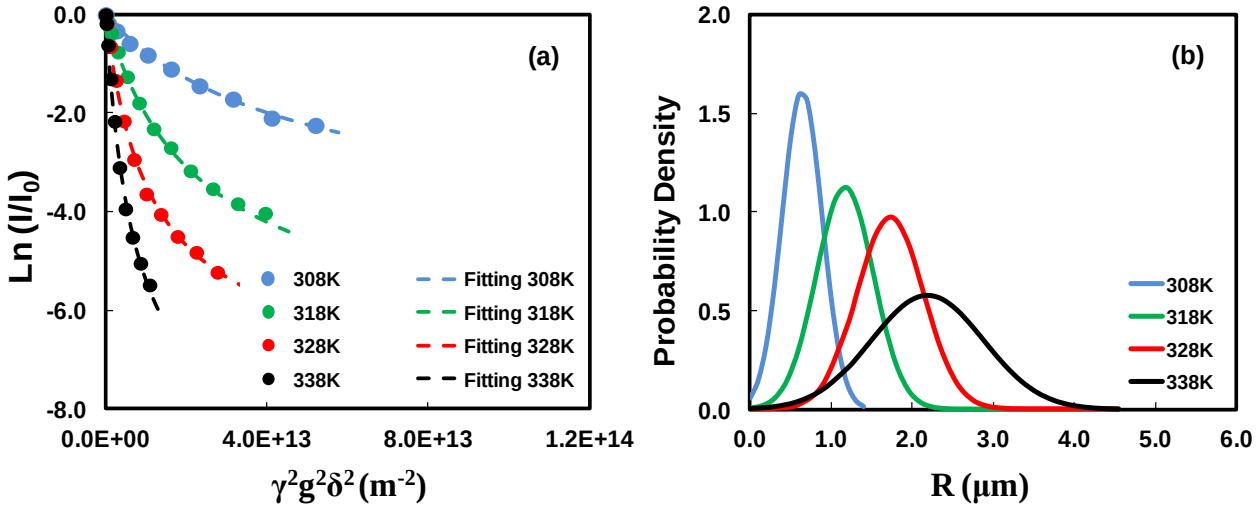

Figure 7.4. Determine the size and distribution of the confinement structure

Fitting experimental data (color dots) using equation (7.5) to estimate the mean value of pore sizes and distribution at various temperatures. (b) Representation of the derived pore sizes and distributions from (a). The mean value of pore size increases by a factor of 4 as the temperature changes from 308 K to 338 K.

7.3.2 Impact of IL Type and Uptake on Ion Transport

We then change the type of ILs and uptakes to examine their impact on cation and anion diffusion. In all cases, cation diffusion is normal and the results are not shown. For the anion

diffusion, figure 7.5a compares $<Z^2>$ of anions for two types of ILs inside dry membranes at different uptakes. The confined anion diffusion occurs in all cases regardless of the cation type. The plot curvature also increases with IL uptake, which indicates an increase in the confinement structural size as shown in figure 7.5b. Increase IL uptake is similar to the temperature effect as discussed in 7.1. We also observe a similar phenomenon when switching to the BF_4^- (results not shown). The experimental observations above further suggest that the "confined" ion diffusion is unique to anions inside these ionomer membranes.

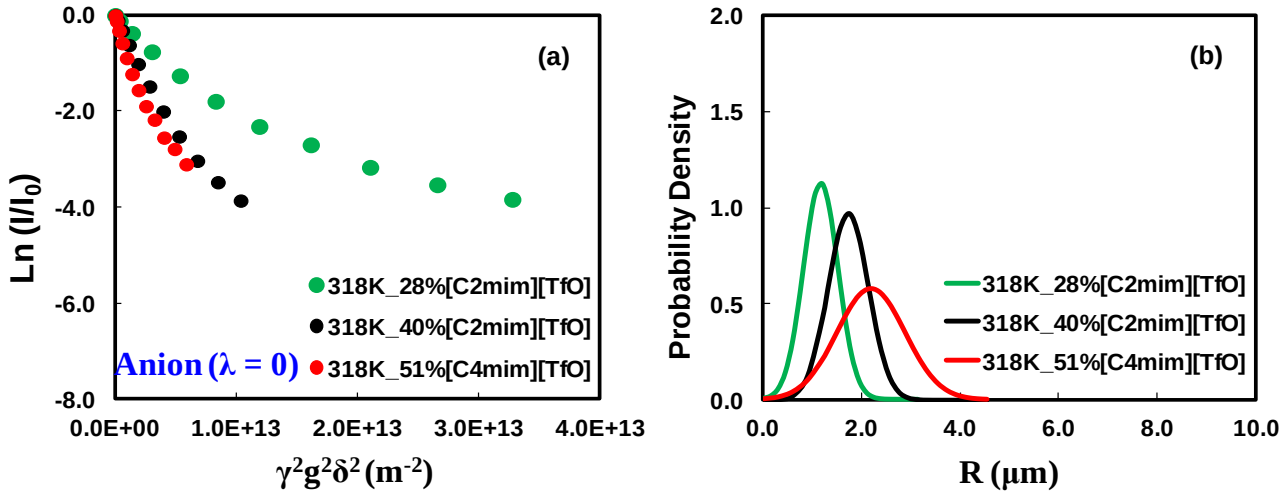

Figure 7.5. Confinement effect vs. IL uptakes and type

(a) Confined anion diffusion vs. IL uptake and type. (b) Changes in the confined pore sizes and distribution due to the variation of IL uptakes.

7.3.3 Impact of Hydration on Ion Transport

To further demonstrate the non-static nature and ion selectivity of these confinement structures, we examine the hydration effect on confined anion diffusion and compare the result with the dry membranes. The idea here is simple: water can strongly screen off the electrostatic interactions (attraction or repulsion) among different ions because of its high dielectric constant,

thereby releasing anions from the local confinement. Thus, even a small amount of water (1-2wt%) is likely to result in a significant dilation of the confinement structures if these structures are ionic in nature. After 24 hours of exposure in the open air, the 28wt% [C_2mim][TfO] dry membranes absorb 2.5wt% water. This process does not change the net IL uptake as confirmed later by the gravimetric measurement. For illustration, figure 7.6a compares the proton spectra of [C_2mim] cation inside dry membranes (bottom) and slightly wet membranes (top). The water peak is marked by the red arrow with its content labeled aside. The line width becomes narrower with enhanced intensity after the water absorption, a phenomenon similar to the temperature effect shown in figure 7.1. Figure 7.6b plots Ln (I/I_0) vs. $\gamma^2g^2\delta^2(\Delta-\delta/3)$ for anion diffusion inside the wet membranes. Similar to the results in figure 7.2, diffusion only becomes restricted at long Δ. However, the diffusion coefficient at short Δ values increases by 5X for the wet membranes as compared to the dry membranes, regardless of the lower temperature in figure 7.6b. For long Δ values, the plot curvature appears when Δ > 200 ms for the dry membranes but only becomes evident if Δ exceeds 1000 ms for the wet membranes. This clearly manifests the critical role of water on decreasing of local restrictions to anion diffusion.

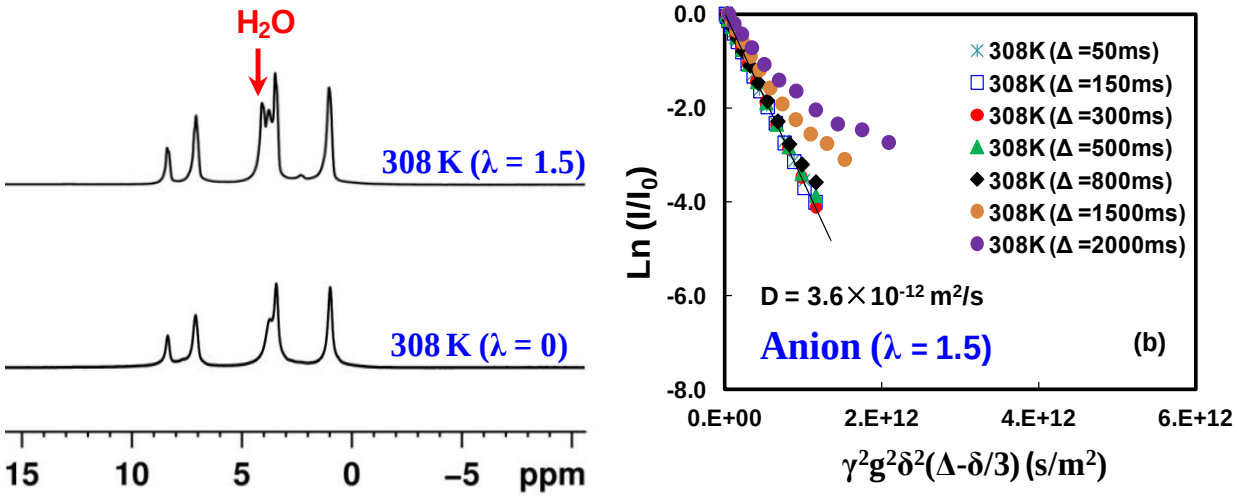

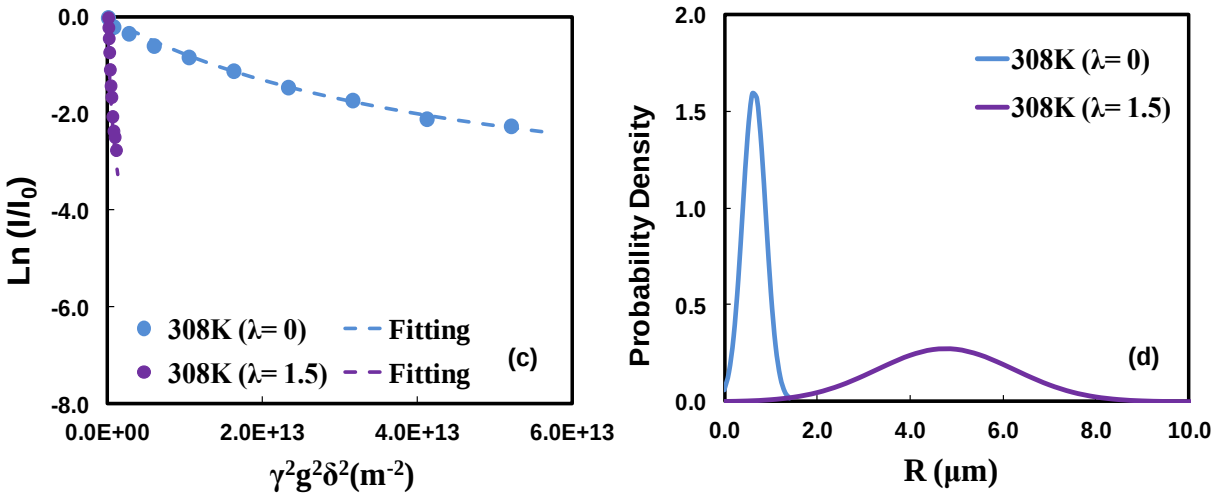

Figure 7.6. Confinement effect vs. hydration levels

(a) Comparison of the proton spectra in the presence (top) /absence (bottom) of water. (b) Plot of the signal intensity (logarithmic scale) vs. the Stejskal-Tanner parameter for anion diffusion at λ =1.5 (2.4 wt% of water). (c) Comparison of the fitting results for confined anion diffusion inside dry membranes vs. slightly "wet" membranes. (d) The dramatic change in fitted pore size and distribution as a consequence of hydration effect.

Figure 7.6c and 7.6d compare the fitting results of pore sizes and distributions between dry and wet membranes using equation 7.5. As we expect, adding water results in a substantial increase of the confinement pore sizes. The average pore size R_0 and distribution σ shift from 0.64 to 4.77 μm and 0.35 to 2.10 μm, respectively. Such a dramatic change in R_0 and σ is not due to the swelling of domain structures by water since the water uptake is too small (2.4 wt%) to cause any large variation in the structural size. This argument is further supported by the results in figure 7.5. Though the [C_2mim][TfO] IL uptake increases from 28 wt% to 40 wt%, the confinement pore size only increases by < 50%. Since the IL has a lower dielectric constant[20] than water, the confinement effect will persist even at high IL uptakes (>50%). Moreover, the

confinement effect is likely to disappear if the water uptake is to further increase. These observations therefore corroborate the fact that these pores structures are both ionic and non-static in nature.

Combining the fact that these confinement structures vary with temperatures and they are charged in nature and selectively transport ions, we conclude that the spatial organization of SO_3^- groups defines a particular type of "ionic domain structure"– a distribution of local electrical potentials, which are modulated by thermal fluctuations and local ionic medium. This "ionic domain structure" in essence corresponds to a density variation of SO_3^- groups from ~10 nm to a few μm that form numerous local spots with various SO_3^- concentrations, thereby delineating a set of "domain boundaries". Figure 7.7 schematically illustrates such a density variation at multiple length scales. Different colors represent various levels of local potentials (energy barriers) that increase with SO_3^- density. These local potentials are repulsive to anion motions but allow the cation transport. This may be somehow counterintuitive since cations are electrostatically dragged by SO_3^- groups. In fact, cation transport by associating with the fixed SO_3^- groups is viable since the energy required to disassociate one cation with one SO_3^- group while associating the cation with another nearby SO_3^- group is zero. Thus, this process involves no energy barriers and is thermodynamically possible. For anion transport, the confinement effect decreases with temperatures because of the increased randomization of SO_3^- groups at high temperatures, thereby reducing the effective strength of local electrical potentials as shown in figure 7.7 C. In other words, the anionic molecular probes will not sense the presence of "domain boundaries" if the thermal fluctuations can overcome these local energy barriers at a given temperature. Consequently, the local energy barrier becomes less evident with temperatures and some "domain boundaries" (green dots) disappear to exhibit a homogeneous material at larger

length scales. Such a concept is further illustrated in figure 7.8. This study of anomalous anion diffusion inside ionomers provides new insights into local dynamics and presents a new pathway to understand the “ionic” nature of these ionomers.

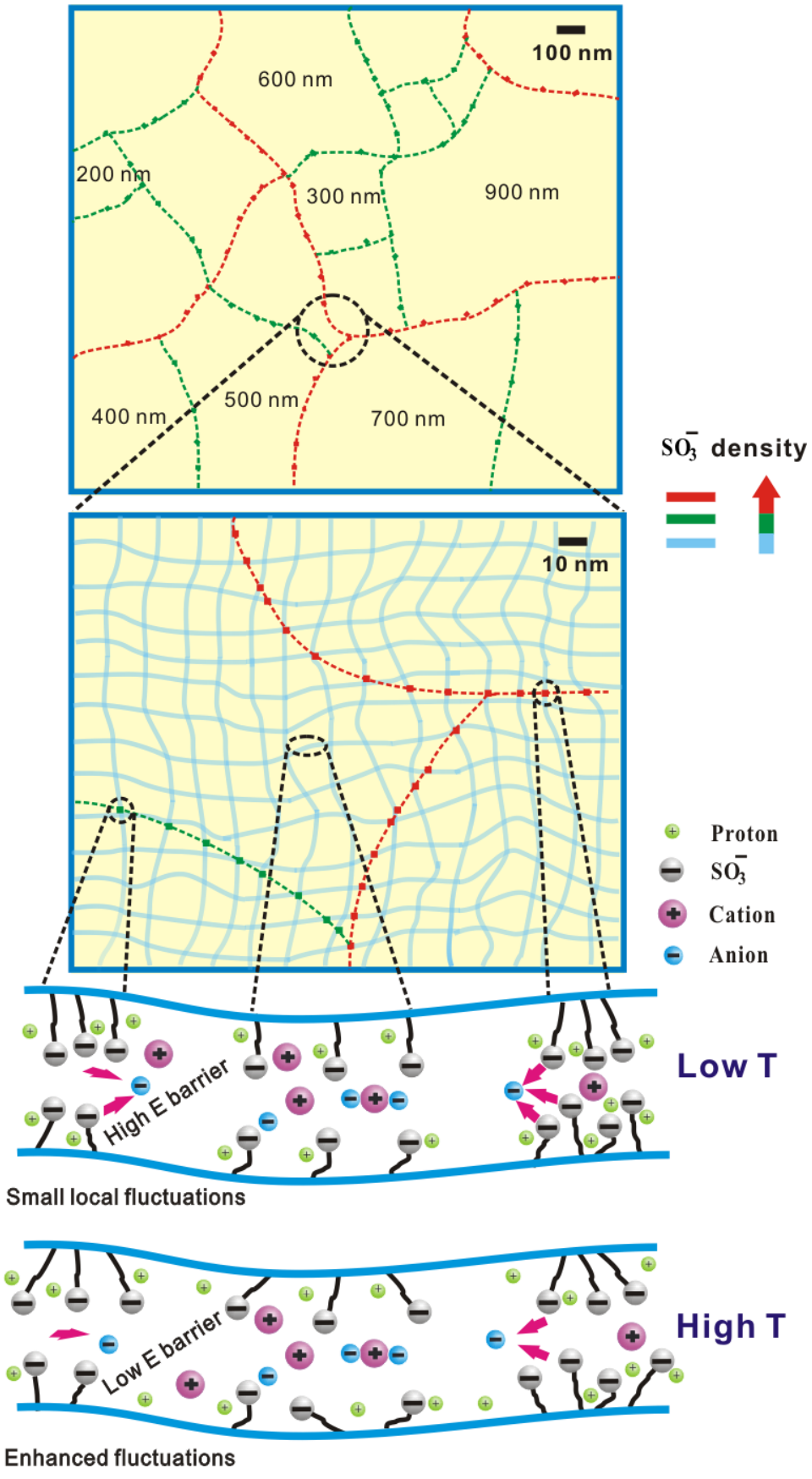
100 nm
600 nm
200 nm
300 nm
900 nm
400 nm
500 nm
700 nm
SO3 density
10 nm
Proton
SO3
Cation
Anion
High E barrier
Low T
Small local fluctuations
Low E barrier
High T
Enhanced fluctuations

Figure 7.7. Density variation of sulfonate groups at multiple length scales

Different colors represent different levels of SO_3^- group density, as denoted by the arrow. The high density ion regions (green and red) appear as local restrictions that block anion motions. At low temperatures or in the absence of high dielectric media, local restrictions are stronger than thermal fluctuations and anion motions are confined within a small dimension. At high temperatures or in the presence of high dielectric media, some local restrictions (green parts) "disappear" because of enhanced local fluctuations or reduced ionic interactions.

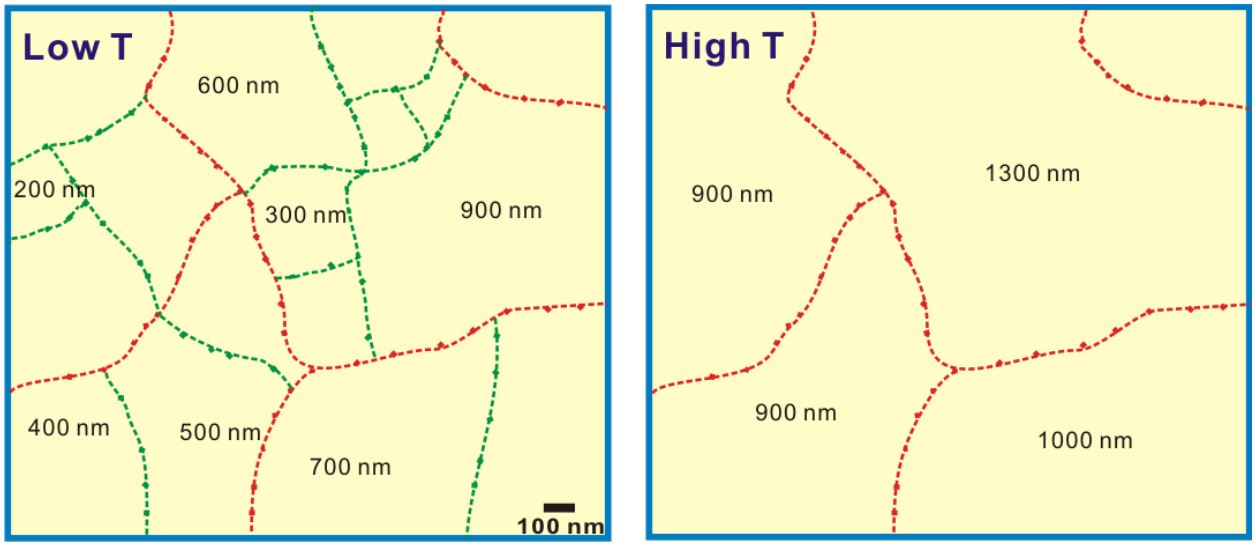

Figure 7.8. Impact of temperature on the ionic domain structure

Local domain boundaries (green and red parts) depend on temperatures. As temperature increases, some local domain boundaries (green parts) disappear due to enhanced local fluctuations, followed by the formation of larger domain structures.

7.4 Conclusion

We have successfully employed the strategy of "double probes" to investigate the structural feature of ionomer membranes via observing cation and anion diffusion inside the materials. Our

measured cation diffusion is normal regardless of IL types, uptakes, temperatures and hydration levels. In contrast, we observe strongly restricted anion diffusion in the absence of water, which results in anomalous NMR signal attenuation and the decay curve becomes independent of Δ when Δ is adequately long. This unique feature confirms the presence of local restrictions that confined anion motions. We further observe that the confinement structures dramatically vary with temperatures and water contents. These observations confirm these confinement structures are non-static and ionic in nature. Combining all these experimental evidence, we attribute the origin of these confinement structures to the inhomogeneous distribution of SO_3^- groups within the polymer matrix. Such a density variation of SO_3^- groups defines a many different levels of local electrical potentials, which are modulated by thermal fluctuations and ionic media. These slow ion diffusion studies present new avenues toward understanding the local dynamics and ionic structures to facilitate new materials design and fabrication.

References

[1] S.M. Javaid Zaidi, T. Matsuura, Polymer membranes for fuel cells, (2009).
[2] R.J. Petersen, Composite reverse-osmosis and nanofiltration membranes, J. Membr. Sci., 83 (1993) 81-150.
[3] M.K. Wang, F. Zhao, S.J. Dong, A single ionic conductor based on Nafion and its electrochemical properties used as lithium polymer electrolyte, J. Phys. Chem. B, 108 (2004) 1365-1370.
[4] M.D. Bennett, D.J. Leo, Ionic liquids as stable solvents for ionic polymer transducers, Sensor Actuat A-Phys., 115 (2004) 79-90.
[5] L. Rubatat, A.L. Rollet, G. Gebel, O. Diat, Evidence of elongated polymeric aggregates in Nafion, Macromolecules, 35 (2002) 4050-4055.
[6] A.L. Rollet, O. Diat, G. Gebel, A new insight into Nafion structure, J. Phys. Chem. B, 106 (2002) 3033-3036.
[7] K. Schmidt-Rohr, Q. Chen, Parallel cylindrical water nanochannels in Nafion fuel-cell membranes, Nature Mater., 7 (2008) 75-83.
[8] J.A. Dura, V.S. Murthi, M. Hartman, S.K. Satija, C.F. Majkrzak, Multilamellar interface structures in Nafion, Macromolecules, 42 (2009) 4769-4774.
[9] T.D. Gierke, G.E. Munn, F.C. Wilson, The morphology in Nafion perfluorinated membrane products, as determined by wide-angle and small-angle X-ray studies, J. Polym. Sci., Part B: Polym. Phys., 19 (1981) 1687-1704.

[10] T. Ohkubo, K. Kidena, A. Ohira, Determination of a micron-scale restricted structure in a perfluorinated membrane from time-dependent self-diffusion measurements, Macromolecules, 41 (2008) 8688-8693.
[11] E.O. Stejskal, J.E. Tanner, Spin diffusion measurements: spin echoes in the presence of a time-dependent field gradient, J. Chem. Phys., 42 (1965) 288-292.
[12] P.S. Pregosin, Ion pairing using PGSE diffusion methods, Prog. Nucl. Magn. Reson. Spectrosc., 49 (2006) 261-288.
[13] J.B. Hou, Z.Y. Zhang, L.A. Madsen, Cation/Anion associations in ionic liquids modulated by hydration and ionic Medium, J. Phys. Chem. B, 115 (2011) 4576-4582.
[14] E.O. Stejskal, J.E. Tanner, Spin diffusion measurements: spin echos in the presence of a time-dependent field gradient, J. Chem. Phys., 42 (1965) 288-292.
[15] W.S. Price, Pulsed-field gradient nuclear magnetic resonance as a tool for studying translational diffusion .1. Basic theory, Concepts Magn. Reson., 9 (1997) 299-336.
[16] P.T. Callaghan, K.W. Jolley, R.S. Humphrey, Diffusion of fat and water in cheese as studied by pulsed field gradient nuclear magnetic resonance, J. Colloid Interface Sci., 93 (1983) 521-529.
[17] H. Walderhaug, O. Soderman, D. Topgaard, Self-diffusion in polymer systems studied by magnetic field-gradient spin-echo NMR methods, Prog. Nucl. Magn. Reson. Spectrosc., 56 (2010) 406-425.
[18] C.S. Johnson, Diffusion ordered nuclear magnetic resonance spectroscopy: principles and applications, Prog. Nucl. Magn. Reson. Spectrosc., 34 (1999) 203-256.
[19] A.E. Frise, S.V. Dvinskikh, H. Ohno, T. Kato, I. Furo, Ion channels and anisotropic ion mobility in a liquid-crystalline columnar phase as observed by multinuclear NMR diffusometry, J. Phys. Chem. B, 114 (2010) 15477-15482.
[20] T. Singh, A. Kumar, static dielectric constant of room temperature ionic liquids: internal pressure and cohesive energy density approach, J. Phys. Chem. B, 112 (2008) 12968-12972.

Chapter 8

Summary and Future Work

8.1 Summary

This dissertation primarily focuses on investigating transport and anisotropy inside ionomer membranes using NMR diffusometry and spectroscopy. The strategy relies on tracking the positions and orientations of molecular probes to detect structural hierarchies on multiple length scales. Using appropriate molecular probes and diffusion theories, these studies have revealed some critical information regarding structural features such as anisotropy, domain structures, defects and density variations of ionic groups inside ionomers.

We have systematically studied water transport and morphology for a class of poly(arylene ether sulfone) hydrophilic-hydrophobic multi-block copolymer membranes and polymeric blend membranes. For the block copolymers, multi-axis pulsed-field-gradient NMR yields *diffusion anisotropy*, the ratio of diffusion coefficients measured both in plane ($\boldsymbol{D}_{//}$) and through plane ($\boldsymbol{D}_{\perp}$). ^{2}H NMR spectroscopy on absorbed D_2O further probes membrane alignment modes. Both types of measurements corroborate uniformly ordered planar structures oriented through the membrane plane in accordance with a lamellar morphology previously observed locally with microscopy. The combination of these two measurements also provides insights into average defect distributions.

For the polymer blend membranes, an increase in compatibilizer significantly improves the membrane phase homogeneity observed by SEM, which is consistent with observed enhancements in proton conductivity and changes in diffusion phenomena. We further observe drastic changes in local restrictions to water diffusion among different blend membranes, and use

theories of diffusion in porous media to understand improvements in domain size R_c and tortuosity $\mathfrak{I}$ with phase homogeneity. NMR relaxometry studies yield multi-component T_1 values, which further probe structural heterogeneities on smaller scales than diffusion experiments.

We then investigate ion transport in ILs and inside perfluorosulfonate ionomers. Cation and anion diffusion coefficients combine to reflect inter-ionic interactions, which are modulated by hydration and ionic media. With increasing hydration of ILs, the anomalous ratio of cation to anion diffusion coefficients reverses, then plateaus to values consistent with expected hydrodynamic radii ratios (r_{cation}/r_{anion} = 1.4 for $[C_2mim][BF_4]$). When ILs diffuse inside an ionomer, ion associations are modulated by ionic interactions between mobile cations and anions, and drag from fixed $-SO_3^-$ lining the polymer's hydrophilic channels. At high hydration, isolated anions diffuse faster ($\leq$ 4X) than cations. Surprisingly, cations diffuse substantially faster ($\leq$ 3X) at low hydration inside membranes, revealing prevalent anionic aggregates.

Finally, we utilize the idea of double probes to examine the structural feature of perfluorosulfonate ionomers. We employ high gradient strength to measure the slow ion diffusion inside the polymers without water. Cations exhibit normal diffusion behavior and suggest there is no structural heterogeneity beyond 100 nm in the material. In contrast, anion diffusion studies provide solid evidence to signify a distribution of local structures that strongly confine anion motions. Varying temperatures, hydration levels and IL uptakes lead to a significant change in the average size and distribution of these structures, which demonstrate the non-static and ionic nature of these confinement structures. We attribute these structures to the spatial organization of SO_3^- groups that defines a particular "structure" - a distribution of local electrical potentials, which vary constantly with thermal fluctuations and local ionic medium.

This study provides new insights into the role of local structural variations on ion transport and presents a new pathway to understand the "ionic" nature of these ionomers.

8.2 Future work

The success of studying slow ion diffusion (~10^{-13} m^2/s) inside ionomers by PFG NMR allows probing structural characteristics down to ~100 nm. This work further lays out the basis for interrogating a variety of ion containing polymers with regard to local ion density variations and ionic domain structure. Future work will focus on more systematic studies toward investigating water and ion transport inside other representative or commercial ionomers, such as Aquivion (perfluorosulfonate ionomers with short side chains), Flemion (perfluorocarboxylic ionomers) or Kraton polymers (sulfonated styrenic pentablock copolymers). Detailed correlations between structure and transport properties are crucial to determine relevant parameters for designing materials with improved performances. In parallel to these work, we will put more effort to study the dynamics and intermolecular interactions inside ionomers. Homonuclear and heteronuclear overhauser effect spectroscopy (NOESY and HOESY) are useful tools for these studies, which directly measure intra and intermolecular couplings. Some of our preliminary studies have already shown evidence for strong intermolecular couplings, which support the concept of ion associations between cations and anions. A general picture that combines ion motion, associations and dynamics inside ionomers will become more comprehensive based on these advanced NMR studies.